Search for Supersymmetric Particles with the OPAL Detector at LEP2

OPAL 検出器を用いた LEP2 での超対称性粒子の探索

神戸大学大学院自然科学研究科
金谷 奈央子

平成 13 年 3 月

Abstract

A search for Supersymmetric particles was performed using the data collected in 1999 and 2000 by the OPAL detector at the LEP2 e^+e^- collider. The centre-of-mass energies ranged from 192 GeV to 209 GeV, and the data analyzed correspond to an integrated luminosity of 432 pb^{-1}. Supersymmetric models permit a large number of different experimental final states which should all be investigated. The search presented here is sensitive to final states with photons plus additional detector activity with missing energy. These topologies are characteristic of events expected in Gauge-Mediated Supersymmetry Breaking (GMSB) models. No significant evidence for their existence is observed. Finally, using various search results at centre-of-mass energy of 189 GeV, constraints on the parameters have been given within the framework of the minimal GMSB model.

Acknowledgements

I'd like to thank Professor H. Takeda, who gave me an opportunity to study at the LEP experiment. And, I'd like to thank Professor S. Komamiya, who accepted me and helped me in my first work. I'm thankful to people of Kobe University and ICEPP (International Center of Elementary Particle Physics), the University of Tokyo.

I'd like to express my gratitude for some people who gave me very helpful advice.

Professor K. Kawagoe, he helped me to complete this thesis, and his advice was very helpful. Dr. I. Nakamura, who taught me analyzing data at the LEP experiment and his help was very useful in my work. Dr. S. Yamashita, his advice promoted better my understanding of OPAL detector. Prof. E. Duchovni, who works on interpretations with the GMSB models and helped me through many discussions. Dr. S. Mihara, who is one of precursors of the GMSB SUSY search and gave me advice when I had a problem. Dr. R.A. McPherson, who is also one of precursors of the GMSB SUSY search and helped me in every respect, and also organized the search working group well. Dr. S. Asai, who is well versed in phenomenology of Supersymmetry, offered an enormous of Monte Carlo samples and gave me advice through many discussions. I'm thankful to the SL Division of CERN for the excellent LEP operation, and other CERN staffs for their support.

I'd like to thank to the OPAL secretaries, M. Stuwe and D. Hudson, who are so kind to encourage and help me anytime. Finally, I'd like to thank my parents, sister, grandmother, and my great friends for their continuous help and encouragement.

Preface

The LEP accelerator is an electron-positron storage ring, which is the largest e^+e^- collider in the world. From 1989 to 1995, LEP was operated at centre-of-mass (cms) energies near 91 GeV to make precision measurements at the electroweak scale. In the next phase called LEP1.5, LEP was running at cms energies of 131–136 GeV. LEP was then operated at energies above the W^+W^-production threshold (LEP2) from 1996. LEP increased its cms energy step by step and it reached the maximum cms energy of 209 GeV. Before LEP was shut down in November 2000, data corresponding to an integrated luminosity of 700 pb^{-1} were collected at high energies (LEP1.5–LEP2). LEP offered a marvelous experimental environment, i.e. clean data, high energies and large amount of luminosities for new particle searches.

The Standard Model has been extremely successful in describing a wide variety of measurements in particle physics. The Standard Model does, however, still have unresolved puzzles. It is natural to consider the Standard Model as a low-energy effective model of a more fundamental theory.
Supersymmetry is one of the most promising theories, which can describe the physics beyond the electroweak scale. In order to verify Supersymmetry, at least one new particle predicted in the theory must be discovered. The particle would be massive enough to have escaped previous detection. In spite of extensive studies for Supersymmetry, no indication has been observed experimentally. Do Supersymmetric particles exist? Are Supersymmetric particles much heavier? Or does Supersymmetry offer special event topologies which have not ever been studied?

At the Tevatron collider experiment, an event of $ee\gamma\gamma$ with missing energy was observed, which is difficult to explain within the Standard Model. This event can be interpreted with GMSB models. Moreover, GMSB scenarios are also favored theoretically, because of its high predictability and advantage of suppressing the flavor changing neutral current (FCNC) processes.

I studied topologies of "*photon plus X (jets or leptons) with missing energy*" using the data collected with the OPAL detector at LEP. These topologies are specific to the GMSB models and they have not been fully studied so far. Although such a new particle has not been discovered in my analysis, the result is helpful for searches at the future hadron collider and linear collider experiments. I hope that we discover an indication of new phenomena in the near future.

Contents

Chapter 1

Introduction

The Standard Model of particle physics, which describes the strong, weak and electromagnetic interactions of particles, has been very successful in accounting for a wide variety of experimental measurements. However, the Standard Model is considered to be a low energy effective theory of a more fundamental framework. The framework must be free from several theoretical problems that occur as soon as one tries to extend the Standard Model to higher energies. *Supersymmetry* is one of the most elegant theories that provide such a solid framework.

A successful supersymmetric theory should not only resolve the problems in the Standard Model but also be constructed reasonably without any inconsistency with the current experimental observations. One of the most stringent bounds comes from contributions of new particles to the flavor changing neutral current (FCNC) processes. The *Gauge-Mediated Supersymmetry Breaking (GMSB)* scenario is one of the solutions, which does not contradict such low-energy constraints. This model predicts existence of some light new particles, which interact with the Standard Model particles via weak or electromagnetic couplings and might be produced at LEP energies.

Various production and decay processes of SUSY particles are possible, and they depend on model parameters. Some topologies are similar to those expected in Gravity-Mediated Supersymmetry Breaking models (SUGRA), and have been previously studied. It is also attractive to investigate additional topologies, expected in GMSB scenarios, which have not been considered in the SUGRA models.

The results presented here are based on the OPAL data collected in 1999 and 2000. The report is organized as follows: In Chapter 1, a short introduction of Supersymmetry and its motivation are presented. Chapter 2 explains the structure of models with the Gauge-Mediated Supersymmetry Breaking and also shows an overview of phenomenological aspects and experimental signals motivated by the GMSB scenario. Chapter 3 describes the LEP accelerator and the OPAL detector. Tools for the analysis, such as basic algorithms and Monte Carlo samples, are described in Chapter 4. Analyses, their results and model-independent upper limits on production cross-sections are presented in Chapter 5. Chapter 6 gives the theoretical interpretation with the minimal GMSB model. The summary of this work is given in Chapter 7.

1.1 The Standard Model

1.1.1 Introduction

The Standard Model which describes the electroweak and strong interactions has been extensively tested for the last 30 years. Even after precise measurements of the electroweak parameters in electron-positron collisions at the Z^0 pole, there is not a signal experimental result that contradicts the Standard Model predictions. A remnant scalar field, the Higgs boson, is the only missing piece

of the Standard Model that still awaits experimental confirmation.

The Standard Model is a quantum field theory which describes the interactions of spin-1/2 point-like fermions, whose interactions are mediated by spin-1 gauge bosons. The bosons are a consequence of a local gauge invariance applied to the fermion fields and are a manifestation of the symmetry group of the theory, *i.e.*, $SU(3)_C \times SU(2)_L \times U(1)_Y$.

The fundamental fermions are leptons and quarks. The left-handed states are doublets under the $SU(2)_L$ group, while the right-handed states are singlets. There are three generations of fermions, being identical except for masses: the origin of this structure and the breaking of generational symmetry (flavor symmetry) are not understood yet. There are three leptons with electric charge -1, the electron (e), muon (μ) and tau lepton (τ) and three electrically neutral leptons, the neutrinos ν_e, ν_μ and ν_τ. Similarly, there are three quarks with electric charge +2/3 , up (u), charm (c) and top (t), and three with electric charge -1/3, down (d), strange (s) and bottom (b). The quarks are triplets under the $SU(3)_C$ group and thus carry an additional 'charge', referred to as "color". There is a mixing between the three generations of quarks parameterized by the Cabibbo-Kobayashi-Maskawa (CKM) matrix whose origin is not explained by the Standard Model.

The $SU(2)_L \times U(1)_Y$ symmetry group, which describes the electroweak interaction, is spontaneously broken by the existence of Higgs field(s) with non-zero vacuum expectation value (VEV). This leads to the emergence of massive vector bosons, the $W^{\pm}$ and Z^0, which mediate the weak interaction, while the photon of electromagnetism remains massless. One physical degree of freedom remains in the Higgs sector, which should manifest itself as a neutral scalar boson H^0, which is yet to be discovered. The $SU(3)_C$ group describes the strong interaction (quantum chromodynamics, QCD). Eight vector gluons mediate this interaction. They carry color charges themselves, and are thus self-interacting. This implies that the QCD coupling α_s is small for large momentum transfers. This largeness of α_s at lower energies leads to the confinement of quarks inside color-neutral hadrons.

In the simplest version, the Standard Model has 19 parameters. Among them are: the three coupling constants of the gauge theory $SU(3)_C \times SU(2)_L \times U(1)_Y$, three lepton and six quark masses, the mass of the Z^0 boson which sets the scale of the weak interaction, and the four parameters which describe the rotation from the weak to the mass eigenstates of the charge -1/3 quarks (CKM matrix). All of these parameters are known with an individual experimental error. A CP-violating parameter associated with the strong interactions must be very small. The last parameter is associated with the mechanism responsible for the breakdown of electroweak $SU(2)_L \times U(1)_Y$ to $U(1)_{\rm em}$. This can be taken as the mass of the Higgs boson. The couplings of the Higgs boson are determined once its mass is given.

1.1.2 Higgs mechanism and the particle masses in the Standard Model

In order to apply the Higgs mechanism to give masses to $W^{\pm}$and Z^0, let us introduce a scalar doublet

$$\Phi = \begin{pmatrix} \phi^\dagger \\ \phi^0 \end{pmatrix} . \tag{1.1}$$

From the Gell-Mann-Nishijima relation in the weak-isospin space $Q = T_3 + 1/2Y$, we verify that the weak-hypercharge of the Higgs doublet is Y = 1. We introduce the Lagrangian

$$\mathcal{L}_{\rm scalar} = \partial_\mu \Phi^\dagger \partial^\mu \Phi - V(\Phi^\dagger \Phi) ,$$

where the potential V is given by

$$V(\Phi^\dagger \Phi) = \mu^2 \Phi^\dagger \Phi + \lambda (\Phi^\dagger \Phi)^2 \qquad (\mu^2 < 0, \lambda > 0) . \tag{1.2}$$

In order to maintain the gauge invariance under the $SU(2)_L \otimes U(1)_Y$, we have to introduce the covariant derivative

$$\partial_\mu \to D_\mu = \partial_\mu + ig\frac{\tau^i}{2}W_\mu^i + i\frac{g'}{2}YB_\mu.$$

We can choose the vacuum expectation value of the Higgs field as,

$$< \Phi >_0 = \begin{pmatrix} 0 \\ \upsilon/\sqrt{2} \end{pmatrix},$$

where

$$\upsilon = \sqrt{-\frac{\mu^2}{\lambda}}. \tag{1.3}$$

Since we want to preserve the exact electromagnetic symmetry to maintain the electric charge conserved, we must break the original symmetry group as

$$SU(2)_L \otimes U(1)_Y \to U(1)_{\rm em},$$

i.e. after the spontaneous symmetry breaking, the subgroup $U(1)_{\rm em}$, of dimension 1, should remain as a symmetry of the vacuum.
In this case the corresponding gauge boson, the photon, will remain massless. We can verify that our choice of the vacuum is invariant under $U(1)_{\rm em}$. This invariance requires that

$$e^{i\alpha Q} < \Phi >_0 \sim (1 + i\alpha Q) < \Phi >_0 = < \Phi >_0,$$

or, the operator Q annihilates the vacuum, $Q < \Phi >_0 = 0$. This is exactly what happens: the electric charge of the vacuum is zero,

$$\begin{aligned} Q < \Phi >_0 &= \left(T_3 + \frac{1}{2}Y\right) < \Phi >_0 \\ &= \frac{1}{2}\left[\begin{pmatrix} 1 & 0 \\ 0 & -1 \end{pmatrix} + \begin{pmatrix} 1 & 0 \\ 0 & 1 \end{pmatrix}\right]\begin{pmatrix} 0 \\ \upsilon/\sqrt{2} \end{pmatrix} = 0\,. \end{aligned}$$

The other gauge bosons, corresponding to the *broken generator* T_1, T_2, and $(T_3 - Y/2) = 2T_3 - Q$ should acquire masses. In order to make this explicit, let us parameterize the Higgs doublet as,

$$\begin{aligned} \Phi &\equiv \exp\left(i\frac{\tau^i}{2}\frac{\chi_i}{\upsilon}\right)\begin{pmatrix} 0 \\ (\upsilon + H)/\sqrt{2} \end{pmatrix} \\ &\sim < \Phi >_0 + \frac{1}{2\sqrt{2}}\begin{pmatrix} \chi_2 + i\chi_1 \\ 2H - i\chi_3 \end{pmatrix} = \frac{1}{\sqrt{2}}\begin{pmatrix} i\sqrt{2}w^+ \\ \upsilon + H - iz^0 \end{pmatrix}, \end{aligned}$$

where w^+ and z^0 are the Goldstone bosons.

Now, if we make a $SU(2)_L$ gauge transformation with $\alpha_i = \chi_i/\upsilon$ (unitary gauge), the fields become

$$\Phi = \Phi' = \exp\left(-i\frac{\tau^i}{2}\frac{\chi_i}{\upsilon}\right)\Phi = \frac{(\upsilon + H)}{\sqrt{2}}\begin{pmatrix} 0 \\ 1 \end{pmatrix}, \tag{1.4}$$

and the scalar Lagrangian can be written in terms of these new fields as

$$\mathcal{L}_{\rm scalar} = \left|\left(\partial_\mu + ig\frac{\tau^i}{2}W_\mu^i + i\frac{g'}{2}YB_\mu\right)\frac{(\upsilon + H)}{\sqrt{2}}\begin{pmatrix} 0 \\ 1 \end{pmatrix}\right|^2 - \mu^2\frac{(\upsilon + H)^2}{2} - \lambda\frac{(\upsilon + H)^4}{4}\,. \tag{1.5}$$

In term of the physical fields $\mathrm{W}^{\pm}$ and Z^0 the first term of Eq.(1.5), that contain the vector bosons, is

$$\left|\begin{pmatrix} 0 \\ \partial_\mu H/\sqrt{2} \end{pmatrix} + i\tfrac{g}{2}(\upsilon + H)\begin{pmatrix} W_\mu^+ \\ (-1/\sqrt{2}\cos\theta_W)Z_\mu \end{pmatrix}\right|^2 = \tfrac{1}{2}\partial_\mu H \partial^\mu H + \tfrac{g^4}{4}(\upsilon + H)^2\left(W_\mu^+ W^{-\mu} + \tfrac{1}{2\cos^2\theta_W} Z_\mu Z^\mu\right), \tag{1.6}$$

where θ_W is called the Weinberg angle which represents the mixing of the neutral fields in $U(1)_Y$ and $SU(2)_L$.

The quadratic terms in the vector fields are,

$$\frac{g^2\upsilon^2}{4} W_\mu^+ W^{-\mu} + \frac{g^2\upsilon^2}{8\cos^2\theta_W} Z_\mu Z^\mu \,.$$

When compared with the usual mass terms for a charged and neutral vector bosons,

$$M_W^2 W_\mu^+ W^{-\mu} + \frac{1}{2} M_Z^2 Z_\mu Z^\mu \,,$$

we can easily identify

$$M_W = \frac{g\upsilon}{2}\,, \qquad M_Z = \frac{g\upsilon}{2\cos\theta_W} = \frac{M_W}{\cos\theta_W}\,.$$

We can see from Eq.(1.6) that no quadratic term in A_μ appears, and therefore, the photon remains massless, as we can expect since the $U(1)_{\mathrm{em}}$ remains as a symmetry of the theory.
Taking into account the low-energy phenomenology via the relation $g/2\sqrt{2} = (M_{\mathrm{W}}^2 G_F/\sqrt{2})^{1/2}$, we obtain the vacuum expectation value as

$$\upsilon = (\sqrt{2}G_F)^{1/2} \sim 246\mathrm{GeV}\,.$$

The Standard Model predictions for the $\mathrm{W}^{\pm}$ and Z^0 masses are

$$M_{\mathrm{W}^\pm}^2 = \frac{e^2}{4\sin^2\theta_W}\upsilon^2 = \frac{\pi\alpha}{\sin^2\theta_W}\upsilon^2 \sim \left(\frac{37.2}{\sin^2\theta_W}\mathrm{GeV}\right)^2 \sim (80\mathrm{GeV})^2,$$

$$M_{\mathrm{Z}^0}^2 \sim \left(\frac{37.2}{\sin\theta_W\cos\theta_W}\mathrm{GeV}\right)^2 \sim (90\mathrm{GeV})^2,$$

where we assumed an experimental value for $\sin^2\theta_W \simeq 0.22$.

We can learn from Eq.(1.5) that one scalar boson, out of the four degrees of freedom introduced in Eq.(1.1), is the remnant of the symmetry breaking. Search for the Higgs boson remains as one of the major challenges in collider experiments. The second term of Eq.(1.5) gives rise to terms involving exclusively the scalar field H, namely,

$$-\frac{1}{2}(-2\mu^2)H^2 + \frac{1}{4}\mu^4\upsilon^2\left(\frac{4}{\upsilon^3}H^3 + \frac{1}{\upsilon^4}H^4 - 1\right). \tag{1.7}$$

In Eq.(1.7) we can also identify the Higgs boson mass term with

$$M_H = \sqrt{-2\mu^2}\,, \tag{1.8}$$

and the self-interactions of the Higgs field. In spite of predicting the existence of the Higgs boson, the Standard Model does not give a hint on the value of its mass since μ^2 is unknown.

Lepton mass

Note that the charged lepton is still massless, since

$$M_\ell \bar{\ell}\ell = M_\ell(\bar{\ell}_R \ell_L + \bar{\ell}_L \ell_R)$$

mixes L and R components and breaks gauge invariance. A way to give mass in a gauge invariant way is via the Yukawa coupling of the leptons with the Higgs field (Eq.(1.4)) , that is,

$$\begin{aligned}
\mathcal{L}^\ell_{\rm yuk} &= -G_\ell[\bar{R}\,(\Phi^\dagger L) + (\bar{L}\Phi)\,R] \\
&= -G_\ell \frac{(\upsilon + H)}{\sqrt{2}}\left[\bar{\ell}_R(0 \quad 1)\begin{pmatrix}\nu_L \\ \ell_L\end{pmatrix} + (\bar{\nu}_L \quad \bar{\ell}_L)\begin{pmatrix}0 \\ 1\end{pmatrix}\ell_R\right] \\
&= -\frac{G_\ell \upsilon}{\sqrt{2}}\bar{\ell}\ell - \frac{G_\ell}{\sqrt{2}}\bar{\ell}\ell H. \qquad (1.9)
\end{aligned}$$

Thus, we can identify the charged lepton mass,

$$M_\ell = \frac{G_\ell \upsilon}{\sqrt{2}}\,. \qquad (1.10)$$

We notice that this procedure is able to generate a mass term for the fermion in a gauge invariant way. However, it does not specify the lepton mass since the Yukawa constant G_ℓ introduced in Eq.(1.9) is arbitrary.

As a consequence, we obtain the Higgs-lepton coupling with a strength

$$C_{\bar{\ell}\ell H} = \frac{M_\ell}{\upsilon}\,, \qquad (1.11)$$

which is a precise prediction of the Standard Model to be checked experimentally.

Quark mass

In order to generate masses for both of the up ($U_i = u,\ c$ and t) and down ($D_i = d,\ s$ and t) quarks, we need a Higgs doublet with $Y = -1$. Defining the conjugate doublet Higgs as

$$\tilde{\Phi} = i\sigma_2 \Phi^* = \begin{pmatrix}\phi^{0*} \\ -\phi^-\end{pmatrix}\,, \qquad (1.12)$$

we can write the Yukawa Lagrangian for three generations of quarks as,

$$\mathcal{L}^q_{\rm yuk} = -\sum_{i,j=1}^{3}\left[G^U_{ij}\bar{R}_{U_i}(\bar{\Phi}^\dagger L_j) + G^D_{ij}\bar{R}_{D_i}(\Phi^\dagger L_j)\right] + h.c.\,. \qquad (1.13)$$

From the vacuum expectation value of Φ and $\bar{\Phi}$ doublets, we obtain the mass terms for the up

$$\overline{(u', c', t')}_R \mathcal{M}^U \begin{pmatrix}u' \\ c' \\ t'\end{pmatrix}_L + h.c.,$$

and down quarks

$$\overline{(d', s', b')}_R \mathcal{M}^D \begin{pmatrix}d' \\ s' \\ b'\end{pmatrix}_L + h.c.,$$

with non-diagonal matrices $\mathcal{M}_{ij}^{U(D)} = (v/\sqrt{2})G_{ij}^{U(D)}$.

The weak eigenstates (q') are linear superposition of the mass eigenstates (q) given by unitary transformations:

$$\begin{pmatrix} u' \\ c' \\ t' \end{pmatrix}_{L,R} = U_{L,R} \begin{pmatrix} u \\ c \\ t \end{pmatrix}_{L,R} , \qquad \begin{pmatrix} d' \\ s' \\ b' \end{pmatrix}_{L,R} = D_{L,R} \begin{pmatrix} d \\ s \\ b \end{pmatrix}_{L,R} ,$$

where $U(D)_{L,R}$ are unitary matrices to preserve the form of the kinetic terms of the quarks. These matrices diagonalize the mass matrices, *i.e.*,

$$U_R^{-1}\mathcal{M}^U U_L = \begin{pmatrix} m_u & 0 & 0 \\ 0 & m_c & 0 \\ 0 & 0 & m_t \end{pmatrix} ,$$

$$D_R^{-1}\mathcal{M}^D D_L = \begin{pmatrix} m_d & 0 & 0 \\ 0 & m_s & 0 \\ 0 & 0 & m_b \end{pmatrix} .$$

The $(V-A)$ charged weak current for three generations will be proportional to

$$\overline{(u', c', t')}_L \gamma_\mu \begin{pmatrix} d' \\ s' \\ b' \end{pmatrix}_L = \overline{(u, c, t)}_L (U_L^\dagger D_L)\gamma_\mu \begin{pmatrix} d \\ s \\ b \end{pmatrix}_L$$

with the generation mixing of the mass eigenstates (q) described by:

$$\mathbf{V} \equiv (U_L^\dagger D_L) .$$

On the other hand, for the neutral current of the quarks, now becomes,

$$\overline{(u', c', t')}_L \gamma_\mu \begin{pmatrix} u' \\ c' \\ t' \end{pmatrix}_L = \overline{(u, c, t)}_L (U_L^\dagger U_L)\gamma_\mu \begin{pmatrix} u \\ c \\ t \end{pmatrix}_L .$$

We can notice that there is no mixing in the neutral sector (FCNC) since the matrix U_L is unitary: $U_L^\dagger U_L = 1$.

The quark mixing, by convention, is restricted to the down quarks, that is with $T_3^q = -1/2$,

$$\begin{pmatrix} d' \\ s' \\ b' \end{pmatrix}_L = \mathbf{V} \begin{pmatrix} d \\ s \\ b \end{pmatrix}_L .$$

$\mathbf{V}$ is the Cabbibo-Kobayashi-Maskawa matrix, that can be parameterized as

$$\mathbf{V} = R_1(\theta_{23})R_2(\theta_{13}\delta_{13})R_3(\theta_{12}),$$

where $R_i(\theta_{jk})$ are rotation matrices around the axis i, the angle θ_{jk} describes the mixing of the generations j and k, and δ_{13} is a phase.

We should notice that, for three generations, it is not always possible to choose the $\mathbf{V}$ matrix to be real, that is $\delta_{13} = 0$, and therefore the weak interaction can violate CP and T.

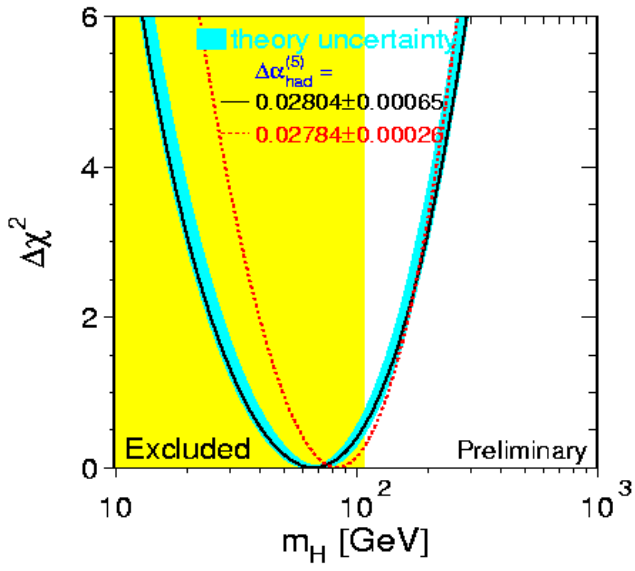

Figure 1.1: *The Standard Model fit to experimental data with respect to the Higgs mass. The shaded region is excluded by the direct search.*

The Cabbibo-Kobayashi-Maskawa matrix can be written as

$$\mathbf{V} = \begin{pmatrix} c_{12}c_{13} & s_{12}c_{13} & s_{13}e^{-i\delta_{13}} \\ -s_{12}c_{23} - c_{12}s_{23}s_{13}e^{i\delta_{13}} & c_{12}c_{23} - s_{12}s_{23}s_{13}e^{i\delta_{13}} & s_{23}c_{13} \\ s_{12}s_{23} - c_{12}c_{23}s_{13}e^{i\delta_{13}} & -c_{12}s_{23} - s_{12}c_{23}s_{13}e^{i\delta_{13}} & c_{23}c_{13} \end{pmatrix},$$

where $s_{ij}(c_{ij}) \equiv \sin(\cos)\theta_{ij}$. Notice that, in the limit of $\theta_{23} = \theta_{13} \to 0$, we associate $\theta_{12} \to \theta_C$, Cabbibo angle, and

$$\mathbf{V} \to \begin{pmatrix} c_{12} & s_{12} & 0 \\ -s_{12} & c_{12} & 0 \\ 0 & 0 & 1 \end{pmatrix}.$$

Using unitarity constraint and assuming only three generations the experimental value for the elements of the matrix $\mathbf{V}$, with 90 % of C.L., can be extracted from weak quark decays and from deep inelastic neutrino scattering as,

$$\mathbf{V} = \begin{pmatrix} 0.9742 - 0.9757 & 0.219 - 0.226 & 0.002 - 0.005 \\ 0.219 - 0.225 & 0.9734 - 0.9749 & 0.037 - 0.043 \\ 0.004 - 0.014 & 0.035 - 0.043 & 0.9990 - 0.9993 \end{pmatrix}.$$

1.2 Beyond the Standard Model

The negative results for direct searches of the Higgs boson have been translated into a lower limit on its mass of 109.7 GeV (95%C.L.) [1]. Indirect constraints are obtained from the precise measurements of the Z^0 lineshape suggesting $m_H = 390\ ^{+390}_{-280}$ GeV [2]. The present situation is depicted in Figure 1.1. Thus, if the Standard Model Higgs boson exists, its mass should be close to the electroweak scale $\sim$ 100 GeV. Moreover, m_H has to be less than about 1 TeV to preserve the unitarity of the W^+W^- scattering.

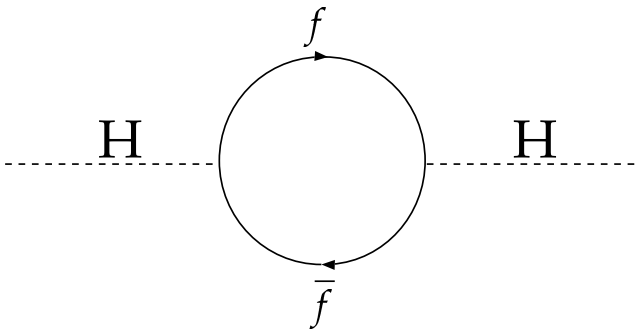

Figure 1.2: *1-loop diagrams contributing to m_H correction*

Despite the success of the Standard Model in reproducing experimental observations, there are theoretical problems that occur when one goes to much higher energy scales. A new framework is necessary at the Planck scale $M_P = (8\pi G_{\rm Newton})^{-1/2} = 2.4 \times 10^{18}$ GeV where quantum gravitational effects become important. The 16 orders of magnitude between the explored weak scale and the Planck scale are considered somewhat unnatural. This argument, called *hierarchy problem*, is based also on more quantitative facts.

It is very instructive to compute the first order correction to the Higgs mass m_H due to a generic fermion loop (see Figure 1.2). It depends on the fermion-antifermion production probability integrated on all possible values of the momentum k carried by the fermion in the loop. Since the Higgs coupling to a fermion f is $(y_f/\sqrt{2})H\bar{f}f$, one finds:

$$\begin{aligned}\Delta m_H^2 &= -\int \frac{d^4k}{(2\pi)^4}\mathbf{Tr}\left[\left(i\frac{y_f}{\sqrt{2}}\right)\frac{i}{\hat{k}-m_f}\left(i\frac{y_f}{\sqrt{2}}\right)\frac{i}{\hat{k}-m_f}\right] \\ &= -2y_f^2\int\frac{d^4k}{(2\pi)^4}\left[\frac{1}{k^2-m_f^2}+\frac{2m_f^2}{(k^2-m_f^2)^2}\right],\end{aligned}$$

where $\hat{k} = \gamma_\mu k^\mu$. A color factor 3 must be multiplied for quarks. The first term of the second line is quadratically divergent. If no new physics is expected up to the Planck scale, $M_{\rm Planck}$ will be the cutoff used to "regulate" the integral. A correction on m_H^2 results in more than 30 order of magnitude larger than the mass expected from the Standard Model fit. There is always the possibility to renormalize away the bad quadratic term, as for logarithmic divergences is done. If some new physics appears at a very high scale the new fermions will have masses close to that scale. Even if a bad ultraviolet behavior is accepted in the theory, their correction terms proportional to $y_f m_f$ will be very large. They must cancel themselves to bring the Higgs mass well below 1 TeV and this is possible only if the involved parameters undergo to an extreme fine-tuning. This problem is called *naturalness problem* when we wish to reconstruct realistic models of the "fundamental physics" beyond the Standard Model. One possibility to solve this problem is Supersymmetry, which introduces a symmetry between fermions and bosons to eliminate the quadratic divergence.

It turns out that the new physics must be very close to the present explored scale. In fact, the small expected value for Higgs yields to a small quadratic coupling constant λ. Figure 1.4 shows the evolution of λ in the Standard Model. The constant λ must be positive to have a stable minimum in the Higgs potential. In case of the Standard Model, the Higgs boson should be lighter than ~ 180 GeV so that λ remains perturbative up to the Planck scale. Some new particles alter the λ running, and the upper limit on the Higgs mass is reduced to be ~ 170 GeV within the minimal SUGRA.

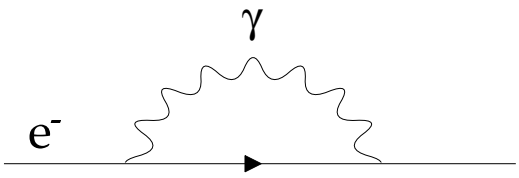

Figure 1.3: *1-loop diagram contributing to m_e correction.*

The 1-loop correction Δm_e to the electron mass due to a photon emission can be computed for comparison. As in the previous case, according to the diagram in Figure 1.3, one finds:

$$\begin{aligned}\Delta m_e &= \int \frac{d^4k}{(2\pi)^4}(-ie\gamma_\mu)\frac{i}{\hat{k}-m_e}(-ie\gamma_\nu)\frac{-ig^{\mu\nu}}{k^2} \\ &= -4e^2 m_e \int \frac{d^4k}{(2\pi)^4}\frac{1}{k^2(k^2-m_e^2)}\,,\end{aligned}$$

where $g^{\mu\nu}$ is the standard Lorenz metric tensor. The integral has a logarithmic divergence in the ultraviolet but the m_e correction is proportional to m_e itself. Even if $M_{\rm Planck}$ is used to cut-off the divergence a small correction turns out;

$$\Delta m_e \sim 4e^2 m_e \log\frac{M_{\rm Planck}}{m_e} \sim 0.24 m_e\,. \tag{1.14}$$

In the limit $m_e \longrightarrow 0$ the model becomes invariant under chiral rotations and the correction vanishes; in other words, the chiral symmetry protects the electron mass against divergences (like any fermion mass as well). Similarly the gauge invariance prevents gauge bosons from having dangerous divergences.

The message of this short description about the weak points of the Standard Model is: some new physics just < 1 TeV is necessary and reasonable.

1.3 Supersymmetry

1.3.1 Introduction

In the Standard Model, the Higgs potential is given by

$$V = \mu^2|H|^2 + \lambda|H|^4\,,$$

where $v =< H >^2 = -\mu^2/2\lambda = (176\text{GeV})^2$. Because a perturbative unitarity requires that $\lambda < 1$, $-\mu^2$ is of the order of (100 GeV)^2. However, the mass squared parameter μ^2 of the Higgs doublet receives a quadratically divergent contribution from its self-energy corrections. Main contribution comes from a pair of top quarks;

$$\Delta\mu_t^2 = -6\frac{y_t^2}{4\pi^2}\Lambda_{\rm eff}^2\,,$$

where $\Lambda_{\rm eff}$ is the cutoff energy for top quark momentum, and $y_t \sim 1$ is the top quark Yukawa coupling.

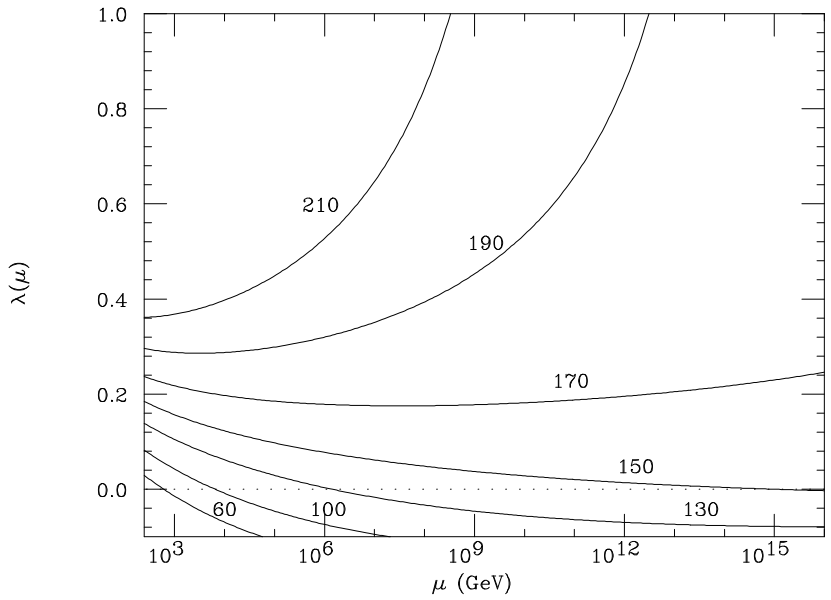

Figure 1.4: *Quadratic coupling constant running for different values of the Higgs mass in GeV. The evolutions of λ start from several initial conditions that set the Higgs mass at the scale $\mu = \sqrt{2}v$ = 246 GeV.*

The motivation for Supersymmetry[7] [8][9] is to make the Standard Model applicable to much higher energies so that we can hope that answers to many puzzles in the Standard Model can be given by physics at higher energy scales. To this purpose, Supersymmetry doubles the degrees of freedom with an explicitly broken new symmetry. The top quark would have a superpartner, stop, whose loop diagram gives another contribution to the Higgs boson self energy

$$\Delta\mu_{\tilde{t}}^2 = +6\frac{y_{\tilde{t}}}{4\pi^2}\Lambda_{\text{eff}}^2 \,.$$

The leading pieces in Λ_{eff} cancel between the top and stop contributions, and one obtains the correction

$$\Delta\mu_t + \Delta\mu_{\tilde{t}} = -6\frac{y_t^2}{4\pi^2}(m_{\tilde{t}}^2 - m_t^2)\log\frac{\Lambda_{\text{eff}}^2}{m_{\tilde{t}}^2} \,.$$

One important things is that the mass of the stop $m_{\tilde{t}}$ is unknown. In order for the $\Delta\mu^2$ to be the same order of magnitude as the tree-level value $\mu^2 = -2\lambda v^2$, we need $m_{\tilde{t}}$ to be not too far above the electroweak scale. Similar arguments apply to masses of other superpartners that couple directly to the Higgs doublet. This is the so-called *naturalness* constraint on the superparticle masses (for more quantitative discussions, see [3]).

1.3.2 Supersymmetric Lagrangian

Supersymmetry is a symmetry between bosons and fermions, and hence relates particles with different spins. All particles in supersymmetric theories fall into supermultiplets, which have both bosonic and fermionic components. There are two types of supermultiplets which appear in renormalizable field theories; chiral and vector supermultiplets.

Chiral supermultiplets are often denoted by the symbol ϕ, regarded as a short-hand notation for the three fields: a complex scalar field A, a Weyl fermion $\frac{1-\gamma_5}{2}\psi$, and a non-dynamical (auxiliary)

complex field F. Lagrangians for chiral supermultiplets consist of two parts, Kähler potential and superpotential. The Kähler potential is nothing but kinetic terms for the fields, usually written with a short-hand notation $\int d^4\theta\phi^*\phi$, which can be explicitly written down as

$$\mathcal{L} \supset \int d^4\theta\phi_i^*\phi_i = \partial_\mu A_i^* \partial^\mu A_i + \bar{\psi}_i i\gamma^\mu \partial_\mu \psi_i + F_i^* F_i \,. \tag{1.15}$$

Note that the field F does not have derivatives in the Lagrangian and hence is not a propagating field. One can solve for F_i explicitly and eliminate it from the Lagrangian completely.

The superpotential is defined by a superfield $W(\phi)$ of the chiral supermultiplets ϕ_i. A short-hand notation $\int d^2\theta W(\phi)$ gives the following terms in the Lagrangian,

$$\mathcal{L} \supset -\int d^2\theta W(\phi) = -\frac{1}{2}\frac{\partial^2 W}{\partial\phi_i \partial\phi_j}\bigg|_{\Phi_i=A_i} \psi^i\psi^j + \frac{\partial W}{\partial\phi_i}\bigg|_{\Phi_i=A_i} F_i \,. \tag{1.16}$$

The first term describes Yukawa couplings between fermionic and bosonic components of the chiral supermultiplets. Using both Eqs.(1.15, 1.16), we can solve for F and find

$$F_i^* = -\frac{\partial W}{\partial\phi_i}\bigg|_{\phi_i=A_i} \,. \tag{1.17}$$

Substituting it back to the Lagrangian, we eliminate F and instead find a potential term

$$\mathcal{L} \supset -V_F = -\left|\frac{\partial W}{\partial\phi_i}\right|^2_{\phi_i=A_i} \,. \tag{1.18}$$

Vector supermultiplets W_α (α is a spinor index), which are supersymmetric generalization of the gauge fields, consist also of three components, a Weyl fermion (gaugino) λ, a vector (gauge) field A_μ, and a non-dynamical (auxiliary) real scalar field D, all in an adjoint representation of the gauge group with an index a. A short-hand notation of their kinetic terms is

$$\mathcal{L} \supset \int d^2\theta W_\alpha^a W^{\alpha a} = -\frac{1}{4}F_{\mu\nu} + \bar{\lambda}^a i\hat{D}\lambda^a + \frac{1}{2}D^a D^a. \tag{1.19}$$

Note that the field D does not have derivatives in the Lagrangian and hence is not a propagating field. One can solve for D^a explicitly and eliminate it from the Lagrangian completely.

Since the vector supermultiplets contain gauge fields, chiral supermultiplets which transform non-trivially under the gauge group should also couple to the vector multiplets to make the Lagrangian gauge invariant. This requires the modification of the Këhler potential $\int d^4\theta\phi^*\phi$ to $\int d^4\theta\phi^\dagger e^{2gV}\phi$, where V is another short-hand notation of the vector multiplet. Then the kinetic terms in Eq.(1.15) are then modified to

$$\mathcal{L} \supset \int d^4\theta\phi_i^\dagger e^{2gV}\phi_i = D_\mu A_i^\dagger D^\mu A_i + \bar{\psi}_i i\gamma^\mu D_\mu\psi_i + F_i^\dagger F_i - \sqrt{2g}(A^\dagger T^a\lambda^a\psi) - gA^\dagger T^a D^a A \,. \tag{1.20}$$

Using Eqs.(1.19 , 1.20), one can solve for D^a and eliminate it from the Lagrangian, finding a potential term

$$\mathcal{L} \supset -V_D = -\frac{g^2}{2}(A^\dagger T^a A)^2 \,. \tag{1.21}$$

General supersymmetric Lagrangians are given by Eqs. (1.18,1.20,1.21).

Although we do not go into formal discussions of supersymmetric field theories, one important theorem must be quoted: the non-renormalization theorem of the superpotential. Under the renormalization of the theories, the superpotential does not receive renormalization at all orders in the

perturbation theory.

A very simple example of superpotential is mentioned here. Consider two chiral supermultiplets ϕ_1 and ϕ_2, with a superpotential

$$W = m\phi_1\phi_2. \tag{1.22}$$

Following the above prescription, the fermionic components have the Lagrangian

$$\mathcal{L} \supset -\frac{1}{2}\frac{\partial^2 W}{\partial\phi_i\partial\phi_j}\psi^i\psi^j = -m\psi_1\psi_2, \tag{1.23}$$

while the scalar potential term Eq.(1.18) gives

$$\mathcal{L} \supset -\left|\frac{\partial W}{\partial\phi_i}\right|^2_{\phi_i=A_i} = -m^2|A_1|^2 - m^2|A_2|^2. \tag{1.24}$$

Obviously, the terms Eqs.(1.23, 1.24) are mass terms for the fermionic (Dirac fermion) and scalar components (two complex scalars) of the chiral supermultiplets, with the same mass m. In general, fermionic and bosonic components in the same supermultiplets are degenerate in supersymmetric theories.

1.3.3 Soft Supersymmetry Breaking

The supersymmetric Lagrangian always gives degenerate bosons and fermions. In the real world, such degenerate particles have not been observed. Therefore, Supersymmetry must be broken. In the low-energy effective theories, however, terms can just be added to supersymmetric Lagrangians which break supersymmetry explicitly. The important constraint is that such explicit breaking terms should not spoil the motivation, namely to keep the Higgs mass-squared only logarithmically divergent. Such explicit breaking terms of Supersymmetry are called "soft" breakings.

Possible soft breaking terms are classified. In a theory with a renormalizable superpotential

$$W = \frac{1}{2}\mu_{ij}\phi_i\phi_j + \frac{1}{6}\lambda_{ijk}\phi_i\phi_j\phi_k\,, \tag{1.25}$$

the possible soft supersymmetry breaking terms have the following forms:

$$m^2_{ij}A^*_iA_j, \qquad M\lambda\lambda, \qquad \frac{1}{2}b_{ij}\mu_{ij}A_iA_j, \qquad \frac{1}{6}a_{ijk}\lambda_{ijk}A_iA_jA_k\,. \tag{1.26}$$

The first one is the masses for scalar components in the chiral supermultiplets, which remove degeneracy between the scalar and spinor components. The next one is the masses for gauginos which remove degeneracy between gauginos and gauge bosons. Finally, the last two ones are usually called bilinear and trilinear soft breaking terms with parameters b_{ij} and a_{ijk} with mass dimension one.

In principle, any terms with couplings with positive mass dimensions are candidates of soft supersymmetry breaking terms. Possibilities in theories without gauge singlets are

$$\psi_i\psi_j\,, \qquad A^*_iA_jA_k\,, \qquad \psi_i\lambda^a\,. \tag{1.27}$$

Obviously, the first term is possible only in theories with multiplets with vector-like gauge quantum numbers, and the last term with chiral supermultiplets in the adjoint representation. In the presence of gauge singlet chiral supermultiplets, however, such terms cause power divergences and instabilities, and hence are not soft in general. Without any gauge singlet, first two terms in Eq.(1.27) are allowed, while terms in Eq.(1.26) can also induce divergences in the presence of light gauge singlets

and heavy multiplets.

The coupling of the Higgs doublet chiral supermultiplet H to left-handed Q and right-handed T chiral supermultiplets, is given by the superpotential term

$$W = y_t Q T H_u \,. \tag{1.28}$$

This superpotential term gives rise to terms in the Lagrangian

$$\mathcal{L} = -y_t Q T H_u - y_t^2 |\tilde{Q}|^2 |H_u|^2 - y_t |\tilde{T}|^2 |H_u|^2 - m_Q^2 |\tilde{Q}|^2 - m_T |\tilde{T}|^2 - y_t A_t \tilde{Q} \tilde{T} H_u \,, \tag{1.29}$$

where m_Q^2, m_T^2 and A_t are soft parameters. Note that the field Q and T are spinors, and $\tilde{Q}$, $\tilde{T}$ and H_u are scalar components of the chiral supermultiplets. This explicit Lagrangian allows us to easily work out the one-loop self-energy diagrams for the Higgs doublet H_u, after shifting the field H_u around its vacuum expectation value (this also generates mass terms for the top quark and the scalars which have to be consistently included). The diagram with top quark loop from the first term in Eq.(1.29) is quadratically divergent (negative). The contractions of $\tilde{Q}$ or $\tilde{T}$ in the next two terms also generate (positive) contributions to the Higgs self-energy. In the absence of soft parameters $m_Q^2 = m_T^2 = 0$, these two contributions precisely cancel with each other, consistent with the non-renormalization theorem which states that no mass terms (superpotential terms) can be generated by renormalizations. However, the explicit breaking terms m_q^2 and m_T^2 make the cancellation inexact. With a simplifying assumption $m_Q^2 = m_T^2 = \tilde{m}^2$, one can find

$$\delta m_H^2 = -\frac{6 y_t^2}{(4\pi)^2} \tilde{m}^2 \log \frac{\Lambda_{\text{eff}}^2}{\tilde{m}^2}. \tag{1.30}$$

Here, Λ_{eff} is the ultraviolet cutoff of the one-loop diagrams. Therefore, these mass-squared parameters are indeed "soft" in a sense that they do not produce power divergences. Similarly, the diagrams with two $y_t A_t$ couplings with scalar top loop produce only a logarithmic divergent contribution.

1.4 The Minimal Supersymmetric Standard Model

As mentioned in the previous section, Supersymmetry is explicitly broken while retaining the absence of power divergences. Now the Standard Model is promoted to a supersymmetric theory. The minimal Supersymmetric Standard Model (MSSM) is a supersymmetric version of the Standard Model with the minimal particle content.

1.4.1 Particle Contents

All fields in the Standard Model are promoted to appropriate supermultiplets. This is obvious for the gauge bosons: they all become vector multiplets. For the quarks and leptons, left-handed and right-handed fields are taken in the Standard Model. In order to promote them to chiral supermultiplets, however, all fields should be made left-handed Weyl spinors. This can be done by charge-conjugating all right-handed fields. Therefore, when supermultiplets of the right-handed down quark is referred, supermultiplets whose left-handed spinor components are the left-handed anti-down quark fields are taken. As for the Higgs bosons, the fields in the Standard Model can be embedded into a chiral supermultiplet H_u. It can couple to the up-type quarks and generate their masses upon the symmetry breaking. In order to generate down-type quark masses, however,

$$i\sigma_2 H^* = \begin{pmatrix} H^+ \\ H^0 \end{pmatrix} = \begin{pmatrix} H^{0*} \\ -H^- \end{pmatrix} \tag{1.31}$$

is normally used. This does not work in a supersymmetric fashion because the superpotential is not allowed to take a complex conjugation of this sort. Therefore, another chiral supermultiplet H_d which has the same gauge quantum numbers of $i\sigma_2 H^*$ should be introduced. The chiral supermultiplets in the minimal case are listed in Table 1.4.1.

The particles in the MSSM are as follows. First of all, all quarks, leptons are called just in the same way as in the Standard Model, namely electron, electron-neutrino, muon, muon-neutrino, tau, tau-neutrino, up, down, strange, charm, bottom, and top. Their superpartners, which have spin 0, are named with "s" at the beginning, which stands for "scalar". They are denoted by the same symbols as their fermionic counterparts with the tilde. Therefore, the superpartner of the electron is called "selectron", and written as $\tilde{e}$. Superpartners of quarks are "squarks", and those of leptons are "sleptons". The Higgs doublets are denoted by capital H, but their physical degrees of freedom are h^0, H^0, A^0 and $H^\pm$. Their superpartners are called "higgsinos", written as $\widetilde{H}_u^0$, $\widetilde{H}_u^+$, $\widetilde{H}_d^-$, and $\widetilde{H}_d^0$. In general, fermionic superpartners of the bosons in the Standard Model have "ino" at the end of the name. Spin $1/2$ superpartners of the gauge bosons are "gauginos", and for each gauge groups: gluino for gluon, wino for W, bino for the $U(1)_Y$ gauge boson B. As a result of the electroweak symmetry breaking all neutral "inos", namely two neutral higgsinos, the neutral wino $\widetilde{W}^3$ and the bino $\widetilde{B}$ mix with one another to form four Majorana fermions. They are called "neutralinos" $\widetilde{\chi}_i^0$ for i = 1,2,3,4. Similarly, the charged higgsinos $\widetilde{H}_u^+$, $\widetilde{H}_d^-$, and charged winos $\widetilde{W}^-$, $\widetilde{W}^+$ mix and form two massive Dirac fermions "charginos" $\widetilde{\chi}_i^\pm$ for i=1,2. All particles with tilde do not exist in the non-supersymmetric Standard Model.

L_1(**1,2**)$^{-1/2}$	L_2(**1,2**)$^{-1/2}$	L_3(**1,2**)$^{-1/2}$
E_1(**1,1**)$^{+1}$	E_2(**1,1**)$^{+1}$	E_3(**1,1**)$^{+1}$
Q_1(**3,2**)$^{1/6}$	Q_2(**3,2**)$^{1/6}$	Q_3(**3,2**)$^{1/6}$
U_1(**3,1**)$^{-2/3}$	U_2(**3,1**)$^{-2/3}$	U_3(**3,1**)$^{-2/3}$
D_1(**3,1**)$^{+1/3}$	D_2(**3,1**)$^{+1/3}$	D_3(**3,1**)$^{+1/3}$
	H_u(**1,2**)$^{+1/2}$	
	H_d(**1,2**)$^{-1/2}$	

Table 1.1: *The chiral supermultiplets in the Minimal Standard Supersymmetry Model. The numbers in the bold face refer to $SU(3)_C$, $SU(2)_L$ representations. The superscripts are hypercharge.*

1.4.2 Superpotential

The $SU(3)_C \times SU(2)_L \times U(1)_Y$ gauge invariance allows the following terms in the superpotential

$$\begin{aligned} W = \quad & \lambda_u^{ij} Q_i U_j H_u + \lambda_d^{ij} Q_i D_j H_d + \lambda_e^{ij} L_i E_j H_d + \mu H_u H_d \\ & + \lambda_u'^{ijk} U_i D_j D_k + \lambda_d'^{ijk} Q_i D_j L_k + \lambda_e'^{ijk} L_i E_j L_k + \mu_i' L_i H_u \,. \end{aligned} \tag{1.32}$$

The first three terms correspond to the Yukawa couplings in the Standard Model (with exactly the same number of parameters). The subscripts *i,j,k* are generation indices. The parameter μ has mass dimension one and gives a supersymmetric mass to both fermionic and bosonic components of the chiral supermultiplets H_u and H_d. The terms in the second line of Eq.(1.32) are in general problematic as they break the baryon (B) and lepton (L) numbers.

If the superpotential contains both B- and L-violating terms, such as $\lambda_u'^{112} U_1 D_1 D_2$ and $\lambda_d'^{121} Q_1 D_2 L_1$, one can exchange $\widetilde{D}_2 = \tilde{s}$ to generate a four-fermion operator

$$\frac{\lambda_u'^{112} \lambda_d'^{121}}{m_{\tilde{s}}^2} (u_R d_R)(Q_1 L_1) \,, \tag{1.33}$$

where the spinor indices are contracted in each parentheses and the color indices by the epsilon tensor. Such an operator would contribute to the proton decay process $p \to e^+\pi^0$ at a rate $\Gamma \sim \lambda'^4 m_p^5/m_{\tilde{s}}^4$, and hence the partial lifetime of the order of

$$\tau_p \sim 6 \times 10^{-13}\text{sec} \left(\frac{m_{\tilde{s}}}{1\ \text{TeV}}\right)^4 \frac{1}{\lambda'^4}\,. \tag{1.34}$$

Unless the coupling constants are extremely small, this is clearly a disaster because the experimental limit on the proton partial lifetime in this mode is $\tau_p > 1.6 \times 10^{33}$ [45].

1.4.3 R-parity

To avoid the problem of too-rapid proton decay, a common assumption is a discrete symmetry called R-parity. The R-parity is given by

$$R_p = (-1)^{2s+3B+L}\,, \tag{1.35}$$

where s is the spin of the particle. Under R_p, all the Standard Model particles, namely quarks, leptons, gauge bosons, and Higgs bosons, carry even parity, while their superpartners carry odd parity due to the $(-1)^{2s}$ factor. Once this symmetry is imposed, all terms in the second line of Eq.(1.32) will be forbidden, and a dangerous operator such as that in Eq.(1.33) is not generated.

One immediate consequence of the conserved R-parity is that the lightest particle with odd R-parity, *i.e.*, the Lightest Superparticle (LSP), is stable. Another consequence is that one can produce (or annihilate) superparticles only pairwise. These two points have important implications on the collider phenomenology and cosmology.

1.4.4 Soft Supersymmetry Breaking Terms

In addition to the integrations that arise from the superpotential Eq.(1.32), soft supersymmetry breaking terms should be added to the Lagrangian. Following the general classification in Eq.(1.26), and assuming the R-parity conservation, they are given by

$$\mathcal{L}_{\text{soft}} = \mathcal{L}_1 + \mathcal{L}_2\,, \tag{1.36}$$

$$\begin{aligned}
\mathcal{L}_1 &= -m_Q^{2ij}\tilde{Q}_i^*\tilde{Q}_j - m_U^{2ij}\tilde{U}_i^*\tilde{U}_j - m_D^{2ij}\tilde{D}_i^*\tilde{D}_j \\
&\quad -m_L^{2ij}\tilde{L}_i^*\tilde{L}_j - m_E^{2ij}\tilde{E}_i^*\tilde{E}_j - m_{H_u}^2|H_u|^2 - m_{H_d}^2|H_d|^2\,, \\
\mathcal{L}_2 &= -A_u^{ij}\lambda_u^{ij}\tilde{Q}_i\tilde{U}_j H_u - A_d^{ij}\lambda_d^{ij}\tilde{Q}_i\tilde{D}_j H_d - A_\ell^{ij}\lambda_e^{ij}\tilde{Q}_i\tilde{U}_j H_d + B\mu H_u H_d + c.c\,.
\end{aligned}$$

The mass-squared parameters for scalar quarks (squarks) and scalar leptons (sleptons) are all three-by-three hermitian matrices, while the trilinear couplings A^{ij} and the bilinear coupling B of mass dimension one are general complex numbers.

1.5 Experimental facts supporting Supersymmetry

1.5.1 Grand Unification

From the precise measurements of the gauge couplings performed by LEP [10], one interesting possibility is that the gauge couplings in the Standard Model $SU(3)_C \times SU(2)_L \times U(1)_Y$ may be embedded into a simple gauge group, such as $SU(5)$ or $SO(10)$, at some high energy scale, called *grand unification*. The gauge coupling constants at the energy scale $\mu \sim m_Z$ are approximately $\alpha_1^{-1} = 129$, $\sin^2\theta_W \sim 0.232$, and $\alpha_3 = 0.119$. In the $SU(5)$ normalization, the $U(1)$ coupling constant is given by $\alpha_1 = \frac{5}{3}\alpha' = \frac{5}{3}\alpha/\cos^2\theta_W$. It turns out that the gauge coupling constants become equal at $\mu \sim 2 \times 10^{16}$

GeV if the MSSM particle content with mass $<\sim 1$ TeV is given (Figure 1.5). On the other hand, the three gauge coupling constants miss each other quite badly with the Standard Model particle content. Such a grand unification is realized by a supersymmetric theory with superpartners near the electroweak scale. This remarkable fact has been interpreted by many as a strong hint for a supersymmetric grand unified theory (SUSY GUT), especially since many theories beyond the Standard Model, the composite and technicolor approaches [11], seem now even more disfavored by the precise measurements at LEP and SLC.

1.5.2 The Muon Anomalous Magnetic Moment

Leptonic anomalous magnetic value, g, provides precision tests of the Standard Model and stringent constraints on potential "New Physics" effects. The $a_\mu \equiv (g-2)/2$ is currently about 1000 times less precise than a_e, however, it is much more sensitive to "New Physics" effects, since such contributions are generally proportional to m_ℓ^2. The $m_\mu^2/m_e^2 \sim 40{,}000$ enhancement more than compensates for the reduced experimental precision and makes a_μ a more sensitive probe of short-distance phenomena.

For the positive muon, the extraordinary measurements of a_μ has been made at the Brookhaven National Laboratory [4]. Combining results at BNL and the earlier CERN results, the difference between the weighted mean of the experimental results $a_\mu^{\rm exp} = 11659203\,(15)\times 10^{-10}$, and the theoretical value from the Standard Model, $a_\mu^{\rm SM}$, is

$$a_\mu^{\rm exp} - a_\mu^{\rm SM} = 43\,(16) \times 10^{-10}\,. \tag{1.37}$$

The error is the addition in quadrature of experimental and theoretical errors. The difference is 2.6 σ. In Figure 1.6, the five most recent measurements of a_μ are shown along with the Standard Model prediction.

There are many speculative theories which predict deviations from the Standard Model value for a_μ. The muon anomalous g value is particularly sensitive to Supersymmetry whose contributions to a_μ come from smuon-neutralino and sneutrino-chargino loops (see Figure 1.7). In the limit of large $\tan\beta$

$$|a_\mu^{\rm SUSY}| \sim 140 \times 10^{-11} \left(\frac{100{\rm GeV}}{\tilde{m}}\right)^2 \tan\beta\,, \tag{1.38}$$

where $\tilde{m}$ represents a typical SUSY particle mass. Giving an interpretation with Supersymmetry,

$$\tilde{m} \sim 120{-}400 \ \ {\rm GeV} \qquad\qquad (\tan\beta = 4{-}40). \tag{1.39}$$

Certainly, above experimental results which favor Supersymmetry does not constitute a proof of SUSY, nor can it serve as a substitute for the direct discovery of a SUSY particle. However, it is clearly very encouraging and should not be ignored.

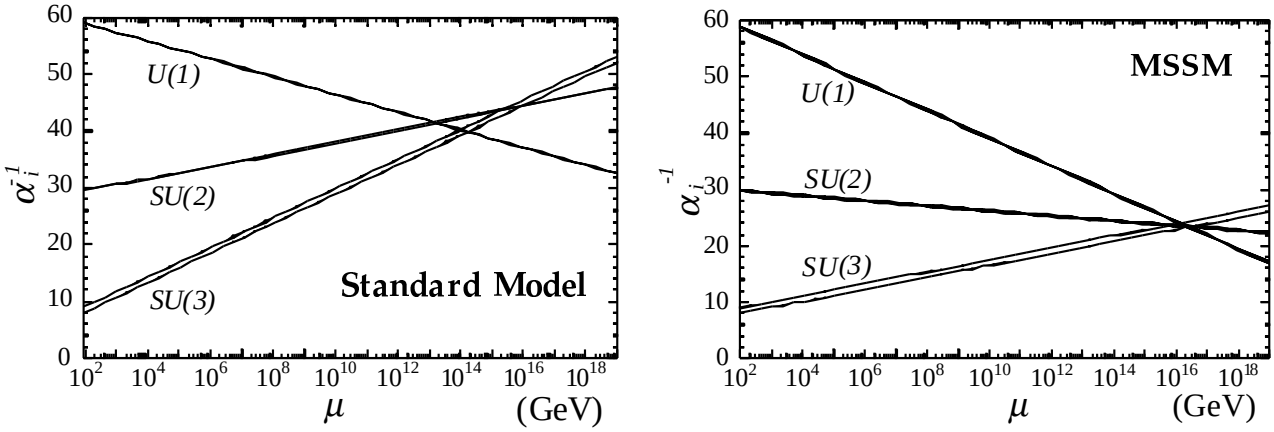

Figure 1.5: *Running of gauge coupling constants in the Standard Model and in the MSSM.*

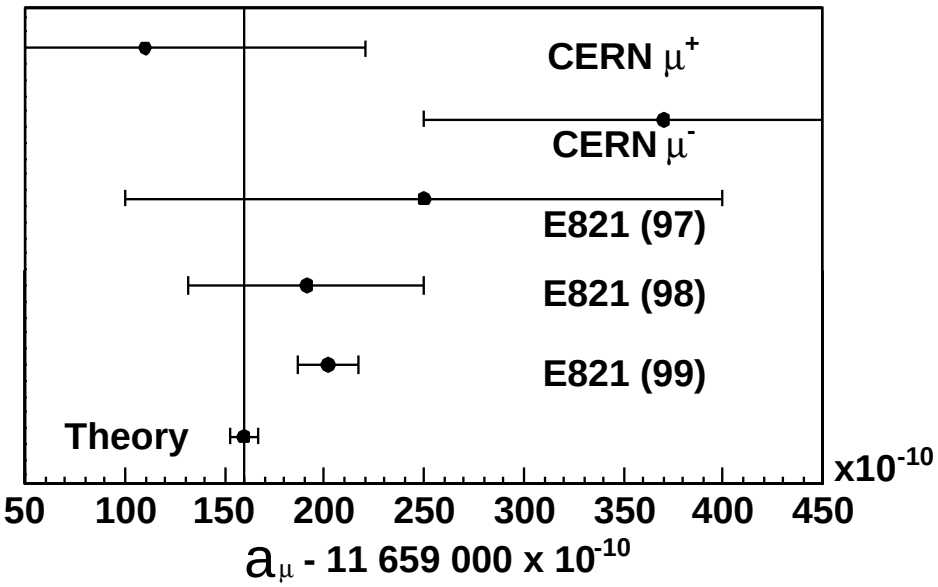

Figure 1.6: *Measurements of a_μ and the Standard Model prediction with their total errors.*

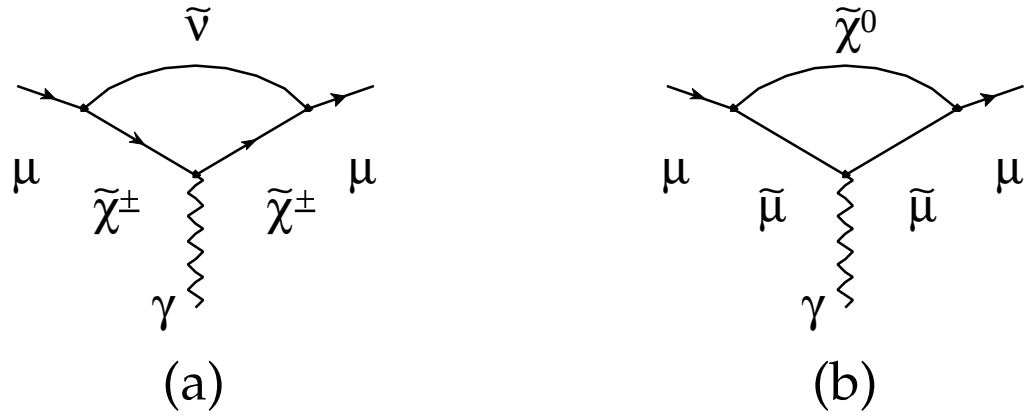

Figure 1.7: *Supersymmetric loops contributing to the muon anomalous magnetic moment; (a) for sneutrino-chargino loops and (b) for smuon-neutralino loops. They include two chargino and four neutralino states.*

Chapter 2

Gauge-Mediated Supersymmetry Breaking

2.1 Structure of models with Gauge-Mediated Supersymmetry Breaking (GMSB)

One of the most stringent problems for supersymmetric theories is to make flavor-invariant supersymmetry breaking masses for squarks and sleptons naturally. The flavor-breaking contributions to the soft terms are very dangerous because they might be inconsistent with experimental results of FCNCs. In case of the gravity-mediated theories, there is no obvious reason why the supersymmetry breaking soft terms for squarks and sleptons should be flavor-invariant.

On the other hand, in GMSB theories, soft terms are generated below the scale Λ_F, which is the new physics energy scale with unknown dynamics responsible for the flavor breaking. Therefore Yukawa couplings are the only relevant sources of the flavor violation, precisely as in the Standard Model. As a consequence, the GIM mechanism is fully operative and it can be generalized to a superGIM mechanism, involving ordinary particles and their supersymmetric partners. Since it is reasonable to expect that Λ_F is as large as the GUT or the Planck scales, in the gauge-mediated theories the flavor problem is naturally decoupled, in contrast to the case of gravity-mediated theories.

The first ingredient of these models is an *observable sector* which contains the usual quarks, leptons, gauge bosons, and two Higgs doublets, together with their supersymmetric partners. Then the models contain a sector responsible for the supersymmetry breaking, which is referred to as *hidden sector*. The supersymmetry breaking in the hidden sector is transmitted to the observable sector via a *messenger sector*. A chiral superfield X belonging to the hidden sector acquires a VEV along its scalar (S) and auxiliary (F) components:

$$< X >= S + \theta^2 F \,, \tag{2.1}$$

and couples at tree level to chiral superfields in the messenger sector, Φ_i and $\overline{\Phi}_i$. The interaction between Φ_i, $\overline{\Phi}_i$ and the chiral superfields X is given by the superpotential term

$$W = \lambda_i X \Phi_i \overline{\Phi}_i \,. \tag{2.2}$$

Here it is assumed that only one chiral superfield X. As a consequence, the spinor components of Φ_i and $\overline{\Phi}_i$ form a Dirac mass $\lambda_i S$, while the scalar components have a squared-mass matrix

$$\begin{pmatrix} |\lambda_i S|^2 & \lambda_i F \\ \lambda_i^* F^* & |\lambda_i S|^2 \end{pmatrix} \tag{2.3}$$

with eigenvalues $|\lambda_i S|^2 \pm |\lambda_i F|$. As can be seen, S VEV of the chiral superfield X induces the mass of fermion components of the messenger fields, while its F VEV generates the mass splitting between fermionic and bosonic components of the messenger fields. If F is non-zero, the messenger spectrum is not supersymmetric,

$$m_f = M_i \qquad \text{(for fermion)} \tag{2.4}$$

$$m_b = M_i \sqrt{1 \pm \frac{\Lambda_i}{M_i}} \qquad \text{(for bosons)}\,, \tag{2.5}$$

where $M_i = \lambda_i S$ and $\Lambda_i = F/S$. The parameter Λ/M_i sets the scalar for the fractional splitting between bosons and fermions. To avoid electroweak and color breaking in the messenger sector, $M_i > \Lambda$ is required.

The simplest messenger sector is described by N_f flavors of chiral superfields $\Phi_i, \bar{\Phi}_i (i = 1, ..., N_f)$ transforming the complete GUT multiplets in order to preserve a grand unification. In this case $M_{\rm GUT}$ is not modified by the presence of messenger fields at an intermediate scale, but the inverse gauge coupling strength $\alpha_{\rm GUT}^{-1}$ receives an extra contribution:

$$\delta\alpha_{\rm GUT}^{-1} = -\frac{N_m}{2\pi} \log \frac{M_{\rm GUT}}{M}\,, \tag{2.6}$$

where N_m is one of theoretical parameters, *messenger index* and it is given by

$$N_m = \sum_{i=1}^{N_f} n_i\,. \tag{2.7}$$

Here n_i is the Dynkin index of a gauge representation formed by messenger supermultiplets with normalization $n = 1$ for the $\Phi_i, \bar{\Phi}_i$ pair forming the fundamental representation of $SU(N)$. For example, $n = 1$ for single flavor of $\mathbf{5} + \bar{\mathbf{5}}$, and $n = 3$ for single flavor of $\mathbf{10} + \bar{\mathbf{10}}$. Index i enumerates flavors. Eq.(2.6) limits the messenger index. For messenger scale M as low as 100 TeV, perturbativity of gauge couplings up to the $M_{\rm GUT}$ scale requires N_m to be 5 at most.

Supermultiplets at observable sector degenerate at the tree level, since they do not directly couple to X. However, splittings arise at the quantum level because of gauge interactions between the observable and messenger fields. Vector boson and matter fermion masses are protected by the gauge invariance. On the other hand, gaugino, squark and sleptons can acquire masses consistently, once supersymmetry is broken. Gaugino masses are generated at one-loop, but squark and slepton masses can only arise at two-loops, since the exchange of both gauge and messenger particles is necessary. The corresponding Feynman diagrams are drawn in Figure 2.1.

From direct evaluation of the relevant Feynman diagrams, the supersymmetry breaking gaugino masses are

$$M_{\tilde{\lambda}_i}(M) = k_i \frac{\alpha_i(M)}{4\pi} \Lambda_G \qquad i = 1, 2, 3 \tag{2.8}$$

and sfermion masses are

$$m_{\tilde{f}}^2(M) = 2 \sum_{i=1}^{3} C_i^{\tilde{f}} k_i \left(\frac{\alpha_i(M)}{4\pi} \right)^2 \Lambda_S^2 \qquad i = 1, 2, 3 \tag{2.9}$$

at the messenger scale M. Here,

$$\Lambda_G = N_m \frac{F_i}{M_i} g\left(\frac{F_i}{M_i^2} \right), \tag{2.10}$$

$$g(x) = \frac{1}{x^2}[(1+x)\log(1+x)] + (x \to -x)\,, \tag{2.11}$$

$$\Lambda_S^2 = N_m \frac{F_i^2}{M_i^2} f\left(\frac{F_i}{M_i^2}\right), \tag{2.12}$$

$$f(x) = \frac{1+x}{x^2}\left[\log(1+x) - 2\mathrm{Li}_2\left(\frac{x}{1+x}\right) + \frac{1}{2}\mathrm{Li}_2\left(\frac{2x}{1+x}\right)\right] + (x \to -x)\,. \tag{2.13}$$

In the above formulae, $C_i^{\tilde{f}}$ are quadratic Casimir operators of sfermions $\tilde{f}$: $C = \frac{N^2-1}{2N}$ for the N-dimensional representation of $SU(N)$, and $C = Y^2 = (Q - T_3)^2$ for the $U(1)_Y$ factor. Coefficients k_i are normalized so that $k_i\alpha_i$ are equal at the GUT scale: $k_1 = \frac{5}{3}$ and $k_2 = k_3 = 1$. Both functions, $g(x)$ and $f(x)$, are very close to unity for $\Lambda << M$. The function $g(x)$ reaches the maximal value 1.4 at the limit of $x \to 1$. The function $f(x)$ is approximately equal to 1 for $x < 0.8$, and reaches the minimum value 0.7 at the limit of $x \to 1$.

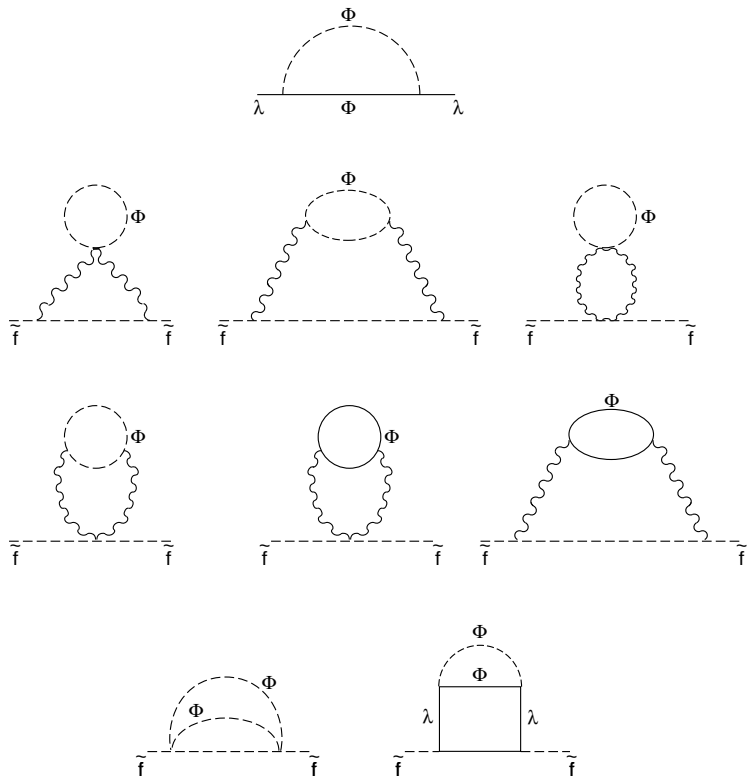

Figure 2.1: *Feynman diagram contributing to supersymmetry breaking gaugino (λ) and sfermion ($\bar{f}$). The scalar and fermionic components of the messenger field Φ are denoted by dashed and solid lines, respectively; ordinary gauge bosons are denoted by wavy lines.*

2.2 Phenomenology

It is essential for the studying the phenomenology of GMSB models to know the LSP and the NLSP (Next-Lightest SuperParticle) as well as the decay width of the NLSP.

2.2.1 The lightest SUSY particle

As a result of the spontaneous supersymmetry breaking, the physical spectrum contains a massless spin 1/2 fermion, the goldstino. When the globally supersymmetric theory is coupled to gravity and promoted to a locally supersymmetric theory, the goldstino provides the longitudinal modes of the spin 3/2 partner of the graviton. As a result of this "superhiggs" mechanism, the gravitino[1], $\widetilde{\mathrm{G}}$, acquires a supersymmetry breaking mass which is given by

$$m_{\widetilde{G}} = \frac{F_0}{\sqrt{3}M_{\mathrm{Planck}}} = C_{\mathrm{grav}}\frac{F}{\sqrt{3}M_{\mathrm{Planck}}} = C_{\mathrm{grav}}\left(\frac{\sqrt{F}}{100\ \mathrm{TeV}}\right)^2 \ \ 2.4\ \mathrm{eV}\,, \tag{2.14}$$

where $M_{\mathrm{Planck}} = (8\pi G_N)^{-1/2} = 2.4 \times 10^{18}$ GeV is the reduced Planck mass. The parameter F_0 is the total contribution of the supersymmetry breaking VEV of the auxiliary fields. While F_0 is the fundamental scale of the supersymmetry breaking, F is the scale of the supersymmetry breaking felt by the messenger particles (the mass splitting inside their supermultiplets). The ratio $C_{\mathrm{grav}} \equiv F_0/F$ depends on how the supersymmetry breaking is communicated to the messengers. The model-independent coefficient C_{grav} is always > 1.

2.2.2 The Next-lightest SUSY particle

In a large class of models with low-energy supersymmetry breaking, the NLSP will either be the lightest neutralino ($\widetilde{\chi}_1^0$) or the lightest stau ($\widetilde{\tau}_1^{\pm}$) mass eigenstate[2]. The stau mixing angle $\theta_{\tilde{\tau}}$ is such that

$$\begin{pmatrix} \widetilde{\tau}_1 \\ \widetilde{\tau}_2 \end{pmatrix} = \begin{pmatrix} \cos\theta_{\tilde{\tau}} & \sin\theta_{\tilde{\tau}} \\ -\sin\theta_{\tilde{\tau}} & \cos\theta_{\tilde{\tau}} \end{pmatrix} \begin{pmatrix} \widetilde{\tau}_L \\ \widetilde{\tau}_R \end{pmatrix} \tag{2.15}$$

with $m_{\widetilde{\tau}_1} < m_{\widetilde{\tau}_2}$ and $0 \le \theta_{\tilde{\tau}} \le \pi$. The sign of $\cos\theta_{\tilde{\tau}}$ mainly depends on the sign of μ (the superpotential Higgs mass parameter) through the off-diagonal term $m_\tau(A_\tau - \mu\tan\beta)$ in the stau (mass)^2 matrix. The term $\mu\tan\beta$ typically dominates over the contribution from the soft trilinear scalar couplings A_τ in GMSB models, because the latter are very small at the messenger scale and the effect of renormalization group running are usually not very large. For this reason, it is very unlikely that cancellation between A_τ and $\mu\tan\beta$ can lead to $\cos\theta_{\tilde{\tau}} \sim 0$ in these models, unless the scale of the supersymmetry breaking is very high. On the other hand, the selectron and smuons also mix exactly analogously to Eq.(2.15). Their mixings are generally much smaller, with $\cos\theta_{\tilde{\mu}}/\cos\theta_{\tilde{\tau}} \sim y_\mu/y_\tau \sim 0.06$ and $\cos\theta_{\tilde{e}}/\cos\theta_{\tilde{\tau}} \sim y_e/y_\tau \sim 3\times10^{-4}$. Therefore, in most cases one can just treat the lighter selectron and smuon mass eigenstates as nearly unmixed and degenerate states, $\widetilde{e}_1^{\pm} \sim \widetilde{e}_R^{\pm}$ and $\widetilde{\mu}_1^{\pm} \sim \widetilde{\mu}_R^{\pm}$.

Assuming R-parity conservation, all supersymmetric particles will cascade to the NLSP. Therefore, the nature of the NLSP determines the signatures in collider experiments and also some cosmological properties of gauge mediation.

The correspoinding interaction Lagrangian is

$$\mathcal{L} = -\frac{1}{F_0}J_Q^\mu \partial_\mu \tilde{G}\,, \tag{2.16}$$

where J_Q^μ is the supercurrent [6]. This shows how the goldstino interacts with derivative couplings suppressed by $1/F_0$.

[1] spin $\pm$ 3/2 components only couple with gravitational strength and the particle which is relevant to accelerator phenomenology is not *gravitino* but *goldstino*. However, *gravitino* is used as a generic term of *goldstino* and *gravitino*.

[2] In a very restricted region of parameters, the sneutrino can be the NLSP.

Neutralino NLSP

When the lightest neutralino $\widetilde{\chi}_1^0$ is the NLSP, $\widetilde{\chi}_1^0$ mostly decays into $\gamma\widetilde{\mathrm{G}}$ if R-parity is conserved. The neutralino has, in most cases, a dominant B-ino component, since the ratio μ/M_1 is typically larger than one.

NLSP $\widetilde{\chi}_1^0$ decay rate is expressed by

$$\Gamma(\widetilde{\chi}_1^0 \to \gamma\widetilde{G}) = \frac{\kappa_\gamma m_{\widetilde{\chi}_1^0}^5}{16\pi F^2 C_{\rm grav}^2} = \frac{\kappa_r}{C_{\rm grav}}\left(\frac{m_{\widetilde{\chi}_1^0}}{100\ \mathrm{GeV}}\right)^5\left(\frac{100\ \mathrm{TeV}}{\sqrt{F}}\right)^4 2\times 10^{-3}\quad \mathrm{eV}\,. \tag{2.17}$$

If the decays are allowed kinematically, $\widetilde{\chi}_1^0$ can decay into $\mathrm{Z}^0\gamma$ or $h^0\gamma$.

The ratios of decay widths to $\Gamma(\widetilde{\chi}_1^0 \to \gamma\widetilde{\mathrm{G}})$ are

$$\frac{\Gamma(\widetilde{\chi}_1^0 \to \mathrm{Z}^0\widetilde{G})}{\Gamma(\widetilde{\chi}_1^0 \to \gamma\widetilde{G})} = \frac{\kappa_Z}{\kappa_\gamma}\left(1-\frac{m_{\mathrm{Z}^0}^2}{m_{\widetilde{\chi}_1^0}^2}\right)^4, \tag{2.18}$$

$$\frac{\Gamma(\widetilde{\chi}_1^0 \to h^0\widetilde{G})}{\Gamma(\widetilde{\chi}_1^0 \to \gamma\widetilde{G})} = \frac{\kappa_h}{\kappa_\gamma}\left(1-\frac{m_h^2}{m_{\widetilde{\chi}_1^0}^2}\right)^4, \tag{2.19}$$

$$\kappa_\gamma = |N_{11}\cos\theta_W + N_{12}\sin\theta_W|^2\,, \tag{2.20}$$

$$\kappa_Z = |N_{11}\sin\theta_W - N_{12}\cos\theta_W|^2 + \frac{1}{2}|N_{13}\cos\beta - N_{14}\sin\beta|^2\,, \tag{2.21}$$

$$\kappa_h = |N_{13}\sin\alpha - N_{14}\cos\alpha|^2\,, \tag{2.22}$$

where $N_{1i}(i=1,2,3,4)$ are the $\widetilde{\chi}_1^0$ components, which correspond to the photino, zino and two neutral higgsinos in sequence and $\tan 2\alpha = \tan 2\beta(m_A^2+m_{\mathrm{Z}^0}^2)/(m_A^2-m_{\mathrm{Z}^0}^2)$. The decay mode into photon and gravitino is very likely to dominate. Even if the decay modes into the Z^0 boson or the neutral Higgs boson are kinematically allowed, they are suppressed by the β^8 phase-space factor. If $\widetilde{\chi}_1^0$ is mainly B-ino, $\kappa_Z/\kappa_\gamma = 0.3$ and κ_h/κ_γ is negligible.

Co-sleptons NLSP

The termination of superpartner decay chain depends crucially on the mass differences between $\widetilde{\chi}_1^0, \widetilde{\tau}_1^\pm$, and $\widetilde{\ell}_R^\pm$ ($\widetilde{\ell}_R^\pm$ is a generic notation for $\widetilde{e}_R^\pm$ or $\widetilde{\mu}_R^\pm$.) Among the three generations of right-handed sleptons, $\widetilde{\tau}_1^\pm$ is the lightest because of mixing effects proportional to m_τ in the stau mass matrix.

Here one must distinguish between several qualitatively distinct scenarios. If $\tan\beta$ is not too large, then $\widetilde{e}_R^\pm$ and $\widetilde{\mu}_R^\pm$ will not be much heavier than $\widetilde{\tau}_1^\pm$, and the decay $\widetilde{\ell}_R^\pm \to \ell^\pm\tau^\pm\widetilde{\tau}_1^\mp$ and $\widetilde{\ell}_R^\pm \to \ell^\pm\widetilde{\chi}_1^0$ will not be kinematically open. This case is called *slepton co-NLSP scenario*, and each of $\widetilde{e}_R^\pm, \widetilde{\mu}_R^\pm$ and $\widetilde{\tau}_1^\pm$ may decay according to $\widetilde{e}_R^\pm \to e^\pm\widetilde{\mathrm{G}}$, $\widetilde{\mu}_R^\pm \to \mu^\pm\widetilde{\mathrm{G}}$ and $\widetilde{\tau}_1^\pm \to \tau^\pm\widetilde{\mathrm{G}}$, possibly with a large gravitino mass [3].

The NLSP slepton decay rate is

$$\Gamma(\widetilde{\ell} \to \ell\widetilde{G}) = \frac{m_{\widetilde{\ell}}^5}{16\pi F^2 C_{\rm grav}^2} = \frac{1}{C_{\rm grav}^2}\left(\frac{m_{\widetilde{\ell}}}{100\ \mathrm{GeV}}\right)^5\left(\frac{100\ \mathrm{TeV}}{\sqrt{F}}\right)^4 2\times 10^{-3}\quad \mathrm{eV}. \tag{2.23}$$

[3]The three body decay of $\widetilde{\ell}_R \to \nu_\ell\bar{\nu}_\tau\widetilde{\tau}_1$ through off-shell charginos, $\widetilde{\chi}_i^\pm$. However, these decays are strongly suppressed by the phase space and because the coupling of $\widetilde{\ell}_R$ to $\ell\widetilde{\chi}_i^\pm$.

Stau NLSP

For larger values of $\tan\beta$, enhanced stau mixing renders $\widetilde{\tau}_1$ lighter than $\widetilde{e}_R$ and $\widetilde{\mu}_R$ by more than m_τ. In this *stau NLSP scenario*, all supersymmetric decay chains should terminate in $\widetilde{\tau}_1 \to \tau\widetilde{\mathrm{G}}$, again possibly with a large gravitino mass. If the mass ordering is $m_{\widetilde{\mu}_R} - m_\mu$ and/or $m_{\widetilde{e}_R} - m_e > m_{\widetilde{\chi}_1^0}$, then the two-body decays $\widetilde{\mu}_R \to \mu\widetilde{\chi}_1^0$ and/or $\widetilde{e}_R \to e\widetilde{\chi}_1^0$ will be open and will dominate. Even if $m_{\widetilde{\chi}_1^0} > m_{\widetilde{\ell}_R} - m_\ell > m_{\widetilde{\tau}_1} + m_\tau$, $\widetilde{\mu}_R$ and/or $\widetilde{e}_R$ can decay through off-shell neutralinos in three-body decays, $\widetilde{\mu}_R \to \mu\tau\widetilde{\tau}_1$ and/or $\widetilde{e}_R \to e\tau\widetilde{\tau}_1$. These three-body decays may dominate over two-body decays, $\widetilde{\mu}_R \to \mu\widetilde{\mathrm{G}}$ and $\widetilde{e}_R \to e\mathrm{G}$. The analytical result for the three-body decay widths of $\widetilde{e}_R$ and $\widetilde{\mu}_R$ is reported in [47].

Lifetime

As the gravitino coupling to the NLSP is suppressed by $1/F$, the lifetime of the NLSP is proportional to F^2. From the NLSP decay rate, see Eq.(2.17) and 2.23, the average distance traveled by the NLSP with mass m and produced with energy E is obtained;

$$L = \frac{1}{\kappa_\gamma}\left(\frac{100\ \mathrm{GeV}}{m}\right)^5\left(\frac{\sqrt{FC_{\mathrm{grav}}}}{100\ \mathrm{TeV}}\right)^4\sqrt{\frac{E^2}{m^2}-1}\times 10^{-2} \qquad \mathrm{cm}\,, \tag{2.24}$$

where κ_gamma is given in Eq. 2.20 for $\widetilde{\chi}_1^0$ and it is equal to one for $\widetilde{\tau}_1^\pm$. Mainly depending on the unknown value of $\sqrt{FC_{\mathrm{grav}}}$, the NLSP can decay within microscopic distances, inside the detector or well outside of the detector. The NLSP decay length can generally be divided into three relevant ranges. The first is *prompt decay* which can not be resolved as secondary vertices, and therefore appears to originate from the interaction. Since SUSY particles are produced in pair the signatures are two hard particles coming from the NLSP decays, significant missing energy carried by a gravitino pair, and possibly other particles from cascade decays to the NLSPs.

The second range of decay length is macroscopic but within the detector. In this case the particles arising from the NLSP decay do not necessarily point back to the interaction region. For a neutralino decay $\widetilde{\chi}_1^0 \to \gamma\widetilde{\mathrm{G}}$ this leads to "displaced photons" (Photons not originating from the $\mathrm{e^+e^-}$ interaction point). For $\widetilde{\chi}_1^0$ NLSP displaced decay $\widetilde{\chi}_1^0 \to \mathrm{Z}^0\widetilde{\mathrm{G}}$ or $\widetilde{\chi}_1^0 \to \mathrm{h}^0\widetilde{\mathrm{G}}$, secondary vertices arise with decay products whose invariant mass can be identified with the parent h^0 or Z^0 boson. This generally requires a special analysis to identify high momentum particles which form secondary vertices. In some cases this can greatly reduce background. For $\widetilde{\ell}$, NLSP displaced decays $\widetilde{\ell} \to \ell\widetilde{\mathrm{G}}$ inside the inner tracking region, will yield charged particle tracks which do not point back to the interaction region. When a non-relativistic slepton traverses at least part of the tracking region before its decay $\widetilde{\ell} \to \ell\widetilde{\mathrm{G}}$, it gives a highly ionizing track (HIT) with a "kink" to a minimum ionizing track or tau jet.

Observation of a macroscopic decay length for any NLSP type would be a hint for low-scale supersymmetry breaking. In addition, a measure of the decay length distribution, along with the superpartner mass and identity, would essentially give a model independent measure of the supersymmetry breaking scale.

The final range of NLSP decay lengths is well outside the detector. A neutralino NLSP which decays well outside the detector appears as a missing energy.

A slepton NLSP which traverses the detector is generally not ultra-relativistic and therefore appears as a HIT. Since sleptons are produced in pairs, the resulting signature is HIT pairs often without significant missing energy, and possibly with other particles from cascade decays.

2.3 Search at e^+e^- colliders

In this report, it is assumed that $\widetilde{\chi}_1^0$ is the NLSP with prompt decaying into $\gamma\widetilde{G}$. The lightest sleptons $\widetilde{\ell}_1^{\pm}$ (= $\widetilde{e}_R^{\pm}, \widetilde{\mu}_R^{\pm}, \widetilde{\tau}_1^{\pm}$), the lightest chargino $\widetilde{\chi}_1^{\pm}$ and the second lightest neutralino $\widetilde{\chi}_2^0$ can be the next lightest sparticle to the NLSP, called NNLSP, which depends on theoretical parameters. In case that the NNLSP mass is light enough to be produced at LEP2 energies, cascade decays from $\widetilde{\chi}_1^+\widetilde{\chi}_1^-$, $\widetilde{\ell}_1^+\widetilde{\ell}_1^-$ and $\widetilde{\chi}_1^0\widetilde{\chi}_2^0$ productions, are expected. Figure 2.2 shows diagrams for these production processes. $\widetilde{\chi}_1^{\pm}$ will be pair-produced in e^+e^- collisions through a virtual Z^0 or γ in the s-channel. For the wino component there is an additional production process through scalar electron neutrinos,$\tilde{\nu}_e$, exchanged in the t-channel. Neutralino pairs, $\widetilde{\chi}_1^0\widetilde{\chi}_2^0$, can be produced through an s-channel virtual Z^0, or by t-channel scalar electron, $\tilde{e}$, exchange. For slepton pair production $\widetilde{\ell}_1^+\widetilde{\ell}_1^-$ they are produced through a virtual Z^0 and γ exchange in s-channel. A pair of selectrons is produced by t-channel $\widetilde{\chi}_i^0$ exchange as well.

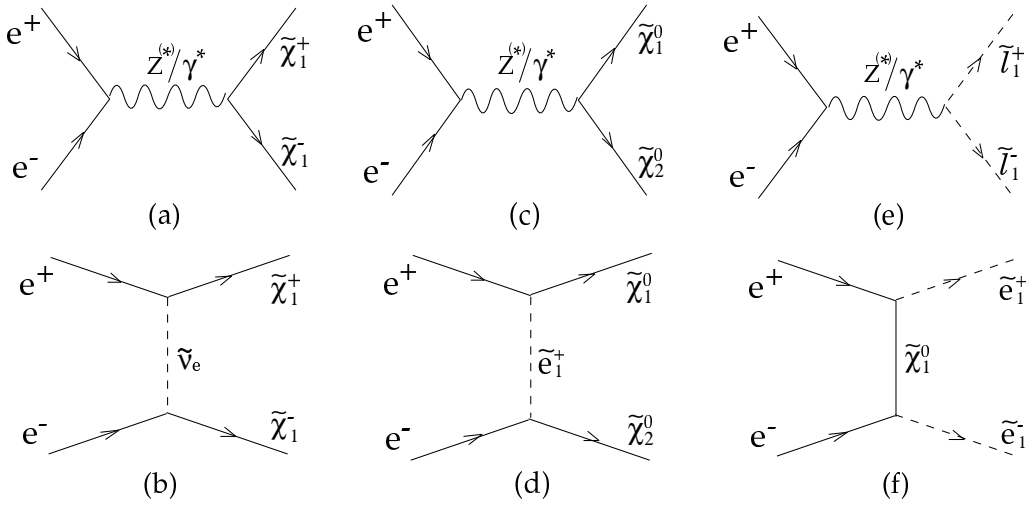

Figure 2.2: *(a)* $\widetilde{\chi}_1^+\widetilde{\chi}_1^-$ *via s-channel* Z^0/γ *exchange, (b)* $\widetilde{\chi}_1^+\widetilde{\chi}_1^-$ *via* t*-channel* $\tilde{\nu}_e$ *exchange, (c)* $\widetilde{\chi}_1^0\widetilde{\chi}_2^0$ *via s-channel* Z^0 *exchange, (d)* $\widetilde{\chi}_1^0\widetilde{\chi}_2^0$ *via* t*-channel* $\widetilde{e}^{\pm}$ *exchange, (e)* $\widetilde{\ell}^+\widetilde{\ell}^-$ *via s-channel* Z^0/γ *exchange and (f)* $\widetilde{e}^+\widetilde{e}^-$ t*-channel* $\widetilde{\chi}_1^0$ *exchange.*

2.3.1 Experimental topologies

In the minimal GMSB model, $\widetilde{\chi}_1^0$ is the candidate of the NLSP and decays mostly by $\widetilde{\chi}_1^0 \to \gamma\widetilde{G}$ if R-parity is conserved. Assuming it decays in a detector, signatures for the $\widetilde{\chi}_1^0\widetilde{\chi}_2^0$ production give two photons plus X with missing energy, where X arises from cascade decays to $\widetilde{\chi}_1^0$.
In the rest frame of the decaying $\widetilde{\chi}_1^0$, the photon is approximately produced isotropically[4] with energy equal to $m_{\widetilde{\chi}_1^0}/2$ and the distribution of photon energy is about rectangular. Both the missing energy and photon energy depend on γ-factor of $\widetilde{\chi}_1^0$ and the NNLSP, but they are typically greater than $m_{\widetilde{\chi}_1^0}/2$. For instance, in the case of slepton pair production where $\widetilde{\ell}$ decays into $\widetilde{\chi}_1^0\ell$ and then, $\widetilde{\chi}_1^0 \to \gamma\widetilde{G}$, the ranges of lepton and photon energies are given by following formulae:

$$E_{\ell\ \mathrm{min}}^{\ \mathrm{max}} = \frac{E_{\mathrm{beam}}}{2m_{\widetilde{\ell}}^2}\left(m_{\widetilde{\ell}}^2 - m_{\widetilde{\chi}_1^0}^2\right)\left(1 \pm \frac{m_{\widetilde{\ell}}^2}{E_{\mathrm{beam}}^2}\right) \quad \mathrm{GeV}, \tag{2.25}$$

[4]The photon distribution depends on the helicity of $\widetilde{\chi}_1^0$, which arises from the NNLSP decays. The produced NNLSPs are unpolarized in many parameter space in the minimal GMSB.

$$\mathrm{E}_{\gamma\ \mathrm{min}}^{\ \mathrm{max}} = \frac{\mathrm{m}_{\widetilde{\chi}_1^0}}{2}\left(1 \pm \frac{\mathrm{m}_{\widetilde{\ell}}^2 - \mathrm{m}_{\widetilde{\chi}_1^0}^2}{\mathrm{m}_{\widetilde{\ell}}^2 + \mathrm{m}_{\widetilde{\chi}_1^0}^2}\right)\left(1 \pm \left(1 - \frac{\mathrm{m}_{\widetilde{\ell}}^2}{E_{\mathrm{beam}}^2}\right)^{1/2}\right) \quad \mathrm{GeV}\,, \tag{2.26}$$

where E_{beam} is the energy of the electron (positron). The mass difference between the NNLSP and the NLSP, ΔM, is the most effective to characterize kinematics of an event. The region of energy distribution for lepton is expressed by $\Delta M/2\,(1 \pm \alpha)$, with $\alpha \sim 0.1$-10. The photon energy is distributed around $\mathrm{m}_{\widetilde{\chi}_1^0}/2$, therefore one can say it depends on ΔM when $\mathrm{m}_{\widetilde{\ell}}$ is fixed. As the ΔM becomes smaller, the photon energy becomes large, and on the contrary to it, the event visible energy excluding the photons decreases.
In case of slepton productions the event multiplicity is always low, while it depends on decay of Z^0 and $\mathrm{W}^\pm$ bosons for neutralino and chargino productions, respectively.

Search for sleptons In the case of $\widetilde{\ell}_1^+\widetilde{\ell}_1^-$ pair production the following cascade decay is expected:

$$\begin{array}{l} \mathrm{e}^+\mathrm{e}^- \longrightarrow \widetilde{\ell}_1^+\,\widetilde{\ell}_1^- \\ \quad\big|\ \ \hookrightarrow \widetilde{\chi}_1^0\,\ell^+ \\ \quad\big|\qquad\quad\big| \\ \quad\big|\qquad\quad\hookrightarrow \gamma\,\widetilde{G} \\ \quad\hookrightarrow \widetilde{\chi}_1^0\,\ell^- \\ \qquad\quad\big| \\ \qquad\quad\hookrightarrow \gamma\,\widetilde{G} \end{array}$$

Of course, the direct decay to $\ell\widetilde{\mathrm{G}}$,

$$\widetilde{\ell} \to \ell + \widetilde{G}$$

is also possible. However, this decay width is usually smaller than that of $\widetilde{\ell} \to \widetilde{\chi}_1^0 + \ell$ unless the latter is suppressed by the phase space, that is, ΔM is very small ($<$ a few GeV).

Search for neutralino When $\widetilde{\chi}_2^0\widetilde{\chi}_1^0$ are produced, $\widetilde{\chi}_2^0$ and $\widetilde{\chi}_1^0$ decay as follows;

$$\begin{array}{l} \mathrm{e}^+\mathrm{e}^- \longrightarrow \widetilde{\chi}_1^0\,\widetilde{\chi}_2^0 \\ \quad\big|\ \ \hookrightarrow \widetilde{\chi}_1^0\,\mathrm{Z}^0 \\ \quad\big|\qquad\quad\big| \\ \quad\big|\qquad\quad\hookrightarrow q\bar{q} \text{ or } \ell^+\ell^- \\ \quad\big|\qquad\quad\big| \\ \quad\big|\qquad\quad\hookrightarrow \gamma\,\widetilde{G} \\ \quad\hookrightarrow \gamma\,\widetilde{G} \end{array}$$

and an event topology depends on the Z^0 decay. If Z^0 decays into $\mathrm{q\bar{q}}$, "*jets plus two photons with missing energy*" can be observed in the final state. As ΔM becomes smaller, jets become soft, namely, low-multiplicity and small energy. In the case of leptonic Z^0 decay, the event topology is very similar to that of slepton pair production. They are shown in Figure 2.3 (1,2) schematically.
When Z^0 decays to a pair of neutrinos, the final state is acoplanar photons. This case is not considered in the analysis.

Search for chargino Chargino pairs may also be produced at LEP2 energy with large cross-section. Assuming that $\widetilde{\chi}_1^{\pm}$ always decays into $\widetilde{\chi}_1^0 \mathrm{W}^{\pm}$ by 100 %, the following cascade decay is expected:

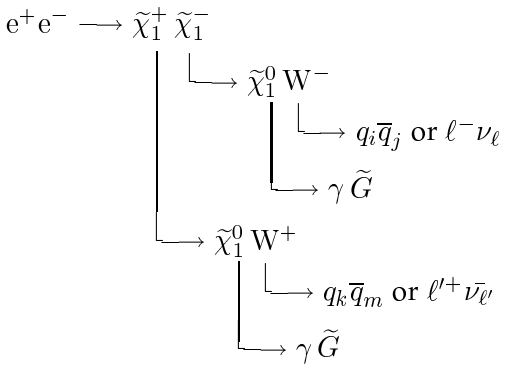

There appear three types of topologies in final states according to the decay mode of $\mathrm{W}^{\pm}$ as schematically shown in Figure 2.3(3)(4)(5). As mentioned in the neutralino case, if both $\mathrm{W}^{\pm}$'s decay into leptons, the final state looks like that of slepton pair production.

If the mass of slepton is lighter than that of $\widetilde{\chi}_1^{\pm}$, it is also possible that $\widetilde{\chi}_1^{\pm}$ performs a cascade decay as shown below.

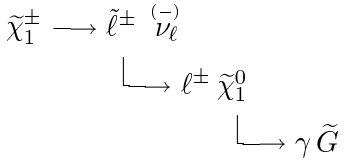

In addition, if $\widetilde{\nu}_\ell$ is lighter than $\widetilde{\chi}_1^{\pm}$, the following decay is also possible.

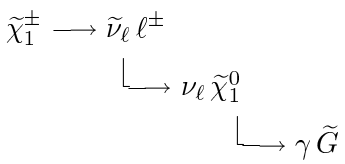

Both of them have "*two photons plus two leptons with missing energy*", and they are similar to the slepton pair production topologically. These branching ratios are free parameters, however, within the minimal GMSB, the branching fraction of $\widetilde{\chi}_1^{\pm} \to \mathrm{W}^{\pm} \widetilde{\chi}_1^0$ is usually larger than the others.

2.3.2 Background processes at LEP2

The signals as presented in the previous section can be broadly classified into two categories:

- **low-multiplicity**
  - slepton
  - chargino with two leptonic W decays
  - neutralino with leptonic Z^0 decay
- **high-multiplicity**
  - chargino with at least one hadronic W decay
  - neutralino with hadronic Z^0 decay

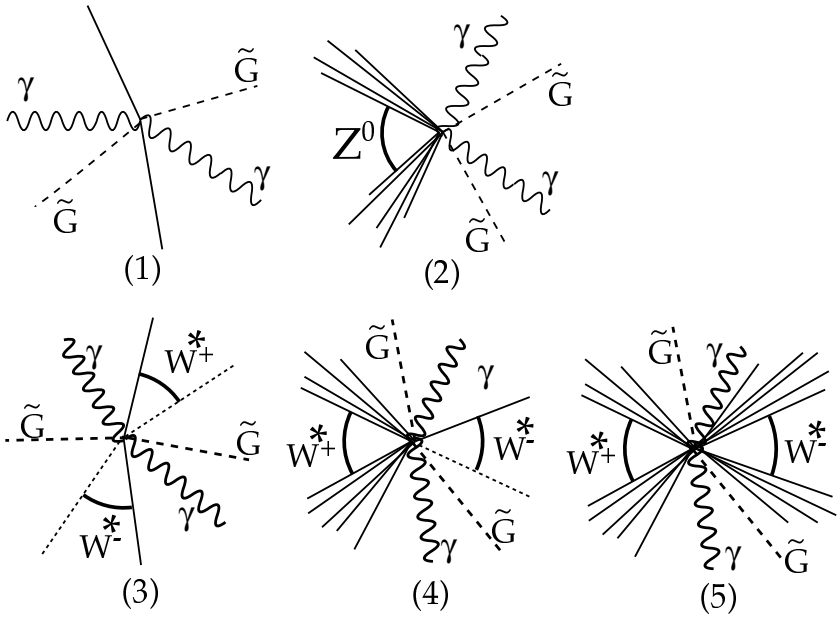

Figure 2.3: *Schematic views of event topologies for $\tilde{\chi}_1^0\tilde{\chi}_2^0$ and $\tilde{\chi}_1^+\tilde{\chi}_1^-$ productions. In the case of $\tilde{\chi}_1^0\tilde{\chi}_2^0$ with $\tilde{\chi}_1^0\mathrm{Z}^0$decays of $\tilde{\chi}_2^0$ followed by $\gamma\tilde{\mathrm{G}}$ decays of the $\tilde{\chi}_1^0$, (1) for hadronic decay of $\mathrm{Z}^{0(*)}$, and (2) for leptonic decay except invisible decay of $\mathrm{Z}^{0(*)}$. In case of $\tilde{\chi}_1^+\tilde{\chi}_1^-$ with $\tilde{\chi}_1^0\mathrm{W}^\pm$decays of $\tilde{\chi}_1^\pm$ followed by $\gamma\tilde{\mathrm{G}}$ decays of the $\tilde{\chi}_1^0$. For the decays of $\tilde{\chi}_1^\pm$ only through $\mathrm{W}^\pm$, rates for (3),(4) and (5) are in the ratio 45 % : 44 % : 11 %, where (3) for both $\mathrm{W}^\pm$decaying to hadrons, (4) for one to hadrons and the other to leptons and (5) for both of leptons.*

All signals have two energetic photons and missing energy, which are useful for extracting signal events from large amount of background events. In the case of the low-multiplicity signal, the main background comes from the tau pair production process, while multihadronic process and four-fermion $\mathrm{q\bar{q}}\ell\bar{\nu}_\ell$ process contaminate with the high-multiplicity signal.

Tau pair process

The process $\mathrm{e^+e^-} \to \tau\tau$ can be the dominant background source for the low-multiplicity signal. Neutrinos from tau decays cause missing energy. At cms energies above the Z^0 mass, initial state radiation (ISR) photons are emitted to reduce the effective cms energy to m_{Z^0}. Such an event is called a "*radiative-return*" event, and the photon energy is given by

$$E_\gamma = \frac{s - m_{\mathrm{Z}^0}^2}{2\sqrt{s}}\,. \tag{2.27}$$

Even if two energetic and isolated photons are required, radiative-return tau pair events with final state radiation (FSR), another ISR or a neutral hadron can fake the low multiplicity signal events.

Multihadronic process

Multihadronic events with a photon from a radiative-return process can be the main background for high-multiplicity signals. This process has a sizable production cross-section, as much as ~ 80 pb at $\sqrt{s} = 206$ GeV. Ideally such an event has no missing energy, however poor detector resolution and

particle(s) escaping in the beam direction induce missing energy as well as neutrinos from semileptonic decays of heavy quarks. Neutral hadrons and photons emitted from quark and hadron (FSR) as well as ISR fake a signal photon.

Four-fermion $q\bar{q}\ell\bar{\nu}_\ell$ process

The cross-section of four-fermion $q\bar{q}\ell\bar{\nu}_\ell$ events is not large compared to multihadronic events, but it is also a serious background for the high-multiplicity signal. A neutrino from W decay causes a considerable missing energy. Similarly, an event with a neutral hadron, FSR emitted from a jet/lepton and ISR can be selected as a signal.

Figure 2.4 shows diagrams of dominant background processes and some cross-sections of the Standard Model processes are presented in Figure 2.5.

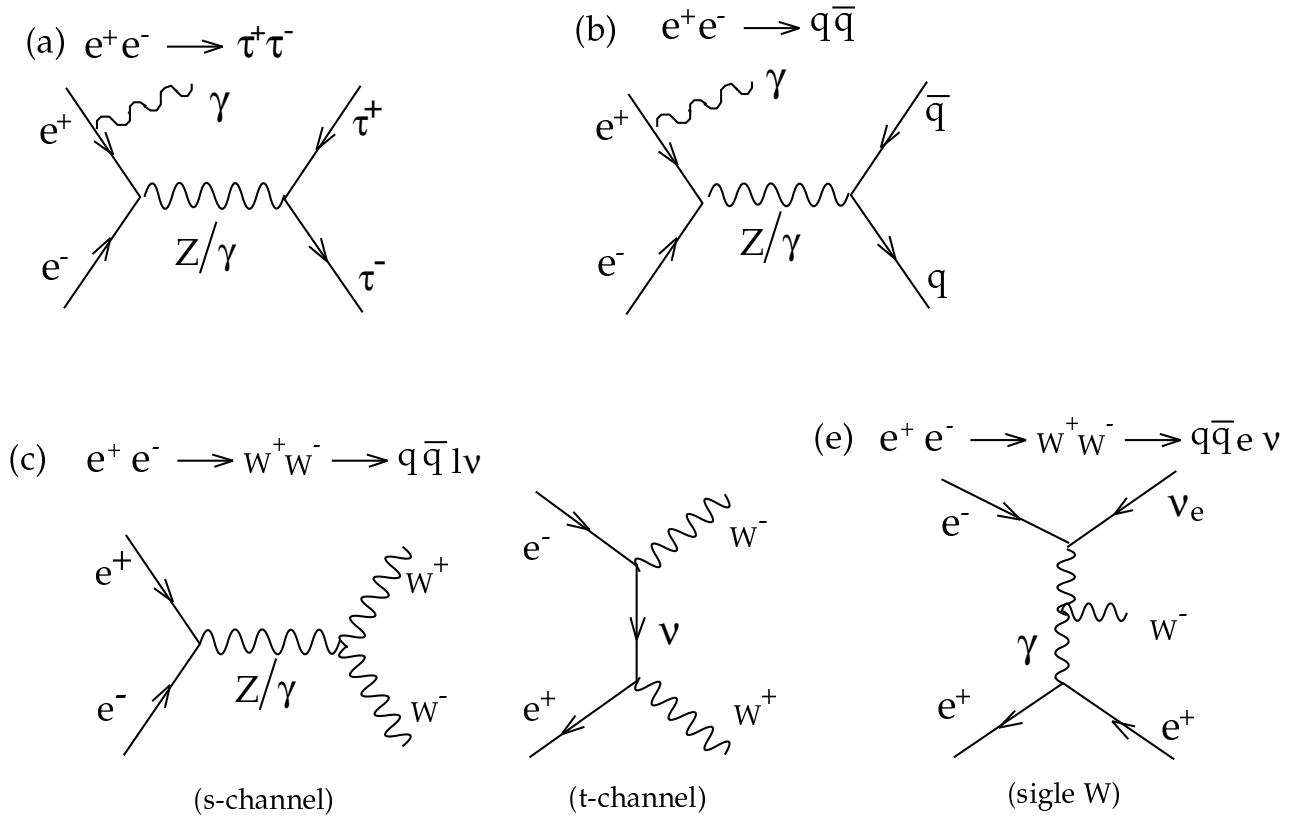

Figure 2.4: *Diagrams contributing to the Standard Model background processes: (a) tau pair process, (b) multihadronic process, (c) four-fermion $q\bar{q}\ell\bar{\nu}_\ell$ process from W^+W^- via Z^0/γ exchange in s-channel and electron neutrino exchange in t-channel, and (d) four-fermion $q\bar{q}e\nu_e$ process from single W process.*

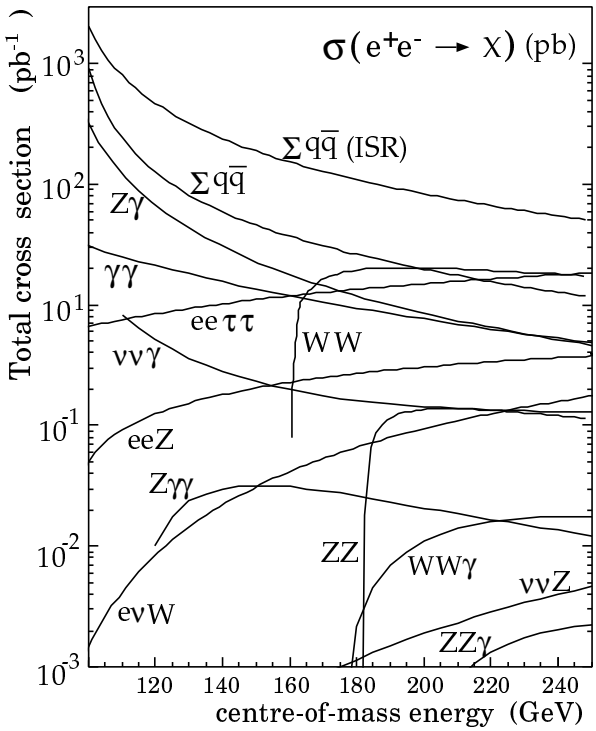

Figure 2.5: *The cross-sections of the Standard Model background processes versus the* e^+e^- *cms energy.*

Chapter 3

The LEP Collider and the OPAL Detector

3.1 The LEP collider

The CERN Large Electron Positron (LEP) collider is a 26.67 km circumference e^+e^- storage ring across the border between Switzerland and France. A schematic view of the LEP accelerator is shown in Figure 3.1.

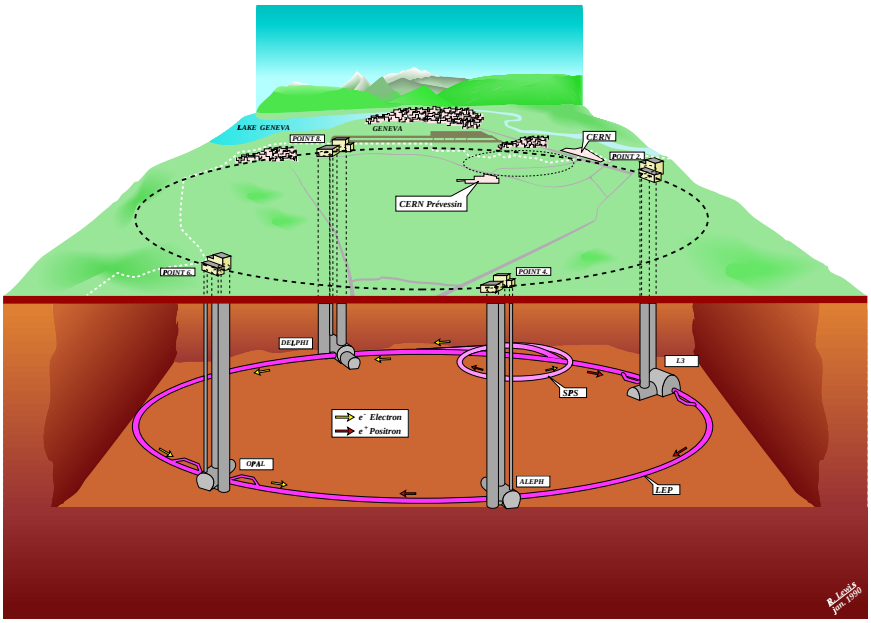

Figure 3.1: *A schematic view of LEP* e^+e^- *collider.*

A decade of successful operation of the LEP collider provided a wealth of precision data on the electroweak and on the strong interactions, through a multitude of e^+e^- annihilation final states which are recorded by four multi-purpose detectors, ALEPH [13] , DELPHI [14] L3 [15] and OPAL [16]. In the phase which is called LEP1, from 1989 to 1995, the collider was operated at the cms energy near the Z^0 resonance ($\sim$ 91 GeV). Measurements of s-dependent cross sections around Z^0 resonance provide model independent results (mass of the Z^0, the Z^0 total and partial decay widths, and the fermion pole cross-sections) and verify the Standard Model with high accuracy. Since 1995, the LEP collider operated at energies above the Z^0 resonance. In 1996, after LEP running at energies of 130–136 GeV (LEP1.5), 144 superconducting cavities were installed for the operation above the W^+W^- production threshold (LEP2). The LEP succeeded in raising up the cms energy with additional supercon-

ducting cavities, and offered a plenty of data at high energies, which was essential for new particle searches. The highest cms energy was 209 GeV achieved in 2000. LEP was closed on November 2nd in 2000 and a total integrated luminosity collected at energies above Z^0 resonance amounted to 700 pb^{-1} for each experiment. A brief summary of the structure of the LEP and the accelerating system for LEP2 are described below.

3.1.1 Structure

The LEP storage ring consists of eight straight sections connected by the same number of curved sections. The ring is situated underground, in a tunnel of 3.8 m inner diameter, at an average depth of 100 m. Electrons and positrons are constrained in a vacuum chamber along the nominal orbit by an electro-magnetic guide field system. The system consists of dipole, quadrupole and sextuple magnets, dipole correctors in horizontal and vertical directions, rotated quadrupoles, and electrostatic deflectors. The quadrupoles produce alternating-gradient forcussing, and the sextupoles are used to compensate the energy dependence of the focusing strength.

The curved sections are occupied by sets of standard cells consisting of these magnets. The beams are bent by the dipole field of about 0.1 T, which is unusually low as a circular accelerator in order to reduce the radiative energy loss. The middle of the eight straight sections are the interaction points. Four of them are surrounded by solenoidal magnets used by the detectors of the experiments. Beams are focussed tightly at the interaction points by the strong quadrupole field generated by a set of superconducting magnets to obtain maximum luminosity. Typical transverse dimension of the beam at an interaction point is about 10 μm $\times$ 250 μm in the vertical and horizontal plane respectively. The longitudinal dimension is typically $\sim$ 2 cm.

3.1.2 Accelerating System

The LEP storage ring is the last one in a chain of five accelerators. Electrons are generated at the end point of the 200 MeV linac and are accelerated by the electrostatic field. Positrons are generated by the positron converter which converts some of the accelerated electrons into positrons. The electrons and positrons are then accelerated up to 600 MeV by a linac. Accelerated particles are injected into the Electron-Positron Accumulating ring (EPA). The role of this ring is to generate bunches of the electrons and positrons with a high intensity and a constant energy. The high intense beams are transferred to the CERN Proton Synchrotron (CERN-PS) which operates as a 3.5 GeV synchrotron. The PS injects into the next circular accelerator, Super Proton Synchrotron (CERN-SPS), operating as a electron-positron injector for LEP. Particles are further accelerated up to 20 GeV in this ring and finally they are transferred to the LEP ring. After the transfer, the LEP accelerating system accelerates the bunches up to the full energy required for collisions.

Since the particles are constrained to a circular motion, they continually lose energy through the emission of synchrotron radiation. In a circular orbit, the energy radiated by an electron or positron per turn is given by

$$\Delta E = \frac{4\pi}{3}\frac{e^2\beta^2\gamma^4}{\rho} \propto \frac{E^4}{\rho}$$

where ρ is the bending radius, β is the particle velocity, γ = (1 - β^2)$^{-1/2}$, and E is the particle energy. Consequently, larger radius results in smaller loss of the energy in addition to lower magnetic field to bent the beams. In order to compensates this energy loss and maintains the beams in their orbit, the Radio-Frequency (RF) accelerator cavities are installed in the straight section of the LEP ring. In LEP2, RF cavities made of superconducting material are employed to reduce the power dissipation as heat in the cavities and to achieve the higher beam energy.

LEP status in 2000

Various techniques to increase the beam energy and the integrated luminosity with respect to those in 1999 were utilized very successfully in 2000 [12]. Mini-Ramp is one of the skills in order to achieve a high energy beam.
While, in 1999, the beam energy was kept constant in each fill, it was proven during the last running day that the mini-ramp technique could be used to increases the beam energy within a fill, in a short time and with no additional background in the detectors. This technique, already proposed in 1999 to optimize the 2000 performance, has several advantages.

- it allows the limit on the total current, which becomes more and more stringent when the energy in crease. A beam energy increase successively during physics;
- it allows the highest energy (with no RF margin) to be reached at end-of-fills while suppressing the burden of one hour re-fillings every 15 minutes, thus saving about two weeks of running;
- it may relax the requirement on the starting energy (with respect to a fixed energy running), which in turn would lengthen the coasts, and make the operation less tiring;
- it can also be used at the beginning of fills, before going to the physics energy, so as to adjust the beams with a comfortable RF margin, which in turn should prevent a few fills from being lost immediately.

3.2 The OPAL detector

The OPAL (**O**mni-**P**urpose **A**pparatus for **L**EP) detector [16] is a large, multi-purpose particle detector. The detector is sited on the LEP accelerator at CERN, and measures the results of interactions between electrons and positrons, which collide at the centre of the detector. Overall, the detector is about 12m long, 12m high and 12m wide.

The main features of the OPAL detector are:

- **Central tracker**
  Detecting charged particles in the central region of a solenoidal coil, and measurements of their direction and momentum with their trajectories, and particle identification by their $\mathrm{d}E/\mathrm{d}x$, and reconstruction of primary and secondary vertices near the interaction point.
- **Electro magnetic calorimeter**
  Identification of photons and electrons, and measurement of their energies.
- **Hadron calorimeter**
  Measurement of hadronic energy by the total absorption using the magnet yoke instrumented as a calorimeter.
- **Muon detector**
  Identification of muons by measuring their position and direction within and behind the hadron absorber.
- **Forward detector**
  Measurement of the absolute machine luminosity using Bhabha scattering events in the very forward direction with respect to the beam line.

The general layout of the detector is shown in figure 3.2, indicating the location and relative size of the various components. Figure 3.3 shows cross sections of the detector parallel and perpendicular to the beam axis. The OPAL right-handed coordinate system is defined such that the origin is at the

geometric centre of the jet chamber, the z axis is parallel to, and has positive sense along, the e^- beam direction, r is the coordinate normal to z, θ is the polar angle with respect to the $+z$ direction and ϕ is the azimuthal angle around the z axis. Full details of the OPAL detector can be found in [16] and only a brief introduction is given here.

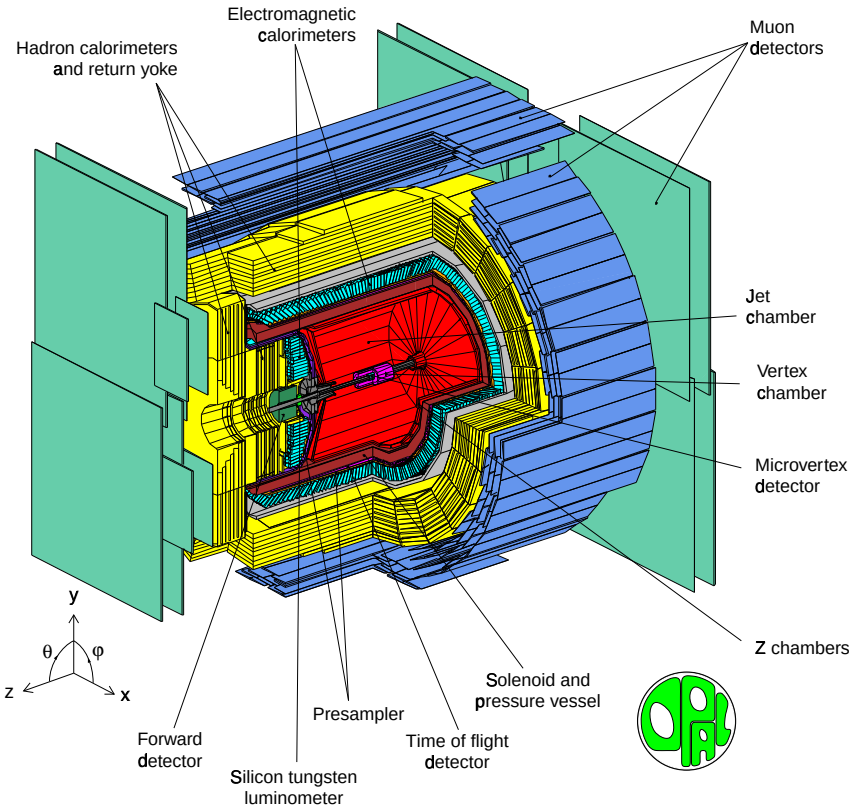

Figure 3.2: *A schematic view of the OPAL detector.*

3.2.1 Magnet

A solenoidal coil surrounds the central detector, and provides a uniform magnetic field parallel to the beam. The coil is made of aluminum supported by itself to reduce the amount of material, which electrons and photons need to pass through before reaching the electromagnetic calorimeter. The thickness of the coil is 96 mm of Al and 54 mm of glass epoxy, which corresponds to 1.7 radiation lengths. The iron return yoke is made of soft iron plates, which serves also as the absorption material of the hadron calorimeter. The magnetic field in the central detector volume is 0.435 T with a uniformity of $\pm$ 0.5 %.

3.2.2 Central Tracking System

The central tracker (CT) consists of a silicon microvertex detector (SI), a vertex chamber (CV), a jet chamber (CJ) and z-chambers (CZ). The whole tracking system is located inside the solenoidal coil.

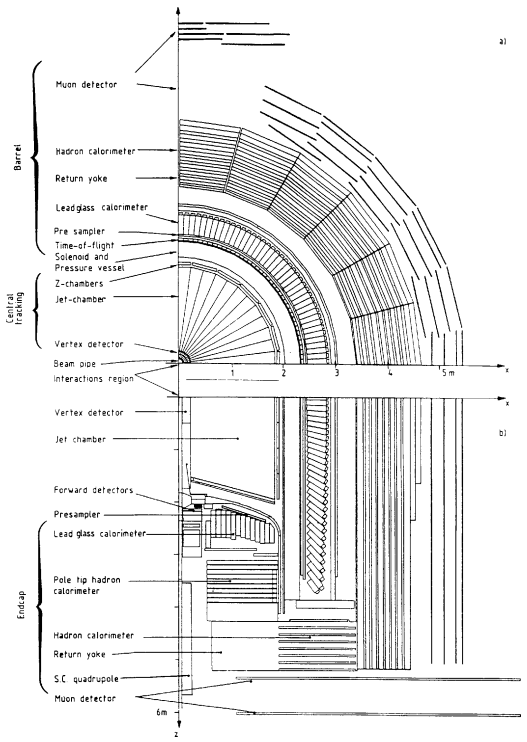

Figure 3.3: *Cross-sectional views of the OPAL detectors (a) perpendicular to the beam and (b) parallel to the beam.*

Central field	0.435 T
Mean coil diameter	4.36 m
Solenoid thickness	96 mm of Al + 54 mm of glass-epoxy ($\sim$ 1.7 X^0, including pressure vessel)
Coil weight	25 t
Overall magnet weight	2800 t

Table 3.1: *Magnetic parameters.*

Silicon Microvertex Detector

The silicon microvertex detector (SI) consists of two barrels of ladders at radii of 6.1 cm and 7.5 cm, respectively. The inner layer consists of 12 ladders and the outer one of 15, tilted to close ϕ gaps as shown in Figure 3.4. Each ladder is 30 cm long and consists of 5 silicon wafers which are assembled by gluing r–ϕ and r–z wafers back to back. The strips run in 25 μm pitch and the signals are read out in 50 μm pitch in r–ϕ and in 100 μm pitch in r-z.

Vertex Drift Chamber

The vertex drift chamber (CV) is a high precision cylindrical jet drift chamber. It is 100 cm long with a radius of 23.5 cm and consists of two layers of 36 ϕ sectors each. The inner layer contains axial sectors, each of which contains a plane of 12 sense wires strung parallel to the beam direction. The outer layer contains stereo sectors each containing a plane of 6 sense wires inclined at a stereo angle of about 4 degree. The r–ϕ position of a track is measured by the drift time sensed by the axial wires and the z position is measured by combining the information from the axial and stereo wires. Figure 3.5 shows

a schematic view of CV and its wire layout at one end plate. Spatial resolution of the r–ϕ position σ is obtained to be about 50 μm.

Jet Chamber

The jet chamber (CJ) is a cylindrical drift chamber of 400 cm long in the z direction with an outer radius of 185 cm and an inner radius of 25 cm. The chamber consists of 24 identical sectors each containing a sense wire plane of 159 wires strung parallel to the beam direction. The signal wires are positioned at radii between 255 mm and 1835 mm with a 10 mm spacing, alternating with potential wires. The signal wires are staggered by $\pm$ 100 μm to resolve left-right ambiguity. The z-coordinate is measured using a charge division technique. The sum of the charges received at both ends of a wire gives information on the energy loss dE/dx. Figure 3.6 shows a plot of dE/dx versus momentum. In the range $|\cos\theta| < 0.73$, 159 points can be measured along each track. More than 20 points on a track can be used for the measurement over 96 % of the full solid angle. Measurements of the curvatures of the tracks provide precise momentum determination. The momentum resolution is given by

$$\frac{\sigma_{P_t}}{P_t} = 1.4 \times 10^{-3} P_t(\mathrm{GeV}) \oplus 0.02$$

including a term due to multiple scattering.

z-Chamber

The z-chambers (CZ) are a set of thin drift chambers which provide the precise measurement of the z-coordinates of tracks as they leave CJ. They consist of a layer of 24 drift chambers with 4 m length and 0.5 m width arranged to form a barrel. The chambers cover 94 % of the azimuthal angle within the polar angle range $|\cos\theta| < 0.72$. Each chamber is divided in the z direction into eight cells, covering 50 cm $\times$ 50 cm, containing a plane of six sense wires strung in the ϕ direction. The θ angle is measured by the drift time and ϕ angle is by the charge division technique. When they are installed in the OPAL detector, θ angle resolution of 3 mrad and ϕ position resolution of about 1.5 cm are obtained.

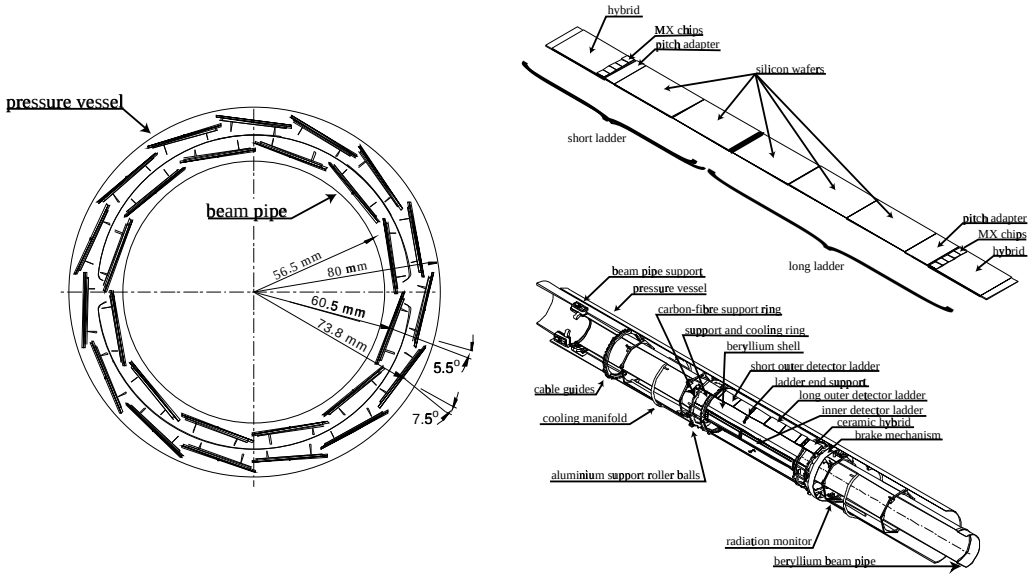

Figure 3.4: *A schematic view of Silicon Micro Vertex detector; (left) cross section view, (right-upper) a set of short and long ladders, (right-lower) Cut away view.*

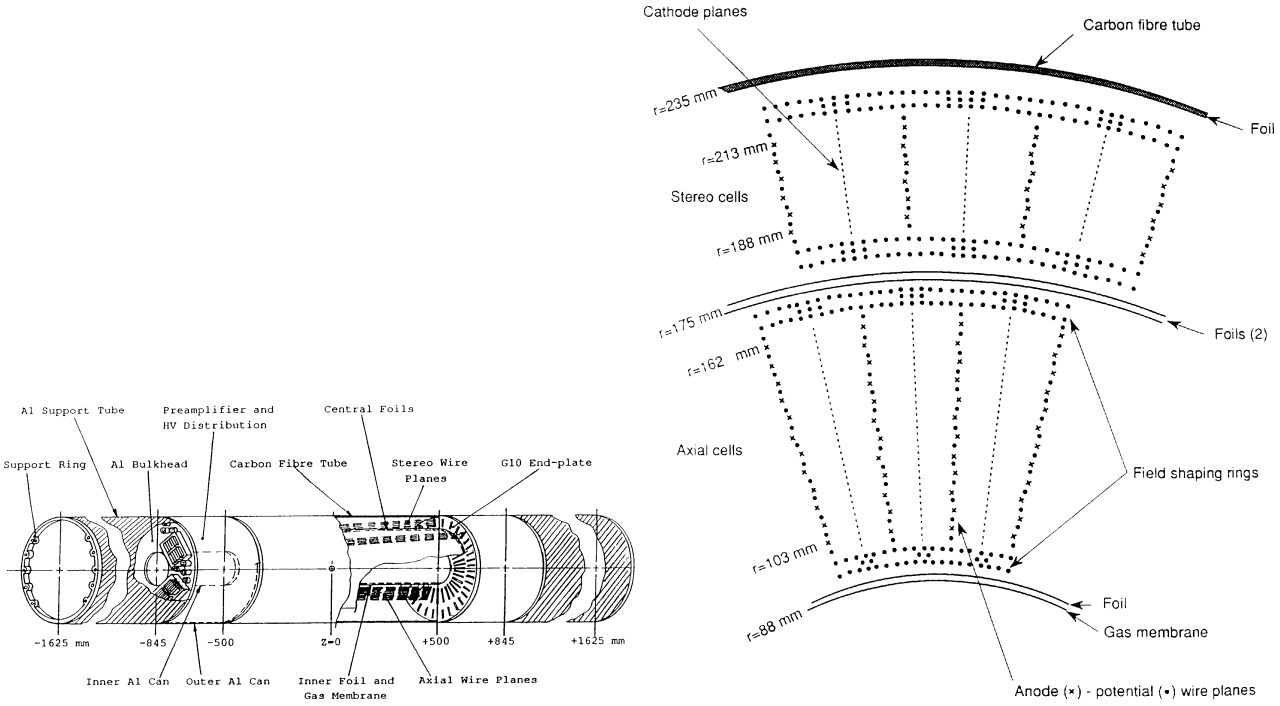

Figure 3.5: *A schematic view of CV (left) and its wire layout at one end plate (right).*

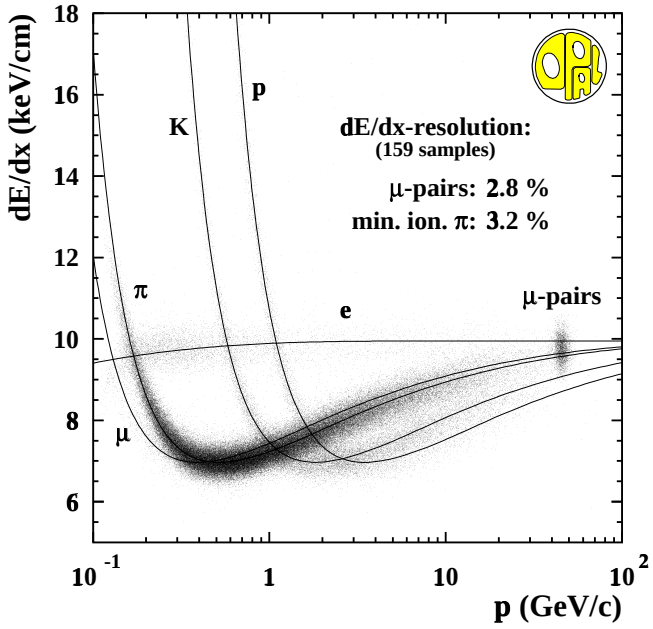

Figure 3.6: *This scatter plot shows the measured dE/dx for multihadronic tracks and muon-pairs together with the expected functional form. The dE/dx resolution for minimum ionizing pions within multihadrons (p = 0.4 - 0.8 GeV/c) and muon-pairs with 159 dE/dx hits is also indicated.*

	Inner	Outer	r–ϕ	r–z
Acceptance	<0.93	<0.90		
Number of ladders	11	64		
Average radius	61 mm	75 mm		
Readout strip pitch			50 μm	100 μm
Spatial resolution			$\sim$5 μm	$\sim$13 μm

Table 3.2: *Characteristics of the Silicon Micro Vertex Detector.*

Tracking device	Vertex detector (CV)	Jet chamber (CJ)	z-chamber
Gas	argon (88.2 %), methane (9.8 %), isobutane (2.0%) at 4 bar		
Maximum drift distance	0.5 μs	5 μs	5 μs
Gas gain	2×10^4	10^4	2–5 $\times 10^4$
Angular coverage	$23^\circ \leq \theta \leq 157^\circ$	$43^\circ \leq \theta \leq 137^\circ$	$44^\circ \leq \theta \leq 136^\circ$
	for axial + stereo wires	for 159 wires	94 % in ϕ
	$18^\circ \leq \theta \leq 162^\circ$	$11^\circ \leq \theta \leq 169^\circ$	67 % in π
	for axial wires	for ≥ 8 wires	
Coordinate determination ϕ	drift time	drift time	charge division
z	ΔT and stereo wires	charge division	drift time
Spatial resolution	55 μm	135 μm	15 mm
Double hit resolution	2.0 mm	2.5 mm	2.5 mm

Table 3.3: *Properties of the tracking chambers.*

3.2.3 Electromagnetic Calorimeter

A lead-glass electromagnetic calorimeter (ECAL) providing acceptance for $|\cos\theta| < 0.984$ together with presamplers and time-of flight scintillators (TOF) is located outside the magnet coil and at the front of both endcaps.

Barrel Electro magnetic Calorimeter

The barrel electromagnetic calorimeter (EB) covers a geometrical region of $|\cos\theta| < 0.82$. Each lead glass block is made of SF57 which has a density of 5.54 g/cm^3. The depth of a block is 37 cm, which corresponds to 24.6 radiation lengths. Figure 3.7 shows the assembly of a block. The calorimeter is segmented into 59 $\times$ 160 blocks in z and ϕ directions, respectively. The blocks are arranged in a nearly-pointing geometry to the interaction region with slight offset in order to prevent incoming particles from escaping in the gaps between the blocks.

The energy resolution during 1999 and 2000 runs is expressed as

$$\frac{\sigma_E}{E} = \frac{12\%}{\sqrt{E}} \oplus 0.7\% \,. \tag{3.1}$$

For 50 GeV electrons injected normal to the counters, a positron resolution was obtained to be 2.4 mm in a test beam.

Endcap Electromagnetic Calorimeter

The endcap electromagnetic calorimeter (EE) covers a region of $0.81 < |\cos\theta| < 0.98$. The blocks are 38, 42 and 52 cm long, and they are arranged so that the total depth of the counter seen by particles from the interaction region is at least 20.5 and typically 22 radiation lengths. They are mounted with

their axes parallel to the beam direction. The lead glass used is CERN-25 which has a density of 4.06 g/cm^3. A total of 1132 lead glass counters are arranged in a dome-shape array as shown in Figure 3.8.

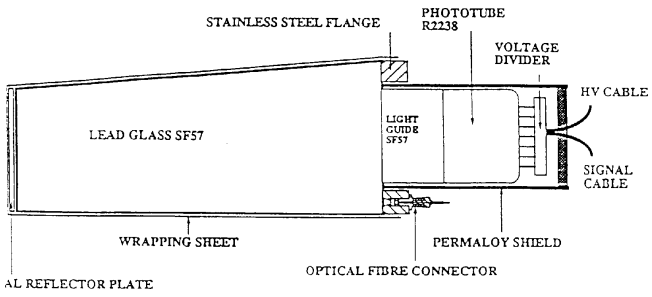

Figure 3.7: *A schematic view of a block in the barrel electromagnetic calorimeter.*

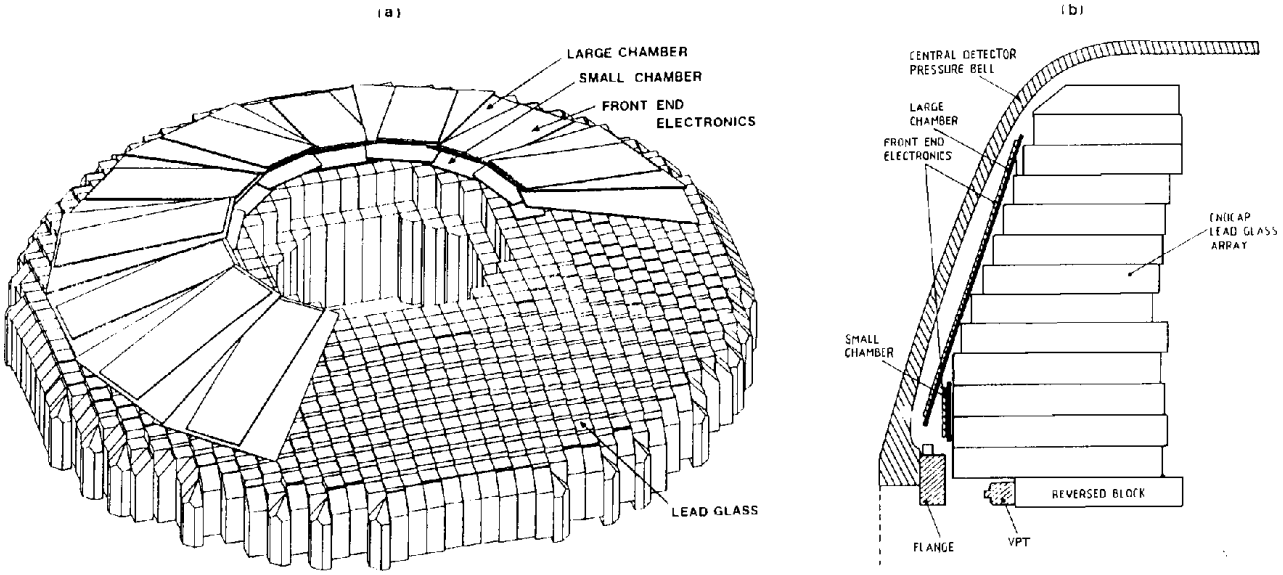

Figure 3.8: *A schematic view of the endcap electromagnetic calorimeter.*

3.2.4 Hadron Calorimeter

The magnet return yoke is instrumented for hadron calorimetry (HCAL) giving a polar angle coverage of $|\cos\theta| < 0.99$. HCAL consists of three parts, barrel, endcap and pole tip hadron calorimeters. Two of them have essentially the same design, located each in the barrel and endcap regions respectively. The energy resolution is $120\ \%/\sqrt{E}$ for all.

Barrel and Endcap Hadron Calorimeter

In the barrel region $|\cos\theta| < 0.81$ the calorimeter consists of 9 layers of chambers with streamer tubes alternating with 8 irons slabs of 100 mm in thickness, which correspond to 4.8 interaction length. The endcap hadron calorimeters cover the ends of the barrels, $0.81 < |\cos\theta| < 0.91$, with 8 layers of chambers and 7 irons slabs of 100 mm in thickness. The total thickness of the iron absorber corresponds to 4.2 interaction lengths. Figure 3.9 shows chamber assemblies of the barrel and endcap hadron calorimeter.

Detector	Barrel	Endcap
Angular coverage, $\lvert\cos\theta\rvert$	< 0.82	0.81 – 0.98
Material	SF57, X^0= 1.50 cm	CEREN 25, X^0= 2.51 cm
Block geometry	Quasi-pointing	Coaxial with beam line
Typical block dimension	$\sim 10 \times 10 \times 37.0$ cm^3	$9.2 \times 9.2 \times 52.0$ cm^3
Depth(for photons from origin)	24.6 X^0	~ 22 X^0
Number of blocks	9,440	2,246
Čerenkov light detector	Field tolerant phototubes	Vacuum photo triodes
Typical magnetic field at detector	0.002 T	0.45 T
Detector gain (PMT or VPT)	$\sim 1.0 \times 10^5$	12.3
Detector high voltage	-1.0 kV	-1.0 kV
Channel equivalent noise	~ 2 MeV	~ 14 MeV
Intrinsic energy resolution (σ_E/E)	0.2 % + 6.3 %/$\sqrt{E}$	~ 5 %/$\sqrt{E}$ at low energy
Intrinsic spatial resolution (at 6 GeV)	~ 11 mm	~ 11 mm

Table 3.4: *Properties of the electromagnetic calorimeter.*

Pole-Tip Hadron Calorimeter

At the end of the endcap hadron calorimeter, the pole tip hadron calorimeter is installed up to the polar angle of $0.91 < \lvert\cos\theta\rvert < 0.99$. It consists of 10 active layers with multiwire proportional chambers alternating with 9 irons slabs of 80 mm in thickness. The total thickness of the iron absorber corresponds to 4.3 interaction lengths.

3.2.5 Muon Detector

The muon detector is located outside of HCAL covering more than 93 % of the full solid angle. Before entering the muon detector, most of hadrons from the interaction region traverse material of more than 7 interaction lengths. Figure 3.10 shows a cross section of a drift chamber of the barrel muon detector. Muons are identified by matching hits in the muon detector and tracks in the central detector to the muon detector within the tolerance caused by energy loss and multiple scattering in the absorber.

3.2.6 Forward Detectors

The forward detectors measure the LEP luminosity by detecting small-angle Bhabha scattering, and also tag electrons from two photon process.

Silicon Tungsten Calorimeter

The silicon tungsten calorimeter (SW) is a sampling calorimeter designed to detect small-angle Bhabha-scattering events in order to measure the luminosity. SW is located at both sides at $\pm$ 238.94 cm from the interaction point on the z-axis and covers the geometrical acceptance of 59 mrad to 24 mrad in polar angle. A schematic view of SW is shown in Figure 3.11. Each calorimeter consists of 19 layers of silicon detectors and 18 layers of tungsten plates. At the front of each calorimeter is a bare layer of silicon to detect preshowers. The next 14 silicon layers are each behind 3.8 mm (1 radiation length) of tungsten and the final 4 layers are behind 7.6 mm (2 radiation length) of tungsten. Each silicon layer consists of 16 wedge shaped silicon detectors. A wedge covers 22.5 degree in ϕ with an inner

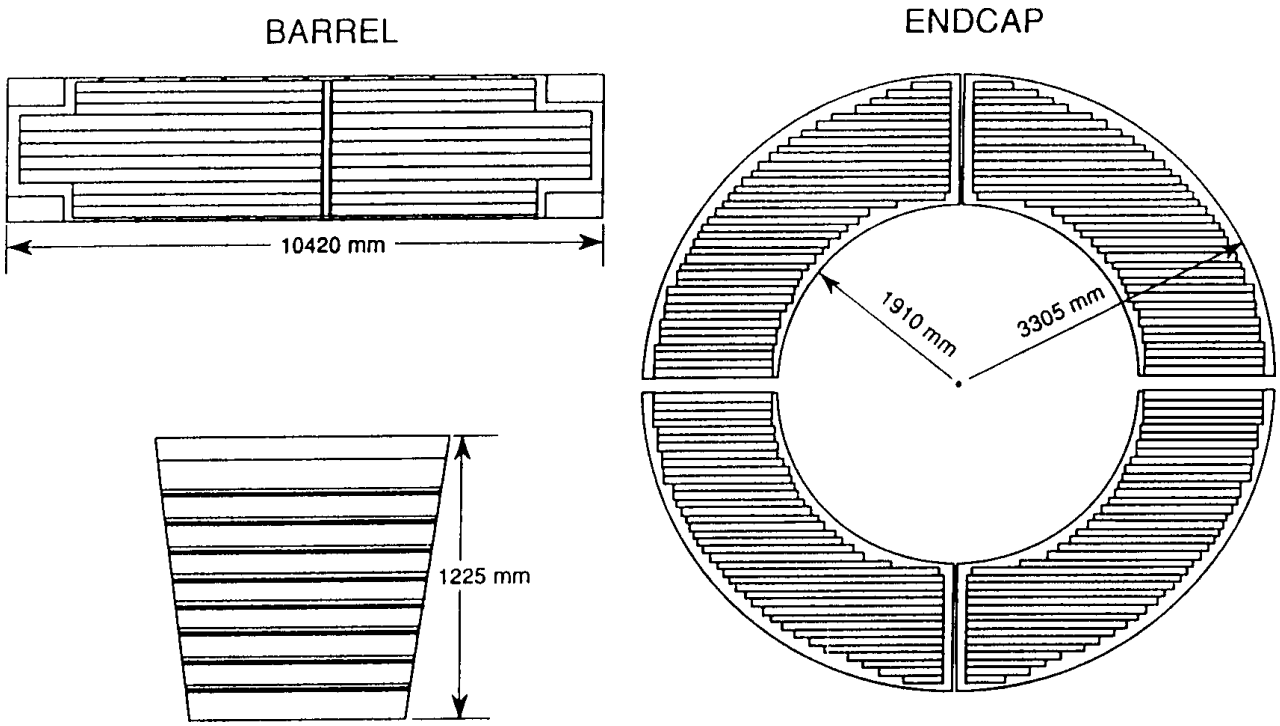

Figure 3.9: *Barrel and endcap chamber assemblies of the hadron calorimeter.*

	Barrel	Endcap	Pole Tip
Angular coverage($\lvert\cos\theta\rvert$)	< 0.81	0.81–0.91	0.91–0.99
Active detector	Limited streamer tubes, cells		Thin high gain multiwire chambers
Number of layers of detector	9	8	10
High voltage	4.65–4.85 kV		3.5 kV
Gas	isobutane (75 %), argon (25 %)		n-pentan (45 %), CO_2 (55 %)
Wire spacing	10 mm		2 mm
Wire diameter	100 μm		50 μm
Readout:towers	pulse height		pulse height
:strips	digital		digital
Absorber (between layers)	100 mm iron		80 mm iron
Gap in iron, for detector	25 mm	35 mm	10 mm
Dimensions : radius	3.4–4.4 m	1.9–3.3 m	0.6–1.8 m
: length	10 m	1.0 m	0.81 m
: thickness of iron	0.8 m	0.7 m	0.72 m
Energy resolution	120 %/$\sqrt{E}$	120 %/$\sqrt{E}$	120 %/$\sqrt{E}$
Strips (10mm)	axial	horizontal	radial
Towers (pointing to vertex)	$\Delta\phi \sim 7.5°$	$\Delta\phi \sim 7.5°$	$\Delta\phi \sim 11°$
	$\Delta\theta \sim 5°$	$\Delta\theta \sim 5°$	$\Delta\theta \sim 4°$

Table 3.5: *Properties of the hadron calorimeter.*

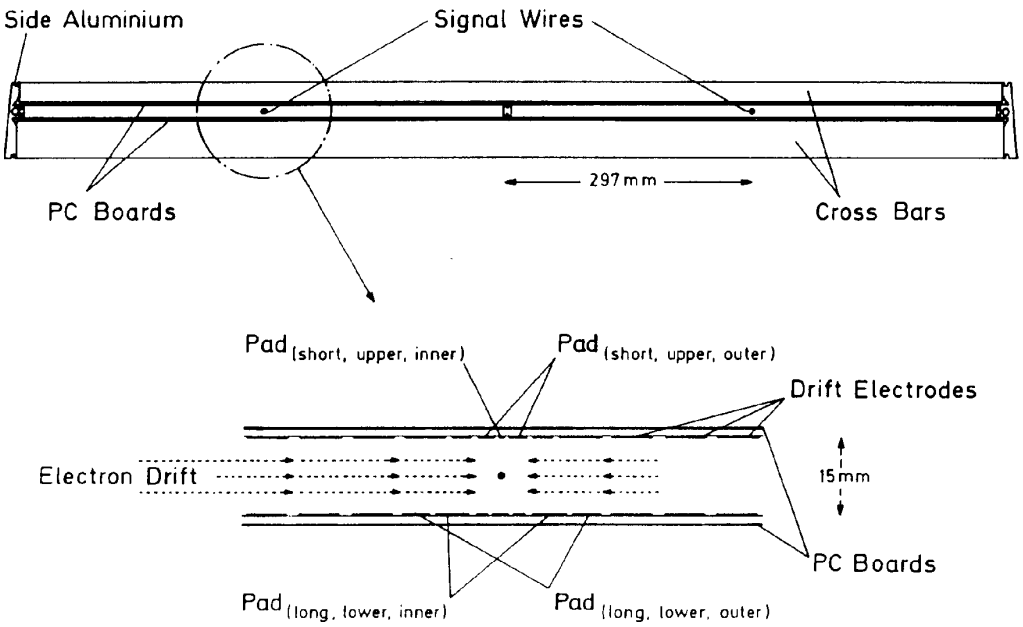

Figure 3.10: *Cross section of a drift chamber of the barrel muon detector.*

	Barrel	Endcap
Angular coverage, $\lvert\cos\theta\rvert$	0.72 for ≥ 1 layer	0.67–0.98
	0.68 for 4 layers	
Absorber (λ_I)	~ 8	8–14
Active detector	110 drift chambers	Limited streamer tubes
Wire direction	along z	along x and y
Wire diameter	50 μm	100 μm
Number of layers	4	4
Spacing	equally spaced over 0.6 m	19, 670, 19 mm
Position Resolution	~ 1.5 mm by drift time (ϕ)	~ 1 mm x (y) by $\perp$ strips
	~ 2 mm by cathode pads (z)	~ 3 mm y (x) by $\parallel$ strips
Direction Resolution	5 mrad	5 mrad
High voltage	drift : 4.0 kV	4.3 kV
	drift + signal: 5.85 kV	
Gas	ethane (10 %), argon (90 %)	isobutane (75 %), argon (25 %)

Table 3.6: *Properties of the muon detector.*

and outer radii of 6.2 cm and 14.2 cm, respectively. The wedge is subdivided into 64 parts (32 in r and 2 in ϕ) giving a total of 38912 channels which are read out individually. Adjacent wedges in a layer are offset by 800 μm in the direction z and positioned in such a way that there is no gap in the active area of the silicon. Consecutive layers in the detector are offset in ϕ by a half wedge so that any cracks between the tungsten half-rings do not line up. The relative experimental error of the absolute luminosity at LEP1 measured with the SW luminometer is 3.3 $\times 10^{-4}$. This includes all intrinsic and time-dependent sources of experimental uncertainty such as detector geometry, gain variations, energy and position biases in the detector response to electromagnetic showers, variations in the beam geometry, backgrounds and other environmental influences.

Forward Calorimeter

The forward calorimeter (FD) consists of 16 segments located at both sides and covers the acceptance of 37 to 154 mrad from the beam pipe. Each segment is composed of 35 sampling layers of lead-scintillator sandwiches divided into a presampler of 4 radiation lengths and the main calorimeter of 20 radiation lengths. It is located behind SW at both sides.

Gamma Catcher

The gamma catcher (GC) is a ring of lead scintillator sandwich sections of 7 radiation lengths, located in front of SW at each side. GC covers the acceptance of 143 to 193 mrad from the beam pipe, thus filling the gap between EE and FD. The detector has a linear response to the energy of electromagnetic shower up to 5 GeV. Any electron or photon with the energy of more than 2 GeV can be detected, thus providing an efficient veto for radiative events.

MIP plug calorimeter

Four layers of 1 cm thick scintillator tiles are installed in both endcaps of the OPAL detector. The main purpose of these tiles is to detect presence of minimum ionizing particles at low angles to the beam axis. Until the installation of the MIP plugs, there were no detectors providing efficient, low angle coverage (between $\sim$ 60 to $\sim$ 160 mrad) for muons. Without the MIP plugs, leptons at low angles can escape detection and fake the missing energy. A schematic view of the layout of SW, FD, GC and MIP plugs are shown Figure 3.12.

3.2.7 Trigger

Events are recorded by the data acquisition system only if they satisfy certain trigger conditions. The detail of the OPAL trigger system can be found in Ref. [16]. The trigger signals from subdetectors divide into two complementary parts, "standard-alone" and "θ–ϕ matrix" signals. Information from a single detector component is used for the stand-alone trigger signals such as total energy measured by ECAL or track multiplicities provided by the track trigger (TT) with relatively high thresholds. In order to allow lower thresholds and spatial coincidences between components, the detector has been subdivided into θ and ϕ elements, "θ–ϕ matrix". The θ–ϕ matrix is composed of overlapping bins in the polar range by 6 bins. The matrix has 5 layers corresponding to the track, time-of-flight, electromagnetic, hadron and muon triggers. The matrix provides spatial correlations of hits within and between subdetector layers.

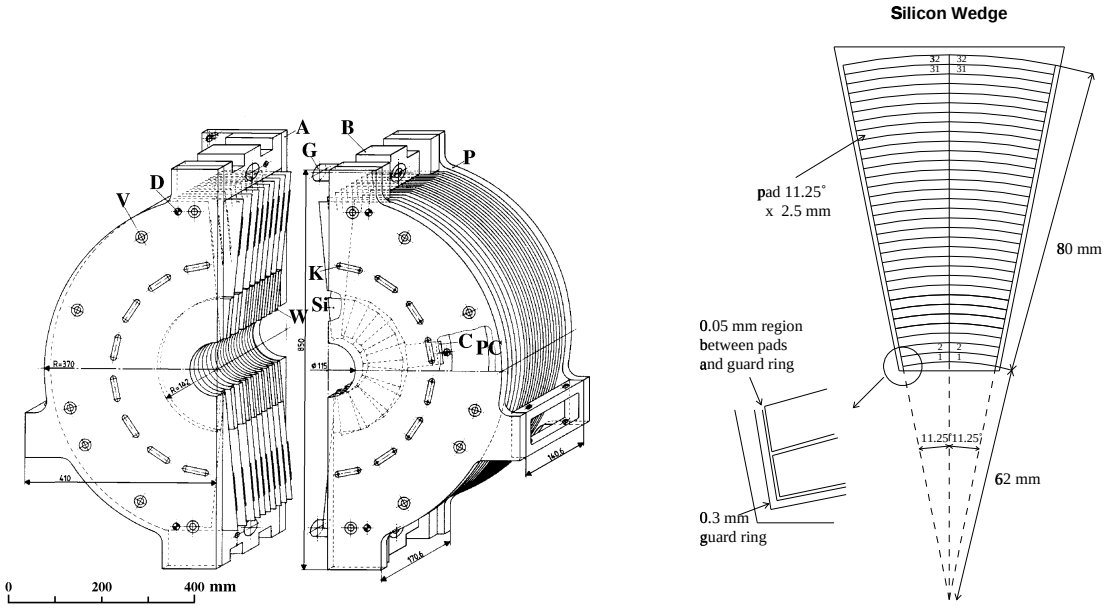

Figure 3.11: *(left) A schematic view of one of the SW calorimeters, separated into two parts, A and B. The dimensions shown on the figure are mm. (right) A schematic illustration of the silicon diode pad geometry.*

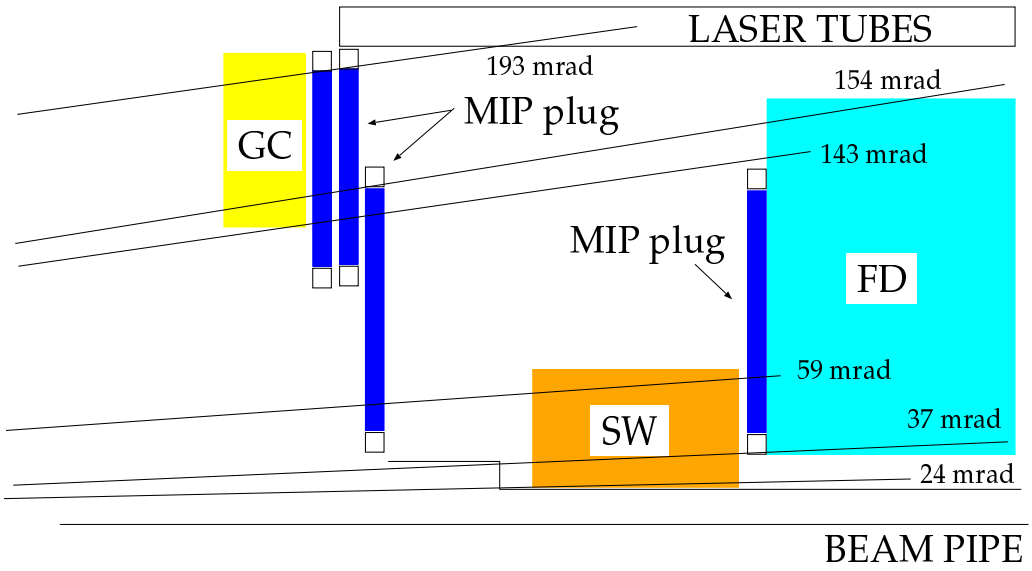

Figure 3.12: *A schematic view of the layout of SW, FD, GC and MIP plugs.*

Chapter 4

Tools for Event Analysis

In this section, a procedure for an event reconstruction , its basic algorithms and the definition of event variables used in the GMSB SUSY particle search are described.

4.1 Event Reconstruction

An event is a collection of *hits*. These hits are reconstructed in order to obtain physics quantities such as track momenta and cluster energies by the event reconstruction program, called ROPE (**R**econstruction of **O**PAL **P**hysics **E**vent). ROPE consists of a variety of *processors*. Some processors convert specific subdetector hits into physics quantities. For example, a processor performs calibration of electromagnetic cluster energy and forms a cluster. Some processors combine data from several subdetectors and compute less detector specific quantities. Finally ROPE forms the OPAL DST (**D**ata **S**ummary **T**ape) containing a set of measured physics quantities, errors of the measurements and so on. ROPE can also read the DST as well as raw data and provide the environment in which more complex analysis can be performed.

4.1.1 Tracks and Calorimeter clusters

First of all, well-measured tracks and calorimeter clusters should be selected to remove the tracks and clusters caused by cosmic rays, beam induced backgrounds, detector noise or bad measurements.

Quality requirements are defined as follows:

- *Good charged tracks* are required to have at least 20 measured space points, more than 50 % of the hits geometrically expected, and transverse momentum exceeding 0.12 GeV. The impact parameters, $|d_0|$ in the r–ϕ plane and $|z_0|$ in the r–z plane, should be less than 2.5 cm and 30 cm, respectively.
- *Good ECAL clusters* in the barrel region are required to have an energy of at least 100 MeV, and the clusters in the endcaps should satisfy the requirement of having an energy of at least 250 MeV and containing at least two adjacent lead glass blocks.
- *Good HCAL clusters* are required to have an energy of at least 0.6 GeV in the barrel and endcaps, and at least 2 GeV in the pole tips.

4.1.2 Energy Flow

An algorithm to calculate energy flow is the most basic method to extract kinematic values of the events. Measuring visible energy with better resolution leads to a more precise measurement of

missing energy, which plays an important role in searches where invisible particles could carry off the energy in the decay of new particles.

In the hadronic final state, charged particles carry about 2/3 of the total energy, while neutral particles carry the remaining 1/3. While neutral particles are measured by the calorimeter only, charged particles deposit energy in ECAL/HCAL and their momenta are measured by CT. This means that simply summing up all the measured momenta by CT and energies by ECAL and HCAL will result in double counting for charged particles. Practically this is avoided by subtracting the assumed charged track energy from the corresponding cluster energy. The remaining energy after subtraction is then considered as originated from neutral particles.

When using calorimetry information, another problem can occur because the energy responses of ECAL and HCAL are very different for hadrons in the OPAL detector. Hadrons may go through ECAL without strong interaction and deposit nearly full energy in HCAL. In some cases, however, hadrons may also deposit a large fraction of its energy in ECAL, as ECAL had non-negligible hadronic interaction length (greater than one). When a hadron shower is produced inside ECAL, Čerenkov light is emitted whose amount corresponds to the energy of π^0 in the shower. Other charged particles in the shower can loose part of their energy by the break up of nuclei and/or nuclear excitation followed by evaporation of nucleons, which is not observed in ECAL. This means that the energy measured by the ECAL is much smaller than the energy lost by the hadron in ECAL. Hence if we simply add the observed energies in ECAL and HCAL for hadrons, we have a bad energy resolution due to the unobserved part of the hadron energy. Therefore, on average, the observed ECAL energy should be scaled up for hadrons. The fraction of the unobserved energy depends on the first interaction points of the hadrons which can not be evaluated cluster by cluster. However it is possible to estimate the mean fraction of the unobserved energy as a function of the observed cluster energy. By adding the ECAL and HCAL energies with optimal weights, we can use the calorimeter energy as the better estimate of the hadron energy as well as the tracking information. This procedure, applied before the above-mentioned subtraction, is very important in order to achieve better resolution. The correction of the measured energy for hadrons is done using the functions shown in Figure 4.1 and the visible energy is reconstructed by the following function;

$$E_{\rm vis} = \sum_i \beta_E(E^i_{\rm raw}) E^i_{\rm raw} + \sum_j \beta_H(H^j_{\rm tower}) H^j_{\rm tower}\,, \tag{4.1}$$

where $E^i_{\rm raw}$ and $H^j_{\rm tower}$ are raw energies (without compensation) of an ECAL cluster i and an HCAL cluster j, respectively. Both $\beta_E(E^i)$ and $\beta_H(H^j)$ are tuned using the pions incident to the calorimeter in the Monte Carlo samples and checked with the data taken at the Z^0 peak. This correction for hadrons should not be applied for electrons and muons. Therefore, a particle identification (ID) is employed in the algorithm. They are summarized briefly in section 4.1.4.

The algorithm starts with finding the matching tracks to ECAL and HCAL clusters, using extrapolated positions of tracks into calorimeters.

Secondly the algorithm uses the particle ID. If the ECAL cluster is identified as that of an electron, the energy is not scaled up. If a track is identified as that of a muon, the expected energy deposit for a minimum ionizing particle is subtracted from the cluster energy.

Next the algorithm searches for ECAL clusters associated with only one or two tracks. If the ratio of the ECAL cluster energy to the track momentum (or momentum sum of two tracks) is greater than 0.7, and the ratio of the associated HCAL cluster energy to the track momentum (or the sum) is less than 0.05, the ECAL energy is reduced by the associated track momentum without compensation optimized for hadrons. This situation will occur when γ is converted before reaching ECAL (as shown in (a) in Figure 4.2) or an isolated pion interacts with lead-glass and larger energy than expected is

observed by ECAL (as shown in (b)). For the latter case, to ensure for any other neutral particle not to have entered the cluster, the requirement on HCAL energy is needed. In the case of γ-conversion, the cluster should be treated as an electromagnetic shower cluster, and in the case of pion interaction the energy should not be calculated with calorimeter but with CT.

Then the algorithm performs "the energy correction for hadrons" to the clusters which are identified as isolated electrons or muons, γ-conversion, or pion interaction. Appropriate energy is subtracted from the ECAL and HCAL clusters according to the associated track momenta. The subtraction is done at first from HCAL cluster energy. If the HCAL cluster energy does not have enough energy, the track momentum is subtracted for the ECAL energy. After subtraction, remaining energy on calorimeters is considered to have come from neutral particles such as γ(s) or neutral hadron(s). The remaining energy in ECAL is re-calculated as originated from γ. Here, charged tracks and neutral clusters are treated complete separately.

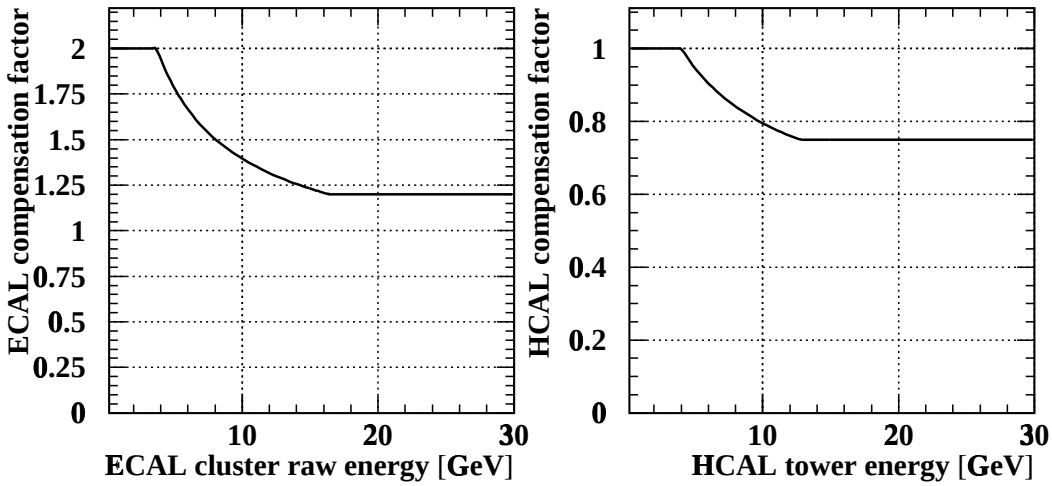

Figure 4.1: *The corrected energies are calculated as (factor)×(ECAL raw energy) and (factor)×(HCAL tower energy).*

4.1.3 Jet Reconstruction Algorithm

Jets are formed from charged tracks and calorimeter clusters using the Durham algorithm. The Durham jet reconstruction algorithm is one of successful combination algorithms which are iterative, beginning with a list of jets that are just the observed particles. At each stage of the iteration, one considers two jets i and j as candidates for combination into a single jet according to the value of a dimensionless variable y_{ij} which expresses "separation" between the jets i and j. The pair i, j with the smallest value of y_{ij} is combined first. When two jets are combined the four-momentum of the new jet P^μ is determined by a combination formula

$$P^\mu = P_i^\mu + P_j^\mu \,. \tag{4.2}$$

After this joining, there is a new list of jets. The process continues until every remaining y_{ij} is lager than a cutoff parameter, y_{cut}, which is called the jet resolution parameter. In this way, each event is classified as containing N jets ($N = 2, 3, 4, ...$), where the number of jets depends on y_{cut}. When events are forced to be reconstructed as N-jet events, this procedure is repeated until the number of jets reached N without setting y_{cut} as a fixed value. There are various algorithms of reconstructing

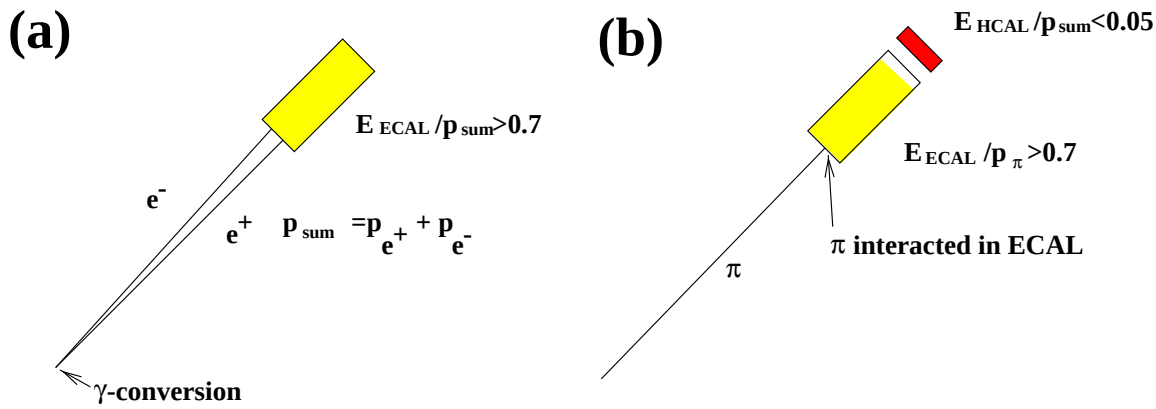

Figure 4.2: *(a): A pair of* e^+e^- *from* γ*-conversion happen to enter a single ECAL cluster. The cluster should be treated as an electromagnetic cluster. (b): When an isolated pion interacts with lead-glass and observed energy with ECAL is larger than 70 % of the track momentum, scaling up the measured ECAL energy will change the event energy flow, which is dangerous especially for low-multiplicity analyses. Such pion energy should be measured by CT and the ECAL cluster should be reduced in the subtraction process. To ensure that no other neutral particle has entered the cluster, it is required that the measured energy in HCAL should be smaller than 5% of the track momentum.*

an event. In the JADE algorithm, y_{ij} is defined as

$$y_{ij} = \frac{2\,E_i \cdot E_j(1-\cos\theta_{ij})}{E^2_{\rm vis}}\,. \tag{4.3}$$

In this method, two soft particles are easy to be combined even if the angle between them is large. Therefore, this analysis employs the Durham algorithm, where y_{ij} is defined as

$$y_{ij} = \frac{(k^2_T)_{ij}}{E^2_{\rm vis}} = \frac{2\,min\,(E_i^2, E_j^2)\,(1-\cos\theta_{ij})}{E^2_{\rm vis}}\,. \tag{4.4}$$

Here $2\,min\,(E_i^2, E_j^2)(1-\cos\theta_{ij})$ is the same as the transverse momentum squared of the lower-energy particle with respect to the direction of the higher-energy particle in the small-angle limit. It can be seen that a particle with low energy will be combined with another soft particle only when the angle between them is smaller than the angle it makes with another particle with higher energy.

4.1.4 Particle Identification

Ways to identify electron, muon, tau lepton and photon used in this analysis are described briefly.

Electron Identification

The electron identification is usually performed using two parameters, i.e. the ionization loss dE/dx and the energy of the electromagnetic cluster (E) divided by the momentum of the track (p) associated with the cluster, the E/p ratio. For electron tracks, dE/dx is expected to be about 10 keV/cm for $p > 2.0$ GeV/c and the E/p ratio is about unity.

Electrons are identified using an *artificial neural network* technique. This neural network consists of an input layer with 12 input nodes, a hidden layer with 15 nodes, and an output layer with an output node. Input parameters for a track are as follows:

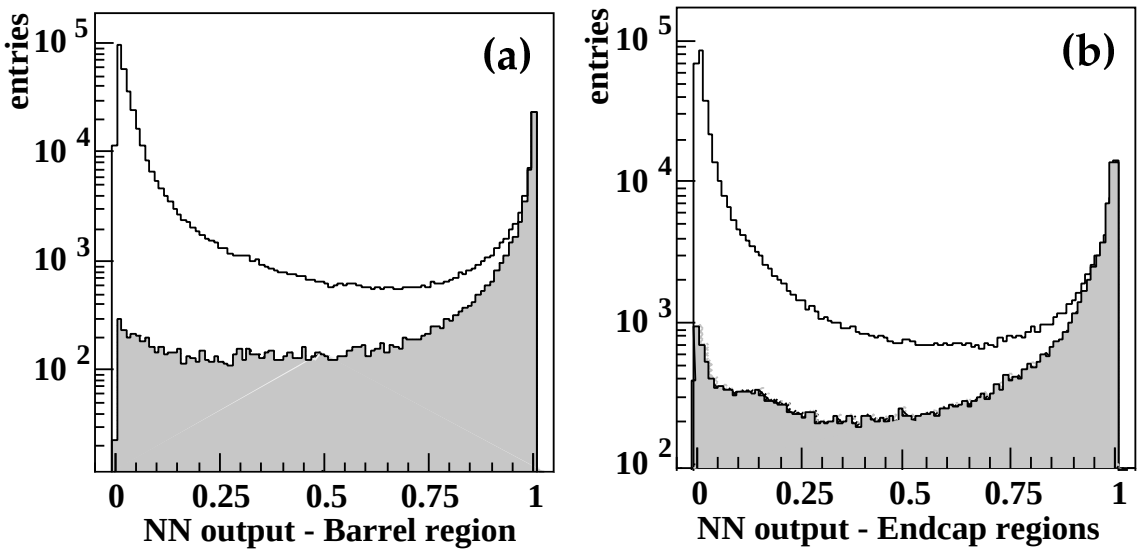

Figure 4.3: *The output distributions of the neural network, (a) for the barrel region and (b) for the endcaps region. The shaded histograms are for true electrons, the open histograms are for backgrounds.*

- the momentum of the track,
- the $\cos\theta$ of the track,
- the dE/dx of the track measured by the jet chamber,
- the expected error of the dE/dx measurement,
- the ratio E/p, where p is the momentum of the track and E is the electromagnetic energy associated to the track,
- the number of lead-glass blocks in the electromagnetic cluster,
- the $E_{\rm cone}/p$, where $E_{\rm cone}$ is the total electromagnetic cluster energy within the cone with a half angle of 30 mrad around the track,
- the number of blocks in the electromagnetic cluster where $E_{\rm cone}$ is defined,
- the ratio $E_{\rm cone}/(E - E_{\rm cone})$,
- the distance between the electromagnetic cluster and the track in ϕ direction,
- the distance between the electromagnetic cluster and the track in θ direction, and
- the multiplicity of presampler hits in front of electromagnetic calorimeters.

The neural network was trained by Monte Carlo samples to output 1 for electron and 0 for other particles. Figure 4.3(a) and (b) show the distribution of the neural network output for the barrel and endcaps, respectively.

Muon Identification

In principle muons have several distinct signatures:

(1) In contrast to any other known charged particles, muons with a momentum of around 2 GeV or more are expected to penetrate the HCAL and leave a track segment in the muon chambers.

(2) Compared to hadrons, muons are expected to deposit a relatively small fraction of their energy in the hadron calorimeter. The hits in the outer hadron calorimeter layers are expected on the way to the muon chambers.

(3) Muons can be distinguished from heavier charged particles (kaons, protons) via the dE/dx measurement in the central tracking detector. However, there is hardly any separation from charged pions only with the dE/dx.

The muon identification is performed again by the artificial neural network technique, which has 18 nodes in one hidden layer. Before applying the neural network, a track is required to have momentum to be larger than 2 GeV, and is "best match" for the given muon segment. The "best match" is based on the matching parameter, $\chi_{\rm pos}$, which is defined as

$$\chi_{\rm pos} = \sqrt{\left(\frac{\Delta\phi}{\sigma_\phi}\right)^2 + \left(\frac{\Delta\theta}{\sigma_\theta}\right)^2}.$$

Here $\Delta\phi$ and $\Delta\theta$ are the differences between the extrapolated track and the muon segment in the ϕ and θ directions respectively, with σ_ϕ and σ_θ being their errors. The output of neural network is shown in Figure 4.4.

The neural network is applied to select tracks with dominant inputs of;

- the $\chi_{\rm pos}$ for the position matching,
- the mis-association ratio $R_{\mu{\rm mis}}$, which is a measure of how ambiguous the choice of the best match is,
- the weight for the match between the muon segment and the track used both positional and directional information for matching inner tracks and muon segments,
- the number of HCAL layers in the HCAL cluster associated with the track if any,
- the number of outermost HCAL layer,
- the weight for the match between the track and HCAL cluster,
- the HCAL cluster energy divided by the track momentum,
- the muon dE/dx weight for the track,
- the error of the dE/dx measurement,
- the momentum of the track,
- the $\cos\theta$ of the track extrapolated to the muon chambers, and
- the ϕ of the track extrapolated to the muon chambers.

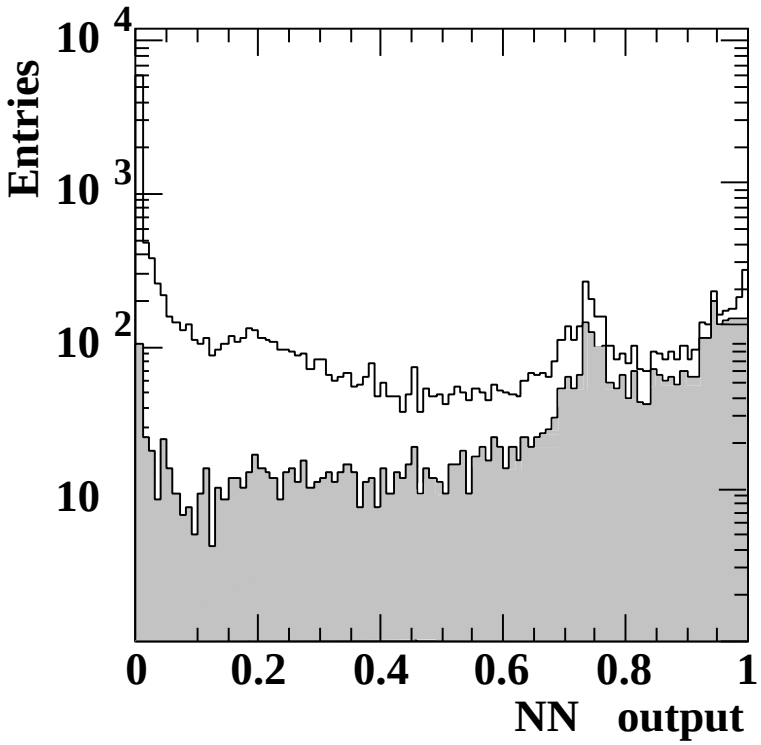

Figure 4.4: *The output distribution of the muon neural network is shown. The Monte Carlo expectation is given by the open histogram, where the the muon component is shown as a shaded histogram.*

Tau lepton Identification

Tau lepton identification is formed to select tau leptons in high multiplicity events. After splitting particles into jets using the Durham algorithm with $k_T^2 = 3\,\mathrm{GeV}^2$, a jet satisfying the following criteria is selected as a tau lepton;

- the number of charged tracks assigned to the jet, $1 \leq N_{\mathrm{ch}} \leq 3$,
- the momentum sum of tracks $> 2\,\mathrm{GeV}$,
- the invariant mass of charged particles assigned to the jet $< 1.5\,\mathrm{GeV}$, and
- the invariant mass of all particles assigned to the jet $< 2\,\mathrm{GeV}$.

If a tau decays leptonically, it may also be selected as electron or muon. Neglecting five- and seven-prong decays of tau, the number of charged tracks assigned to a tau jet should be one or three, and the total charge of tracks must be ± 1. However, these two conditions are not required here. Due to such a loose tau lepton identification, conversion photons (see next paragraph) are often selected as tau lepton. Therefore, tracks identified to originate from a conversion photon are excluded.

Photon Identification

Identification of isolated photons plays an important role in this analysis. It reduces background events very efficiently. Several conditions are required for ECAL clusters to be identified as isolated photons with high purity.

As a photon is neutral and interacts with matter via electromagnetic interaction, it deposits most of energy in ECAL. Ideally, photon is identified as an ECAL cluster with no associated charged track. However due to an amount of material ($\sim 0.1\ X^0$) in front of CJ sensitive volume is located, a photon is converted to an $\mathrm{e}^+\mathrm{e}^-$ pair with an approximately 7 % probability. Such a photon is called *conversion photon*. If one simply requires two photons with no associated charged track in this analysis, ~ 14 % of signals would be lost by this selection criteria. Therefore, conversion photons should be rescued.

A conversion photon is mainly characterized by the existence of an $\mathrm{e}^+\mathrm{e}^-$ pair and the conversion point. The conversion photon identification is performed by an artificial neural network. This neural network consists of an input layer with 9 input nodes, a hidden layer with 10 nodes, and an output layer with one output node. Input parameters are the following;

- the distance between the two tracks at tangency $\Delta(xy)$,
- the radius of the first measured hit of both tracks: R1 and R1P (the P denotes the partner) and the radius of the reconstructed vertex RADV,
- the invariant mass XMI of the $\mathrm{e}^+\mathrm{e}^-$ pair and the impact parameter D0V of the reconstructed photon with respect to the primary vertex of the event,
- the OUT3 of the partner, OUT3 being the neural net output for electron ID described previously, and
- the momentum times the sign of the two tracks, QP and QPP.

To select photons with high purity, isolation requirement is very important, especially in high-multiplicity events. A photon is regarded as isolated if the condition E_{15} <2 GeV is satisfied, where E_{15} is the summation of charged track scalar momenta and electromagnetic calorimeter energies excluding the photon candidate inside a 15° half-angle cone centered on the cluster. If a photon is identified as a conversion photon, energies associated with the photon and energies of associated tracks (*conversion tracks*) are excluded. In this analysis, following selection criteria of isolated photon are employed;

- electromagnetic cluster without associated track or identified as conversion photon ,
- the photon energy, $E_\gamma > 3$ GeV ,
- $|\cos\theta|$ of photon < 0.9, and
- $E_{15}\ (= \sum |P| + E_{\mathrm{ECAL}}) < 2$ GeV .

4.1.5 Event variables

The following event variables are used in the analysis for the SUSY search with GMSB models. They are calculated from good charged tracks and good calorimeter clusters defined in section 4.1.1.

- $N_{\mathrm{ch}}^{\mathrm{good}}$ is the number of good charged tracks.
- N_{conv} is the number of tracks originated from photon conversions. The identification of conversion photon is described in section 4.1.4.
- E_{vis} is defined as the total energy of all reconstructed particles. The energy flow algorithm is used to reconstruct four-momentum of particles.
- $\overrightarrow{P}_{\mathrm{vis}} = (\sum_i p_{x_i}, \sum_i p_{y_i}, \sum_i p_{z_i})$ is defined as the vector sum of all reconstructed particles.

- P_{T} is the transverse component of the total momentum $\overrightarrow{P}_{\mathrm{vis}}$ with respect to the beam axis. Ideally, in the case that no particle escapes the detection, P_{T} is zero. This is one of the most important variables to search for supersymmetric particles. $P_{\mathrm{T}}^{\mathrm{w.o.h}}$ has the same definition as P_{T}, but without the HCAL energy. Because the hadron calorimeter measurement shows a relatively large fluctuation, it can generate a fake transverse momentum. So that P_{T} and $P_{\mathrm{T}}^{\mathrm{w.o.h}}$ are sometimes treated separately for the safety reason.

- The visible mass M_{vis} is defined as the invariant mass of the all reconstructed particles, $M_{\mathrm{vis}} = \sqrt{E_{\mathrm{vis}}^2 - \overrightarrow{P}_{\mathrm{vis}}^2}$.

- $\cos\theta_{\mathrm{miss}}$ is the cosine of the missing momentum $\overrightarrow{P}_{\mathrm{mis}}$ ($= -\overrightarrow{P}_{\mathrm{vis}}$).

- ϕ_{acop} is defined as a supplementary angle in a plane perpendicular to the beam direction between two vectors, $\overrightarrow{P}_1$ and $\overrightarrow{P}_2$, which are made up of vector summations of particle momenta after splitting particles into two jets using the Durham algorithm. The acoplanarity angle is defined as
$$\cos(\pi - \phi_{\mathrm{acop}}) \equiv \frac{(\overrightarrow{P}_1 \times \hat{\mathrm{z}}) \cdot (\overrightarrow{P}_2 \times \hat{\mathrm{z}})}{|\overrightarrow{P}_1 \times \hat{\mathrm{z}}||\overrightarrow{P}_2 \times \hat{\mathrm{z}}|},$$
where $\hat{\mathrm{z}}$ is the unit vector of the e^- beam direction. If any missing particle exists with momentum not pointing to the beam axis, the angle between the two jets in the transverse plane differs from 180°. As a result, a large acoplanarity angle is expected for events with missing particle(s). It is effective to indicate the existence of missing particle(s) even if photons radiated from $e^-(e^+)$ beam or undeflected electrons go undetected and produce large missing energy. It is also helpful to reduce events originating from cosmic rays.

- N_{ℓ}^{iso} is the number of *isolated leptons*. The identified lepton is defined to be isolated if the energy is less than 2 GeV within a cone of half-angle 15° around its lepton.

- $P_{\mathrm{T}\gamma}^{\mathrm{X}}$ is the transverse momentum of photon to the nearest X (a charged track or a jet).

- $M_{\mathrm{jet}}^{\mathrm{max}}$ is the maximum jet mass among N jets when particles are split into N-jets system.

4.2 Monte Carlo Simulation

To search for a new phenomena beyond the Standard Model, event generators both for signal and the Standard Model processes are necessary. A detailed detector simulation is also essential.

4.2.1 Simulation of the GMSB SUSY Processes

DFGT generator

Signal events of charginos, neutralinos and sleptons are generated with the DFGT generator [29]. The DFGT generator includes spin correlations and allows for a proper treatment of both the W boson and the Z^0 boson width effects in the chargino and heavy neutralino decays. The masses and the couplings of the SUSY particles are determined by the four input parameters, m_0 (universal scalar mass at GUT scale), M_2 (the $SU(2)_L$ gaugino mass at GUT scale), μ (the superpotential Higgs mass parameter) and $\tan\beta$ (the ratio of the VEV of the two Higgs doublets). Once the input parameters are given, the DFGT generates four-momenta of particles for a specified SUSY production and decay process.

Events are generated as follows:

- Full helicity amplitudes from initial e^+e^- states into final state partons are first calculated at tree level. This is done using the HELAS library routine [30], which allows us to implement correct angular correlations and effects of the natural width in the structure function formalism.
- The effective cross sections are then evaluated by the numerical integration package BASES [31]. Initial state radiation is included in the structure function.
- The generation of unweighted events is done at the parton level using the SPRING package [31]. The QCD evolution and hadronization of the final state quarks are performed via an interface with JETSET 7.4 [21].

M_2 and μ are adjusted in order to get the NNLSP and NLSP with a mass combination.

The most important parameters influencing the chargino detection efficiency are the mass of the lightest chargino, $m_{\tilde{\chi}_1^+}$, and the mass difference between the lightest chargino and the lightest neutralino, $\Delta M \equiv m_{\tilde{\chi}_1^+} - m_{\tilde{\chi}_1^0}$. The $\tilde{\chi}_1^+\tilde{\chi}_1^-$ events are generated at 72 points of the ($m_{\tilde{\chi}_1^+}$, ΔM) plane; 60 GeV $\sim$ 96–102.5 GeV (a upper value depends on a cms energy) for $m_{\tilde{\chi}_1^+}$, and 3 GeV $\sim m_{\tilde{\chi}_1^+}$ for ΔM. At each point 1,000 events are generated for the decay $\tilde{\chi}_1^+ \rightarrow \tilde{\chi}_1^0\, W^{\pm(*)}$. For the $\tilde{\chi}_1^0\tilde{\chi}_2^0$ production, $m_{\tilde{\chi}_2^0}$ and $\Delta M \equiv m_{\tilde{\chi}_2^0} - m_{\tilde{\chi}_1^0}$ are the main parameters affecting the efficiency. The $\tilde{\chi}_1^0\tilde{\chi}_2^0$ events are generated at 100 points of the ($m_{\tilde{\chi}_1^0} + m_{\tilde{\chi}_2^0}$, ΔM) plane; 100 GeV $\sim$ 190–205 GeV for $m_{\tilde{\chi}_1^0} + m_{\tilde{\chi}_2^0}$, and 3 GeV $\sim$ 180–190 GeV for ΔM. For the $\widetilde{\ell^+}\widetilde{\ell^-}$ pair production, $m_{\widetilde{\ell_1^+}}$ and $\Delta M \equiv m_{\widetilde{\ell_1^+}} - m_{\tilde{\chi}_1^0}$ are the main parameters affecting the efficiency. The $\widetilde{\ell_1^+}\widetilde{\ell_1^-}$ events are generated at 48 points of the ($m_{\widetilde{\ell_1^+}}$, ΔM) plane; 60 GeV $\sim$ 95–102 GeV for $m_{\widetilde{\ell_1^+}}$, and 3 GeV $\sim m_{\widetilde{\ell_1^+}}$ for ΔM. These signal Monte Carlo events are generated at cms energies of 192, 196, 200 and 206 GeV.

4.2.2 Simulation of the Standard Model Processes

The following Standard Model processes are considered as background.

Multihadronic Process

Multihadronic events are generated via the process $e^+e^- \rightarrow Z^{0(*)}/\gamma^* \rightarrow q\bar{q}$. At the cms energy above the Z^0 boson mass, initial state photons are easily radiated to reduce the effective cms energy of the e^+e^- system to the Z^0 pole before the production of multihadronic events. This is called the "radiative-return" process and the cross-section at LEP 2 energies reaches about 100 pb. Generation of these multihadronic events and hadronization of the $q\bar{q}$ system is simulated by using the KK2F [19] and PYTHIA 6.125 [21] packages, respectively. The initial state radiation (ISR) is reproduced with CEEX [20][1] by $\mathcal{O}(\alpha^3 L^3)$ while the final state radiation (FSR) is included in the showering process by PYTHIA.

Lepton pair Processes

For $e^+e^- \rightarrow \mu^+\mu^-(\gamma)$ and $e^+e^- \rightarrow \tau^+\tau^-(\gamma)$ events, lepton pairs are simulated using the KK2F package, in which ISR, FSR and ISR–FSR interference are included. The BHWIDE [24] and TEEGG [25] programs generate $e^+e^- \rightarrow e^+e^-(\gamma)$ events. The former is used for events with both the electron and positron scattering angles larger than 12.5° from the beam axis, and the latter is used for the remaining phase space. Tau lepton decays are simulated by the TAUOLA program [22]. Radiative return tau pair events become the most serious background for the low-multiplicity signal.

[1] Coherent Exclusive Exponentiation (CEEX) is a new theoretical framework for precision predictions of higher order radiative corrections.

Two-photon Processes

Two-photon events are generated through the process $e^+e^- \rightarrow e^+e^- + X$ where the system X is produced in the scattering of two quasi-real photons as $\gamma\gamma \rightarrow X$. Hadronic final states are simulated using PYTHIA and PHOJET at low Q^2 (< 4.5 GeV^2). At high Q^2 the F2GEN with 'perimiss' option [2] is found to give the best description of data. PYTHIA and HERWIG are also used for comparison. The Vermaseren generator is used to simulate purely leptonic final states in two-photon processes. Additional samples which are not covered by the Vermaseren program are generated using the grc4f package [26].

Four-fermion Processes

Four-fermion events are dominated by the W^+W^-pair production processes. Other contributions are from $Z^0\gamma^*$ and $Z^0Z^{0(*)}$ events. They are simulated using the grc4f and KORALW [27]. Processes $e^+e^- f\bar{f}$ ($f = e, \mu, \tau, q$) are generated by grc4f and the others are generated by KORALW. The events with an energetic neutrino and ISR/FSR are serious background in this analysis. These events are simulated by KORALW, where ISR is treated with up to precision of $\mathcal{O}(\alpha^3)$. For FSR, JETSET showering algorithm and PHOTOS are used for multihadonic and leptonic final states, respectively.

4.2.3 Detector Simulation

GOPAL [17] is a Monte Carlo program to simulate the OPAL detector using the CERN GEANT3 package 1.1 [18]. GEANT provides tools to define the geometrical parameters of a detector using standard shapes. GEANT also deals with tracking of particles through this detector, including the necessary physics processes (scattering, decays, interactions). In order to use GEANT a number of user routines have to be provided. These fall broadly into four categories:

(1) At initialization time one has to set up the geometrical description of the detector, and define the materials and tracking parameters for each volume.

(2) Generation of the primary kinematics for each event.

(3) At each step of each particle the user is given control. For particles traversing sensitive detectors one can store *hits*, which contain the necessary information to allow the subsequent simulation of the detector response. In addition, one can decide whether to stop the tracking of certain particles.

(4) At the end of each event one enters the digitization stage, where the hits are used to simulate the data which the detector would have produced for subsequent reconstruction or analysis.

The output from GOPAL is passed to the OPAL reconstruction program, ROPE, as if they were real data.

[2] In the perimiss model, an angular distribution of virtual photons is determined by x (a fraction of a virtual photon energy to a $e^{\pm}$ beam energy) and Q_2 (a momentum transfer of a virtual photon) of generated events.

Chapter 5

Search for SUSY events with Isolated Photons

5.1 Data samples

Data samples used for the physics analysis consist of events satisfying the requirements that ensure the full detector functionality without hardware or data acquisition problems. This selection is made on the basis of a classification of data performed by a team of experts using the database of hardware problems compiled during the data taking as well as the output of appropriate monitoring programs, checking inconsistencies and defects of the data. The criteria that have to be satisfied by the event to be accepted are the following:

(1) CJ is fully operational to avoid poor tracking performances,

(2) EB and EE are fully operational for the the energy measurement to be reliable, especially for photons,

(3) SW and FD are operational for reliable luminosity monitoring.

The available data samples in 1999 and 2000 are summarized in Figure 5.1.

Ideally speaking each data sample at each cms energy would require a dedicated optimized selection. This is clearly unpractical since it would imply that huge Monte Carlo productions of background samples and signal samples are necessary. Moreover it is evident that no large changes are expected for a few GeV of energy increment either in the signal and the background shapes. Therefore, Monte Carlo samples are produced only at cms energies of 192, 196, 200, 202 and 206 GeV. Some of event variables are normalized by cms energy in order to reduce a cms energy dependence.

5.2 Luminosity

The luminosity is measured using small-angle Bhabha events detected in the SW calorimeters. Bhabha scattering events are selected by requiring a high energy cluster in each end of SW, as described below. The energy in each calorimeter has to be at least half of the beam energy, and the average energy has to be at least three quarters of the beam energy. Figure 5.2 shows the correlation of the energy of the SW calorimeter on one end with that on the other end. The two highest energy clusters are required to be back-to-back in ϕ, $||\phi_R - \phi_L| - \pi| < 200$ mrad, where ϕ_R and ϕ_L are the azimuthal angles of the clusters in the right- and left-hand calorimeters, respectively. They are also required to be collinear by placing a cut on the difference between the radial position, $\Delta R \equiv |R_R - R_L| < 25$ mm, where R_R and R_L are the radial coordinates of the clusters on a plane approximately 7 radiation

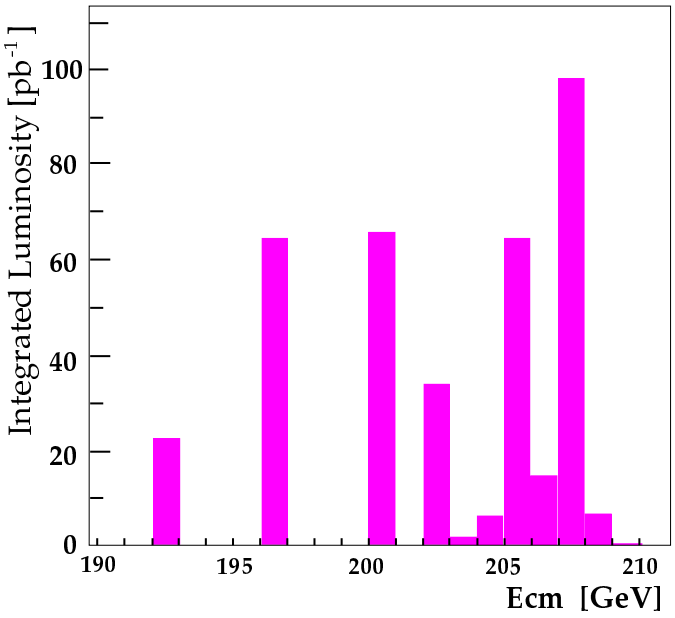

cms energy [GeV]	Luminosity [pb^{-1}]
192	26.3
196	72.7
200	75.3
202	38.3
203	1.5
204	7.0
205	73.6
206	17.0
207	112.1
208	8.1
209	0.1
Total	432.0

Figure 5.1: *Luminosities at each cms energy during 1999 and 2000 data taking. The total luminosity is 432 pb^{-1}.*

lengths into the calorimeter. This cut corresponds to an acollinearity angle[1] of about 10.4 mrad. The inner and outer radial cuts on the fiducial region delimit a region between 38 and 52 mrad on one side of the calorimeter, which for the opposite calorimeter a wider zone between 34 and 56 mrad is used. Two luminosity measurements are performed; the narrower fiducial region on one side plus the wider region on the other side and vice versa. The final result is the average of the two and has no first-order dependence on beam offsets or tilts. The cross-section of Bhabha scattering accepted by these cuts is calculated using the Monte Carlo program BHLUMI [32]. The statistical error on the luminosity measurement is 0.26 %. The systematic uncertainty which arises from theoretical knowledge of the cross-section and detector effects amounts in total to 0.30 (0.22) % in 2000 (1999). The method of the luminosity measurement is fully described in [33].

5.3 Preselection

To select well-measured events and reduce huge uninteresting events, the following preselection is applied:

- The number of good charged tracks in an event, $N_{\rm ch}^{\rm good} > 2$. In addition, the ratio of the number $N_{\rm ch}^{\rm good}$ to the total number of reconstructed tracks is required to be larger than 0.2.
- The transverse momentum of the event, $P_{\rm T} > 0.02\sqrt{s}$.
- The visible mass reconstructed from all particles in the event, $M_{\rm vis} > 3$ GeV .
- The total energies deposited in each side of the silicon tungsten calorimeter, the forward calorimeter and the gamma-catcher at each side have to be smaller than 2 GeV, 2 GeV, and 5 GeV, respectively.

[1] An acollinearity angle is a supplementary angle between two vectors.

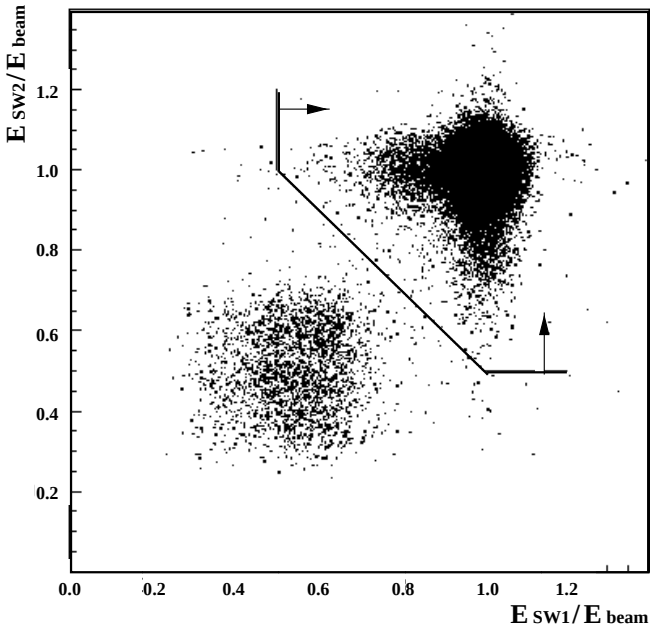

Figure 5.2: *The correlation of the energy (shown as the fraction of the beam energy) of the SW calorimeter on one end of OPAL with that the SW calorimeter on the other end. The Bhabha peak is clearly separated from the off-momentum background.*

- The maximum EM cluster energy and the maximum charged track momentum have to be smaller than 1.3 times of the beam energy.
- the ratio of the visible energy measured in the forward region ($|\cos\theta| > 0.9$) to the total visible energy is less than 0.2 .

5.4 Event Classification

The three signal processes, slepton, neutralino, and chargino productions can have similar final states, namely events with "*photons plus X (jets and/or leptons) with missing energy*". There are six different processes;

(1) $\widetilde{\ell}^+\widetilde{\ell}^-$ with $\widetilde{\ell}^+ \to \ell^+\widetilde{\chi}^0_1$

(2) $\widetilde{\chi}^0_1\widetilde{\chi}^0_2$ with $\widetilde{\chi}^0_2 \to \widetilde{\chi}^0_1 \mathrm{Z}^{0(*)}$ followed by $\mathrm{Z}^{0(*)} \to \ell^+\ell^-$,

(3) $\widetilde{\chi}^0_1\widetilde{\chi}^0_2$ with $\widetilde{\chi}^0_2 \to \widetilde{\chi}^0_1 \mathrm{Z}^{0(*)}$ followed by $\mathrm{Z}^{0(*)} \to \mathrm{q\bar{q}}$,

(4) $\widetilde{\chi}^+_1\widetilde{\chi}^-_1$ with $\widetilde{\chi}^\pm_1 \to \widetilde{\chi}^0_1 \mathrm{W}^{\pm(*)}$ followed by both $\mathrm{W}'s \to \ell\nu$,

(5) $\widetilde{\chi}^+_1\widetilde{\chi}^-_1$ with $\widetilde{\chi}^\pm_1 \to \widetilde{\chi}^0_1 \mathrm{W}^{\pm(*)}$ followed by one $\mathrm{W} \to \mathrm{q\bar{q}}'$ and the other $\mathrm{W} \to \ell\nu$, and

(6) $\widetilde{\chi}^+_1\widetilde{\chi}^-_1$ with $\widetilde{\chi}^\pm_1 \to \widetilde{\chi}^0_1 \mathrm{W}^{\pm(*)}$ followed by both $\mathrm{W}'s \to \mathrm{q\bar{q}}'$.

Here, all decay chains terminate with the decay $\widetilde{\chi}^0_1 \to \gamma\widetilde{\mathrm{G}}$.
These final states can be classified into three topologies.

(A) photons plus leptons with missing energy	(1),(2),(4)
(B) photons plus jets with missing energy	(3),(6)
(C) photons plus jets plus lepton with missing energy	(5)

It is effective to optimize the selection not for each process but for each topology. The most characteristic variables of event topologies are *multiplicity* and ΔM. The multiplicity is defined as $N_{\rm ch}^{\rm good} - N_{\rm conv}$. Events with $N_{\rm ch}^{\rm good} - N_{\rm conv} \leq 6$ (low-multiplicity) are categorized in (A), and the others (high-multiplicity) are classified into (B) or (C). The ΔM is the mass difference between the NNLSP ($\widetilde{\chi}_1^{\pm}, \widetilde{\chi}_2^0, \widetilde{\ell}_1^{\pm}$) and NLSP ($\widetilde{\chi}_1^0$) masses, which characterizes the photon energy and the missing energy.

Category (A) includes signal events with two leptons in addition to photons. Only one analysis is employed for this topology because it is not very necessary to change the analysis according to ΔM. Events with photons plus jets with missing energy are classified to Category (B). A total of five different analyses are employed since it is difficult to keep a high sensitivity using only one analysis. The analysis is divided into three according to the size of ΔM, and they are called "*small*", "*medium*" and "*large*". For signals with medium and large ΔM, the analysis is divided into two; one is for 4-jet events expected for $\widetilde{\chi}_1^+\widetilde{\chi}_1^-$ and the other is for 2-jet events expected for $\widetilde{\chi}_1^0\widetilde{\chi}_2^0$. Category (B) is summarized in Table 5.1. An event which has one isolated lepton as well as photons plus jets with missing energy is classified to Category (C). When one W decays into $\ell\nu$ and the other W decays into $\mathrm{q\bar{q}}$, an event should be categorized here. Two analyses, Analyses C1 and C2, are employed for signals with medium ΔM and large ΔM, respectively. The case of small ΔM is covered by Analysis B1 because the lepton is not well identified.

Selection	target process	ΔM
B1	$\widetilde{\chi}_1^0\widetilde{\chi}_2^0$ and $\widetilde{\chi}_1^+\widetilde{\chi}_1^-$	small
B2N	$\widetilde{\chi}_1^0\widetilde{\chi}_2^0$	medium
B2C	$\widetilde{\chi}_1^+\widetilde{\chi}_1^-$	medium
B3N	$\widetilde{\chi}_1^0\widetilde{\chi}_2^0$	large
B3C	$\widetilde{\chi}_1^+\widetilde{\chi}_1^-$	large

Table 5.1: *Categorization in analysis B.*

5.5 Event selections

Each analysis is presented in the following subsections. All analyses are applied to the data collected in 1999 and 2000 at $\sqrt{s}$ = 192–209 GeV. Experimental plots are shown for the data collected in 2000 with an average energy of 206.1 GeV and Monte Carlo samples generated at $\sqrt{s}$ = 206 GeV.

5.5.1 Analysis A

Analysis A is employed for the topology of "*photons plus leptons with missing energy*", which is expected by the following production and decay processes;

$$\begin{aligned}
\widetilde{\ell}_1^+\widetilde{\ell}_1^- &\rightarrow \widetilde{\chi}_1^0\widetilde{\chi}_1^0\ell^+\ell^- \rightarrow \gamma\widetilde{G}\gamma\widetilde{G} + \ell^+\ell^- \,, \\
\widetilde{\chi}_1^0\widetilde{\chi}_2^0 &\rightarrow \widetilde{\chi}_1^0\widetilde{\chi}_1^0\mathrm{Z}^0 \rightarrow \gamma\widetilde{G}\gamma\widetilde{G} + \ell^+\ell^- \,, \\
\widetilde{\chi}_1^+\widetilde{\chi}_1^- &\rightarrow \widetilde{\chi}_1^0\widetilde{\chi}_1^0\mathrm{W}^+\mathrm{W}^- \rightarrow \gamma\widetilde{G}\gamma\widetilde{G} + \ell^+\nu_\ell\ell^-\bar{\nu}_\ell \,.
\end{aligned}$$

(A - 0) Events must satisfy the following set of selection criterion to be selected as candidates.

- $|\cos\theta_{\rm miss}| < 0.95$,
- $P_{\rm T}, P_{\rm T}^{\rm w.o.h} > 0.03\sqrt{s}$,
- $0.25\sqrt{s} < E_{\rm vis} < 0.85\sqrt{s}$,

- $\phi_{\rm acop} > 5^\circ$, and
- $N_\gamma \geq 2$.

Here, N_γ is the number of an isolated photons. The criteria of an isolated photon is described in section 4.1.4. Figures 5.3–5.5 show distributions of $P_{\rm T}$, $E_{\rm vis}$ and $\phi_{\rm acop}$ for real data and background Monte Carlo as well as expected stau signal Monte Carlo for $\Delta M = 3, 20$ and $M_{\tilde{\tau}^+}$ GeV. The plots of signal Monte Carlo events are shown with arbitrary normalization. These basic cuts reduce most of backgrounds from two-photon and two-fermion processes. The energy distribution of the most energetic photon (hereafter referred as the first photon), $E_\gamma^{\rm 1st}$ is shown Figure 5.6. Background dominantly comes from radiative-return tau pair events. A candidate event must finally satisfy the following cuts.

(A - 1) The photon energies are required to be;

- $10 < E_\gamma^{\rm 1st} < 90$ GeV for the 1st photon , and
- $E_\gamma^{\rm 2nd} > 5$ GeV for the 2nd photon .

Most of radiative-return events are suppressed by the requirement on $E_\gamma^{\rm 2nd}$.

(A - 2) Most of ISR photons are reduced by the requirement of $|\cos\theta_\gamma| < 0.9$. A final state radiation (FSR) and a neutral hadron have a possibility to fake high energy photons from the $\tilde{\chi}_1^0$ decays. FSR tends to distribute closely around a charged track and a neutral hadron usually a small transverse momentum with respect to a hadronic jet. Therefore, these backgrounds can be reduced by requiring that each photon has a large transverse momentum with respect to the nearest charged track, $P_{\rm T\gamma}^{\rm track}$;

- $P_{\rm T\gamma}^{\rm track} > 10$ GeV for the 1st photon, and
- $P_{\rm T\gamma}^{\rm track} > 5$ GeV for the 2nd photon.

Figure 5.7 shows a two-dimensional distribution of the $P_{\rm T\gamma}^{\rm track}$ values of the first and the second photons.

5.5.2 Analysis B1

The selection B1 works for the neutralino and chargino detection with small ΔM;

$$\begin{aligned} \tilde{\chi}_1^0\tilde{\chi}_2^0 &\rightarrow \tilde{\chi}_1^0\tilde{\chi}_1^0{\rm Z}^{0*} \rightarrow \gamma\tilde{G}\gamma\tilde{G} + q\bar{q}\,, \\ \tilde{\chi}_1^+\tilde{\chi}_1^- &\rightarrow \tilde{\chi}_1^0\tilde{\chi}_1^0{\rm W}^{+*}{\rm W}^{-*} \rightarrow \gamma\tilde{G}\gamma\tilde{G} + q\bar{q}q\bar{q}\,(q\bar{q}\ell\bar{\nu}_\ell)\,. \end{aligned}$$

In the case of small ΔM, the event multiplicity becomes low due to small phase space for the $\rm W^\pm$ and $\rm Z^0$ bosons. As a consequence, most of signal events with small ΔM are categorized into Category A: the fractions of events in Category (B) are < 4 %, 3–19 % and 20–40 % for signal with ΔM = 3 GeV, 5 GeV and 10 GeV, respectively. Actually, the number of events categorized to this analysis is small, but they can be evident signal events with high energetic photons. As far as ΔM is small, the analysis is not divided according to the presence of an isolated lepton. This is because the lepton from $\rm W^\pm$ decay which follows $\tilde{\chi}_1^\pm \rightarrow \tilde{\chi}_1^0{\rm W}^\pm$ is often not identified as isolated lepton due to the small energy.

(B1 - 0) Events must satisfy the following criteria:

- $|\cos\theta_{\rm miss}| < 0.95$,

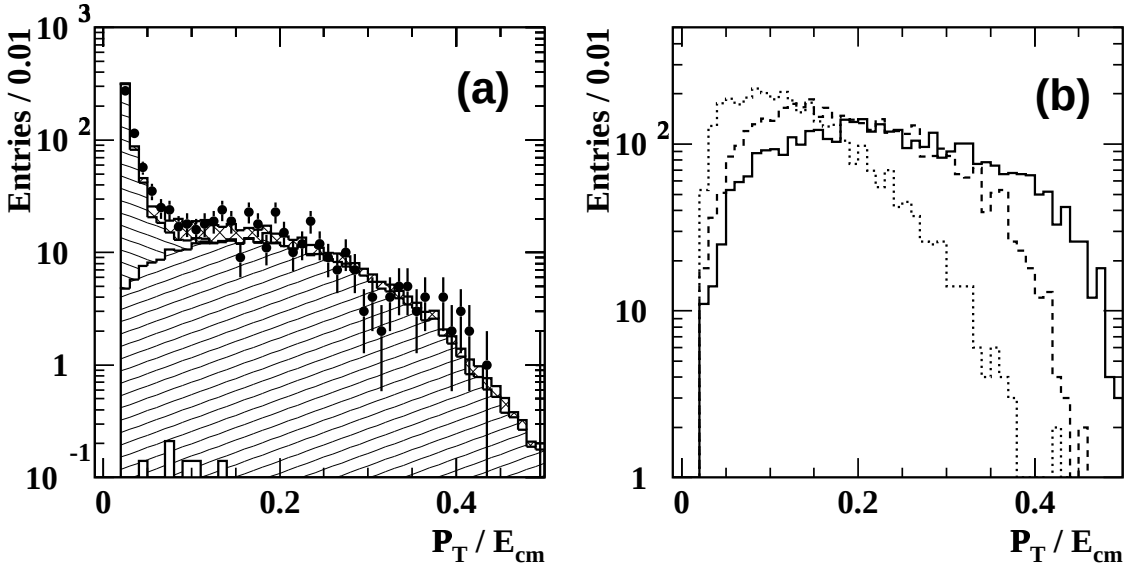

Figure 5.3: *The distributions of the event transverse momentum,P_{T}, normalized by the cms energy. In (a) are shown the data (filled circles with error bars) and expected background:di-lepton events (double hatched area), two-photon processes (negative slope hatching), four-fermion processes (positive slope hatching) and multihadronic events (open area). In (b) predictions from simulated stau events are shown for $\Delta M = 3$ GeV (solid line), 20 GeV (dashed line) and $m_{\tilde{\tau}^+}$ GeV (dotted line).*

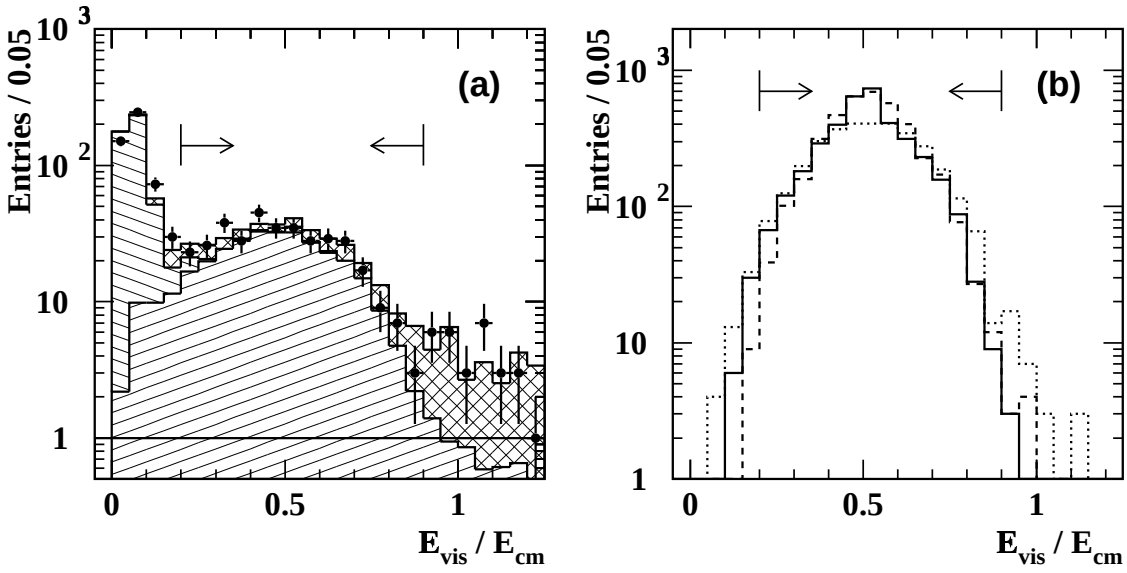

Figure 5.4: *The distribution of the visible energy, $E_{\rm vis}$, divided by the cms energy; (a) for data and background and (b) for the simulated stau events. The symbols, shadings and lines are the same as in Figure 5.3.*

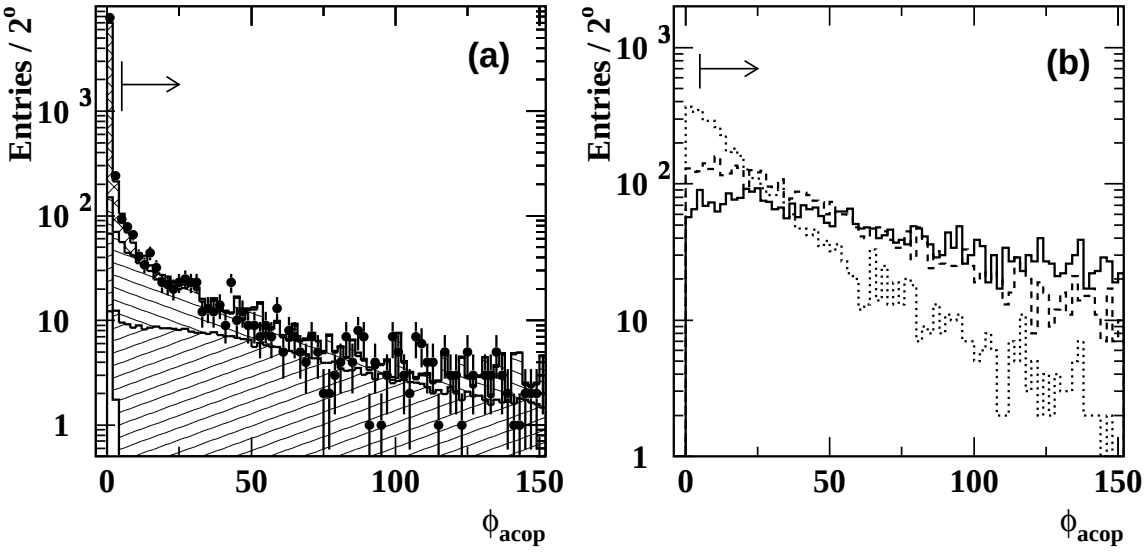

Figure 5.5: *The distributions of the event acoplanarity angle,$\phi_{\rm acop}$, for events; (a) for data and background and (b) for the simulated stau events. The symbols, shadings and lines are the same as in Figure 5.3.*

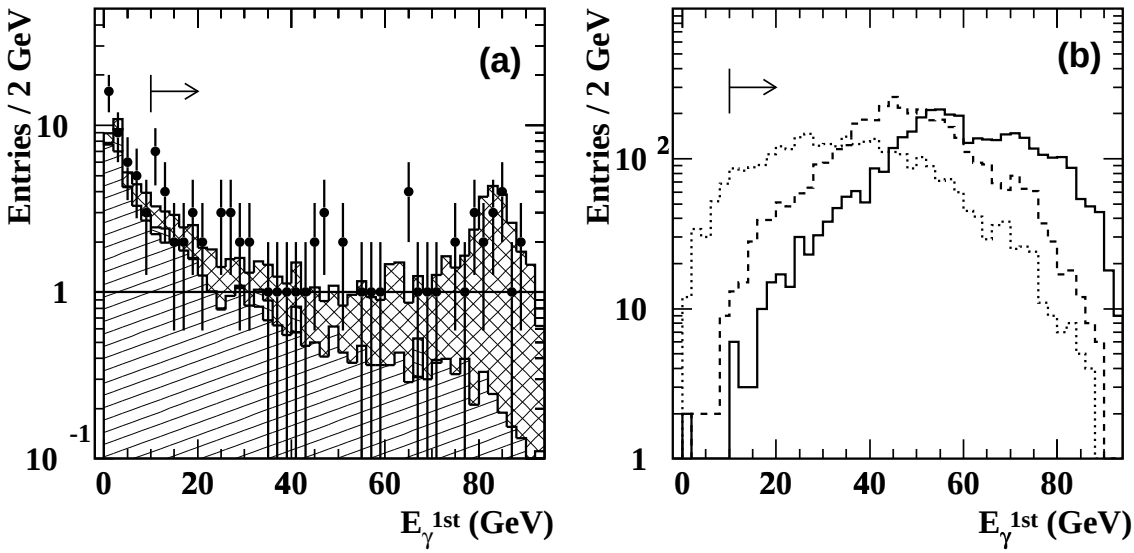

Figure 5.6: *The ECAL cluster energy distribution for data and expected background shown in (a), and for simulated signals in (b). The symbols, shadings and lines are the same as in Figure 5.3.*

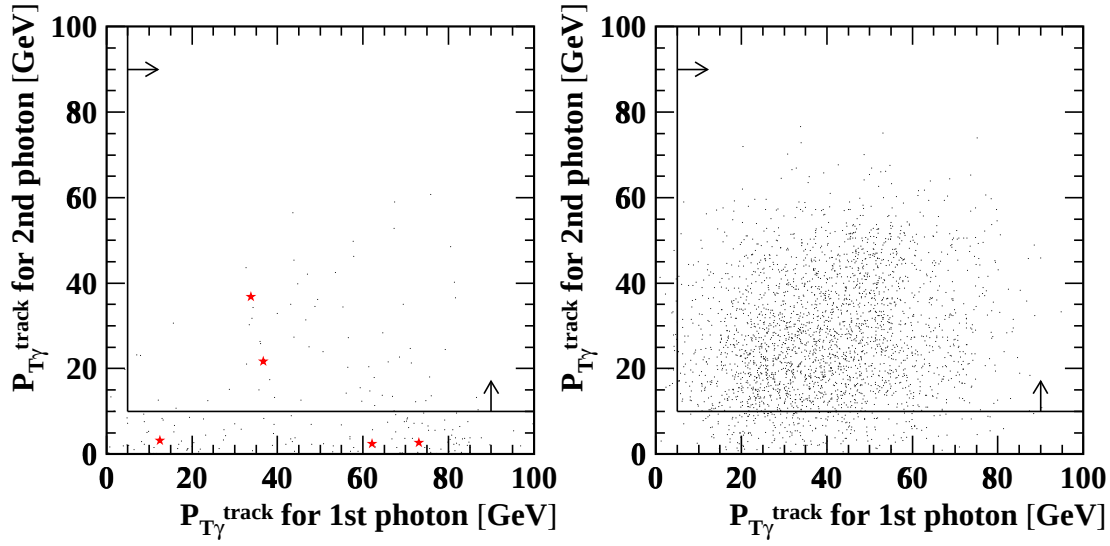

Figure 5.7: *Two-dimensional distribution P_{T} of the 1st photon versus the 2nd photon after requiring two isolated photons, In (a), dot shows background Monte Carlo ($\tau^+\tau^-(\gamma)$, $\ell^+\nu_\ell\ell^-\bar{\nu}_\ell$) and star shows data. In (b) the simulated stau events are shown for ΔM = 3 GeV. The plots of background and signal Monte Calro events are shown with arbitrary normalization.*

- $P_{\rm T}, P_{\rm T}^{\rm w.o.h} > 0.03\sqrt{s}$,
- $0.25\sqrt{s} < E_{\rm vis} < 0.85\sqrt{s}$,
- $\phi_{\rm acop} > 5^\circ$, and
- $N_\gamma \geq 2$.

(B1 - 1) The first and second photons must have large energies. The lower limits on the second photon can strongly reduce events from radiative-return and four-fermion processes;

- $E_\gamma^{\rm 1st} > 20$ GeV for the 1st photon, and
- $E_\gamma^{\rm 2nd} > 10$ GeV for the 2nd photon.

(B1 - 2) The radiative-return multihadronic events or multihadronic events with double ISR's still remained. Such backgrounds are reducible by requiring the visible energy excluding the two photons, $E_{\rm vis}^{\rm ex.\gamma}$, to be less than 50 GeV. The distribution of $E_{\rm vis}^{\rm ex.\gamma}$ is shown in Figure 5.8.

5.5.3 Analysis B2N

This selection is applied for the neutralino production with medium ΔM;

$$\widetilde{\chi}_1^0\widetilde{\chi}_2^0 \to \widetilde{\chi}_1^0\widetilde{\chi}_1^0{\rm Z}^{0(*)} \to \gamma\widetilde{G}\gamma\widetilde{G} + q\bar{q}\,.$$

In this case, both photons and jets are energetic.

(B2N-0) To select events with two isolated photons and missing energy, the following cuts are applied:

- $|\cos\theta_{\rm miss}| < 0.95$,
- $P_{\rm T}, P_{\rm T}^{\rm w.o.h} > 0.03\sqrt{s}$,
- $0.40\sqrt{s} < E_{\rm vis} < 0.95\sqrt{s}$,
- $\phi_{\rm acop} > 5^\circ$, and
- $N_\gamma \geq 2$.

The range of the visible energy, $E_{\rm vis}$, is a little higher than that of Analysis B1, as the missing energy is usually larger than $\sim m_{\widetilde{\chi}_1^0}/2$.

(B2N-1) There is no isolated lepton, $N_\ell^{\rm iso} = 0$. The lepton identifications and isolated condition are described in section 4.1.4 and 4.1.5, respectively.

The $\rm q\bar{q}\ell\bar{\nu}_\ell$ Standard Model background is still left at this stage, because a lepton from W is not always recognized as an isolated lepton when a lepton is included in a jet or a tau lepton is misidentified.

(B2N-2) When particles are split into two jets excluding photons, both jet masses are required to be less than 20 GeV in order to reduce the four-fermion background. Figure 5.10 shows the distribution of the larger jet mass, $M_{\rm jet}^{\rm max}$.

Initial state radiation (ISR) can make a Standard Model event a fake signal. Since most of ISR photons are emitted close to $e^-(e^+)$ beam, they are reduced by $|\cos\theta_\gamma| < 0.9$. Although event including ISR with high $P_{\rm T}$ is not irreducible, such an event can be suppressed by requiring another photon. Dominant background for the second photon might come from a FSR and a neutral hadron, especially π^0's. In addition, $\mathrm{K}^0_{\rm L}$'s, neutrons and overlapping neutral particles like $\mathrm{K}^{*0} \to \mathrm{K}^0_{\rm L}\,\pi^0$ or $\mathrm{K}^0_{\rm S} \to \pi^0\,\pi^0$ fake a signal photon. A prompt photon emitted from a quark at a large angle before fragmentation is not distinguished from signal photon (see Figure 5.9 (a)). On the other hand, photons like Figure 5.9 (b) and (c), distribute around the original charged particle with small angle. They can be removed by a requirement on the transverse momentum with respect to the nearest jets, denoted by $P^{\rm jet}_{{\rm T}\gamma}$.

(B2N-3) The first and second photons are required to be well separated from any jet;

- $P^{\rm jet}_{{\rm T}\gamma} > 10$ GeV for the 1st photon, and
- $P^{\rm jet}_{{\rm T}\gamma} > 5$ GeV for the 2nd photon,

where jets are reconstructed by Durham Algorithm with $k_T = 20$ GeV. Figure 5.11 shows the distribution of $P^{\rm jet}_{{\rm T}\gamma}$ for the second photon.

5.5.4 Analysis B3N

In the case of $\widetilde{\chi}^0_1\widetilde{\chi}^0_2$ production with large ΔM, a real Z^0 boson is always produced and two energetic jets should be observed in the final state. When a photon is emitted to the opposite direction to the neutralino direction, the photon energy becomes very small due to a large boost factor of the primary $\widetilde{\chi}^0_1$. Dominant backgrounds are radiative-return multihadronic events and four-fermion $\mathrm{q\bar{q}}\ell\bar{\nu}_\ell$ events with the lepton not identified as an isolated lepton.

(B3N-0) To select events with two isolated photons and missing energy, the same selection as (B2N-0) is applied.

In the large ΔM case, signal events look very similar to radiative-return multihadronic events, but photons of the signal events cannot have so large energy as those of the radiative-return events.

(B3N-1) The first photon energy must be less than 60 GeV.

(B3N-2) The most energetic photon tends to distribute in the direction opposite to Z^0. The angle between the Z^0 direction reconstructed from the two jets and the most energetic photon should be greater than 110° ($\phi_{\gamma-\mathrm{Z}^0} > 110^\circ$). The distribution of $\phi_{\gamma-\mathrm{Z}^0}$ is shown in Figure 5.12.

(B3N-3) $P^{\rm jet}_{{\rm T}\gamma}$ for the first and second photons are required to be;

- $P^{\rm jet}_{{\rm T}\gamma} > 5$ GeV for the 1st photon, and
- $P^{\rm jet}_{{\rm T}\gamma} > 3$ GeV for the 2nd photon .

5.5.5 Analysis B2C

This selection is employed for signal events where both W's decay into a quark pair;

$$\widetilde{\chi}^+_1\widetilde{\chi}^-_1 \to \widetilde{\chi}^0_1\widetilde{\chi}^0_1\mathrm{W}^+\mathrm{W}^- \to \gamma\widetilde{G}\gamma\widetilde{G} + q\bar{q}q\bar{q}\,,$$

for chargino with medium ΔM. W is not produced on-shell and 2-jet sometimes looks like a mono-jet. A signal event in which one W decays into $q\bar{q}$ and the other decays into $\ell\nu$ might be included in Category (B) if the lepton is not identified as an isolated lepton.

(B2C - 0) To select events with missing energy and reduce two-photon and two-fermion background events, the following selection is applied;

- $|\cos\theta_{\rm miss}| < 0.95$,
- $P_{\rm T}, P_{\rm T}^{\rm w.o.h} > 0.03\sqrt{s}$,
- $0.40\sqrt{s} < E_{\rm vis} < 0.95\sqrt{s}$,
- $\phi_{\rm acop} > 5^\circ$, and
- $N_\gamma \geq 2$.

(B2C - 1) There is no isolated lepton, $N_\ell^{\rm iso} = 0$.

(B2C - 2) At this level, there are still backgrounds from $W^+W^- \to q\bar{q}q\bar{q}$, $W^+W^- \to q\bar{q}\ell\bar{\nu}_\ell$ and $Z^0 \to q\bar{q}$. To suppress these backgrounds, different vetoes are applied according to the number of jets which is defined with $M_{\rm jet}^{\rm max} < 15$ GeV.

- $N_{\rm jet}$ = 4 : When an event is identified as 4-jet, the four jets are grouped into two pairs of jets so that the masses of the two jet pairs are close to m_W by minimizing the following value;

$$(M_{ij} - M_{\rm W})^2 + (M_{kl} - M_{\rm W})^2 \qquad i,j,k,l = 1,2,3,4\,.$$

  The angle between the two jet pairs should be less than 150°.

- $N_{\rm jet}$ = 3 : In the case of 3-jet, two jets are chosen among the three so that the invariant mass of the two jets is close to m_W. The vector $\overrightarrow{P}_1$ is defined as the momentum sum of the two jets, while $\overrightarrow{P}_2$ is defined as that of the remaining jet and the missing momentum. The angle between $\overrightarrow{P}_1$ and $\overrightarrow{P}_2$ must be less than 150°.

- $N_{\rm jet}$ = 2 : The sum of three opening angles among $\overrightarrow{P}_1$, $\overrightarrow{P}_2$, and the direction of the first photon, $\phi_{\Sigma{\rm open}}$, is required to be less than 356°.

Figure 5.13 shows the distribution of $\phi_{\Sigma{\rm open}}$ for events classified as two jets.

(B2C - 3) Both photons should be far from any jets;

- $P_{{\rm T}\gamma}^{\rm jet}$ for 1st photon > 10 GeV, and
- $P_{{\rm T}\gamma}^{\rm jet}$ for 2nd photon > 5 GeV.

Here, jets are reconstructed with k_T = 15 GeV.

5.5.6 Analysis B3C

The background situation becomes worse as ΔM increases. The final state of chargino pair production with large ΔM is similar to that of the W^+W^- production.

(B3C - 0) At first, the following selection is applied, which is the same as that of B2C;

- $|\cos\theta_{\rm miss}| < 0.95$,

- $P_{\rm T}, P_{\rm T}^{\rm w.o.h} > 0.03\sqrt{s}$,
- $0.40\sqrt{s} < E_{\rm vis} < 0.95\sqrt{s}$,
- $\phi_{\rm acop} > 5^\circ$, and
- $N_\gamma \geq 2$.

(B3C -1) There is no isolated lepton, $N_\ell^{\rm iso}$ = 0.

(B3C -2) In order to reduce radiative-return multihadronic events, the first photon energy must be less than 60 GeV.

(B3C - 3) To reduce the background from the $\mathrm{q\bar{q}}\ell\bar{\nu}_\ell$ Standard Model processes, well-separated four jets are required. When particles are split into four jets using Durham algorithm, k_T should be greater than 4 GeV. Figure 5.14 shows the k_T distribution when particles are reconstructed as a 4-jets event.

(B3C - 4) Loose cuts on $P_{{\rm T}\gamma}^{\rm jet}$ are applied because signal photons cannot have large energies;

- $P_{{\rm T}\gamma}^{\rm jet} > 5$ GeV for the 1st photon, and
- $P_{{\rm T}\gamma}^{\rm jet} > 3$ GeV for the 2nd photon.

Here, jets are reconstructed using Durham algorithm with k_T = 15 GeV.

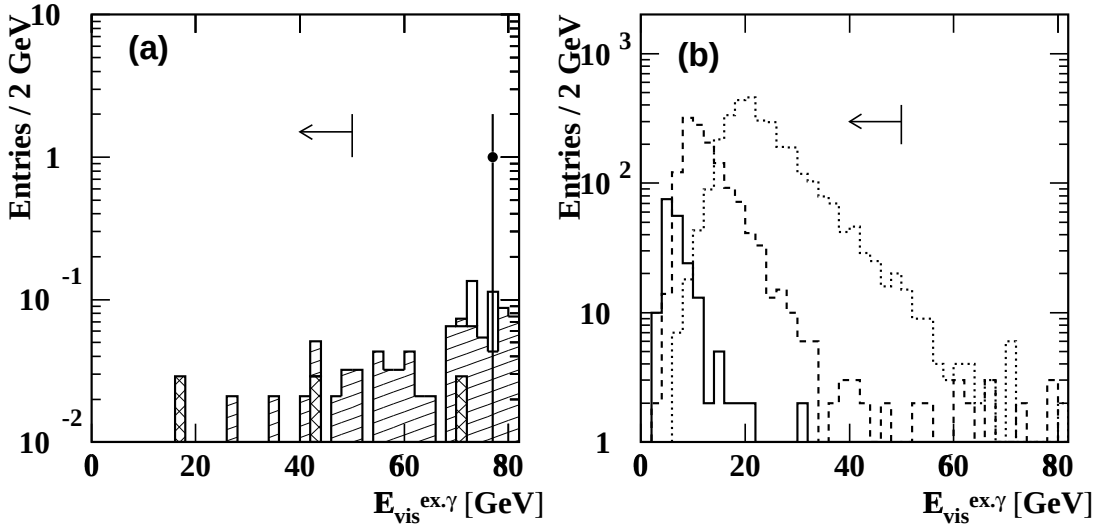

Figure 5.8: *The distribution of visible energy excluding the two photons after applying all other cuts; (a) for data and background Monte Carlo, and (b) for chargino signal with ΔM=3 GeV (solid line), 5 GeV (dashed line) and 10 GeV (dotted line).*

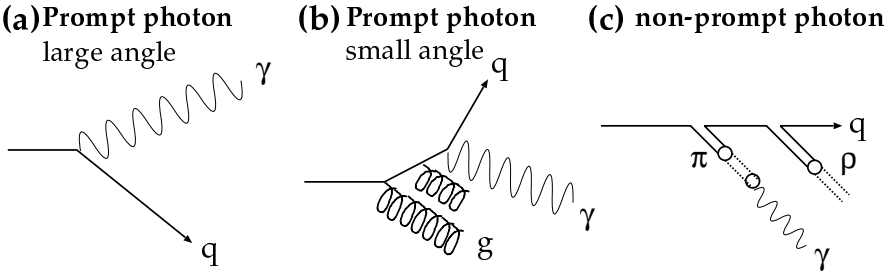

Figure 5.9: *The three regimes for photon radiation off the final quarks for (a) large angle emission, (b) small angle emission and (c) emission of photons at limited transverse momentum* $p_\perp = \mathcal{O}(\Lambda_{\mathrm{QCD}})$.

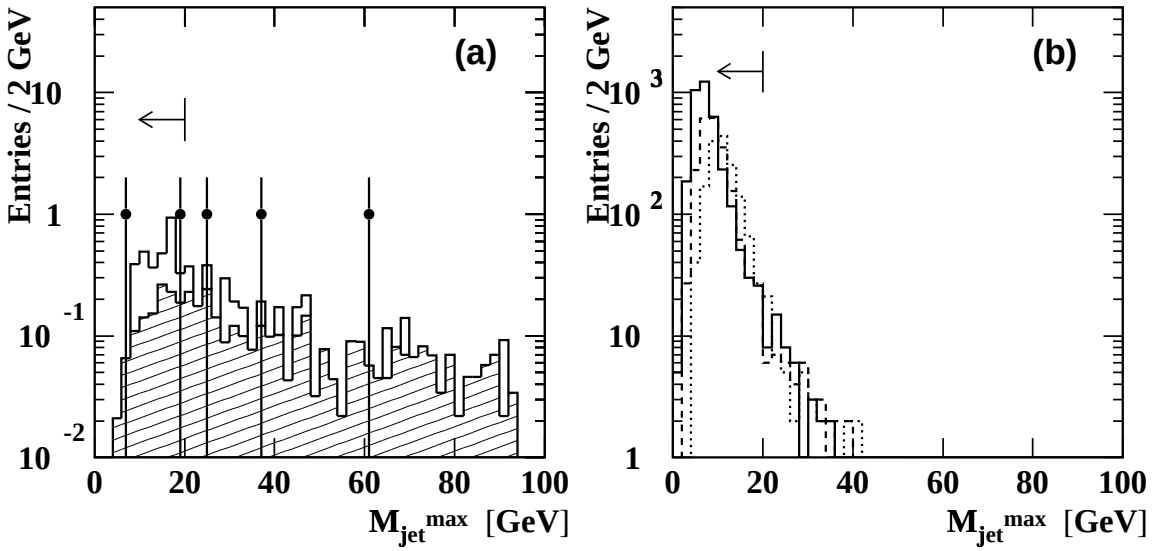

Figure 5.10: *The distribution of the maximum jet mass is shown after splitting particles into two jets; (a) for background Monte Carlo and data, (b) for neutralino signal with* ΔM *=40 GeV (solid line), 70 GeV (dashed line) and 110 GeV (dotted line).*

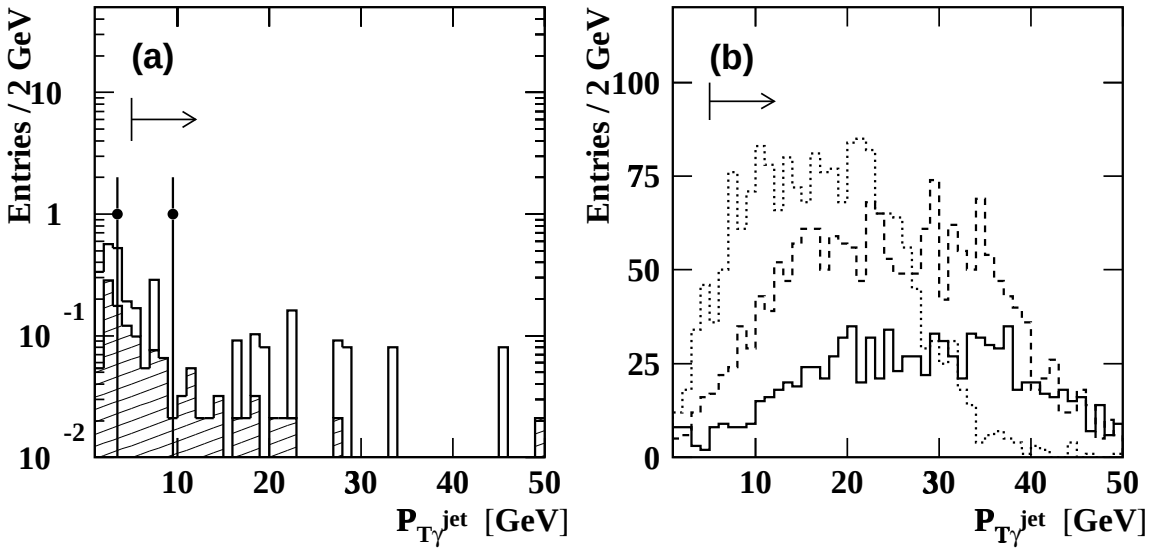

Figure 5.11: *The distribution of photon's transverse momentum with respect to the nearest jet for second photon; (a) for background Monte Carlo and data, (b) for neutralino signal. The lines in (b) are the same as Figure 5.10.*

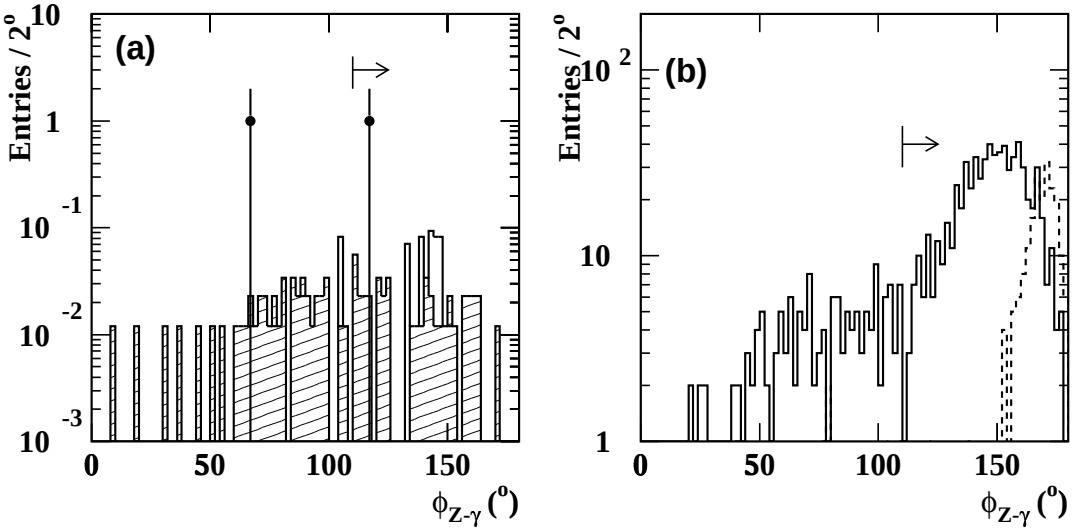

Figure 5.12: *The distribution of the angle between Z^0 direction and the most energetic photon is shown; (a) for background Monte Carlo and data, and (b) for neutralino signal with ΔM=150 GeV (solid line) and 190 GeV (dashed line).*

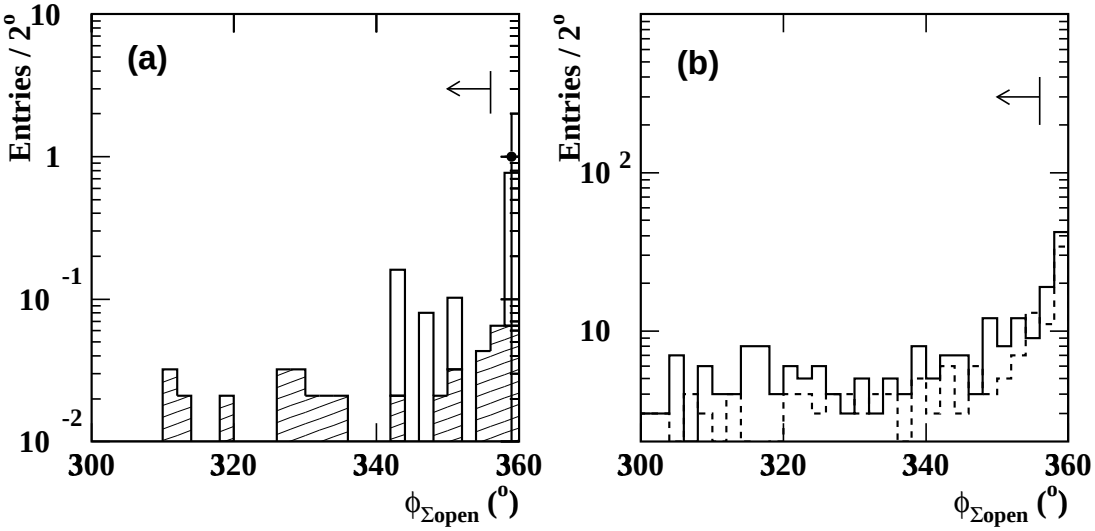

Figure 5.13: *The distribution of the sum of opening angle among two jets and the first photon; (a) for background Monte Carlo and data, and (b) for chargino signal with* $\Delta M = m_{\tilde{\chi}^+}/2$ *GeV (solid line),* $m_{\tilde{\chi}^+} - 30$ *GeV (dashed line).*

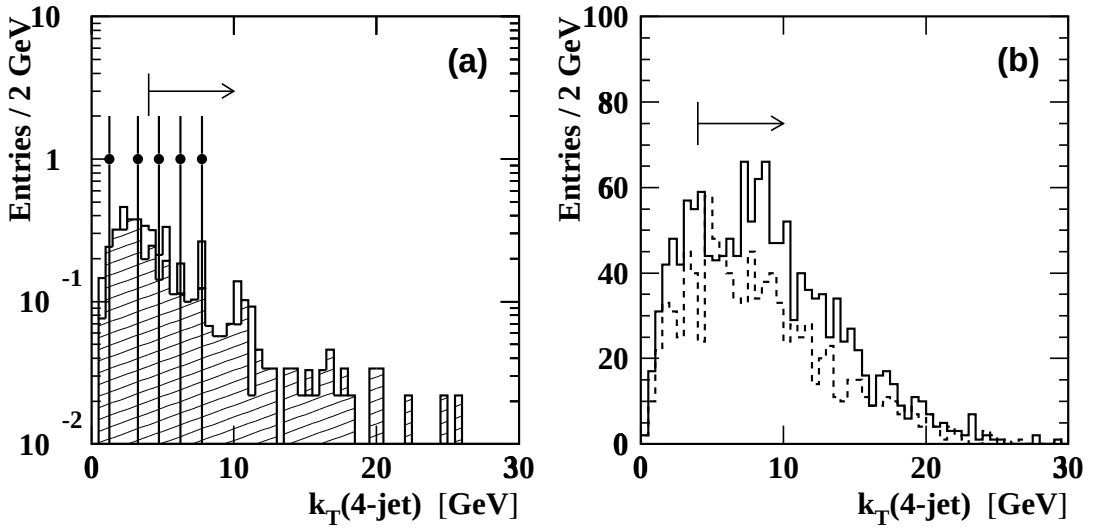

Figure 5.14: *The* k_T *distribution when particles are split into four jets is shown (a) for background Monte Carlo and data, (b) for chargino signal with* $m_{\tilde{\chi}_1^+} - 20$ *GeV (solid line) and* $m_{\tilde{\chi}_1^+} - 10$ *GeV (dashed line).*

5.5.7 Analysis C1

This selection is employed for the $\widetilde{\chi}_1^+\widetilde{\chi}_1^-$ production where one W decays into lepton plus neutrino and the other decays into a pair of quarks;

$$\widetilde{\chi}_1^+\widetilde{\chi}_1^- \to \widetilde{\chi}_1^0\widetilde{\chi}_1^0\mathrm{W}^+\mathrm{W}^- \to \gamma\widetilde{G}\gamma\widetilde{G} + \mathrm{q\bar{q}}\ell\bar{\nu}_\ell\,.$$

This analysis is optimized to chargino events with medium ΔM.

(C1 - 0) The following cuts are applied at first;

- $|\cos\theta_{\mathrm{miss}}| < 0.95$,
- $P_{\mathrm{T}}, P_{\mathrm{T}}^{\mathrm{w.o.h}} > 0.03\sqrt{s}$,
- $0.40\sqrt{s} < E_{\mathrm{vis}} < 0.95\sqrt{s}$,
- $\phi_{\mathrm{acop}} > 5^\circ$, and
- $N_\gamma \geq 2$.

(C1 - 1) An event is required to have at least one isolated lepton.

(C1 - 2) Excluding the two photons and the most energetic isolated lepton, the remaining paricles are split into two jets using Durham algorithm. To require the photons apart from the other particles (a jet or a lepton), cuts are applied on $P_{\mathrm{T}\gamma}^{\mathrm{jet/lepton}}$ of the two photons;

- $P_{\mathrm{T}\gamma}^{\mathrm{jet/lepton}}$ for the 1st photon > 10 GeV, and
- $P_{\mathrm{T}\gamma}^{\mathrm{jet/lepton}}$ for the 2nd photon > 5 GeV.

(C1 - 3) Events from the $\mathrm{q\bar{q}}\ell\bar{\nu}_\ell$ Standard Model process still survive the above selection. In the case of chargino with medium ΔM, W is virtually produced. Cuts on the energy of the isolated lepton and the invariant mass of the two jets;

- $E_{\mathrm{lepton}} < 40$ GeV and $M_{ij} < 70$ GeV

are useful to reduce the remaining background. The distributions of the E_{lepton} versus M_{ij} for the $\mathrm{q\bar{q}}\ell\bar{\nu}_\ell$ background, data, and the simulated chargino events are shown in Figure 5.15.

5.5.8 Analysis C2

For the chargino with a large ΔM, it is difficult to tell the signal from the background, as the signal event, is very similar to a $\mathrm{W}^+\mathrm{W}^- \to \mathrm{q\bar{q}}\ell\bar{\nu}_\ell$ event.

(C2 - 0) The following cuts are applied at first;

- $|\cos\theta_{\mathrm{miss}}| < 0.95$,
- $P_{\mathrm{T}}, P_{\mathrm{T}}^{\mathrm{w.o.h}} > 0.03\sqrt{s}$,
- $0.40\sqrt{s} < E_{\mathrm{vis}} < 0.95\sqrt{s}$,
- $\phi_{\mathrm{acop}} > 5^\circ$, and

- $N_\gamma \geq 2$.

(C2 - 1) Events must have at least one isolated lepton, $N_\ell^{\rm iso} \geq 1$. Additionally, the lepton energy is required to be greater than 5 GeV.

(C2 - 2) Excluding the two photons and the isolated lepton, particles are devided into two jets using Durham algorithm. The transverse momenta of the photons with respect to the nearest particle (a jet or a lepton) should be large enough;

- $P_{\rm T\gamma}^{\rm jet/lepton} > 5$ GeV for the 1st photon, and
- $P_{\rm T\gamma}^{\rm jet/lepton} > 3$ GeV for the 2nd photon.

(C2 - 3) Finally, a veto is applied to reduce $\rm W^+W^- \to q\bar{q}\ell\bar{\nu}_\ell$ events. The angle between the two reconstructed W's should be less than 170°.

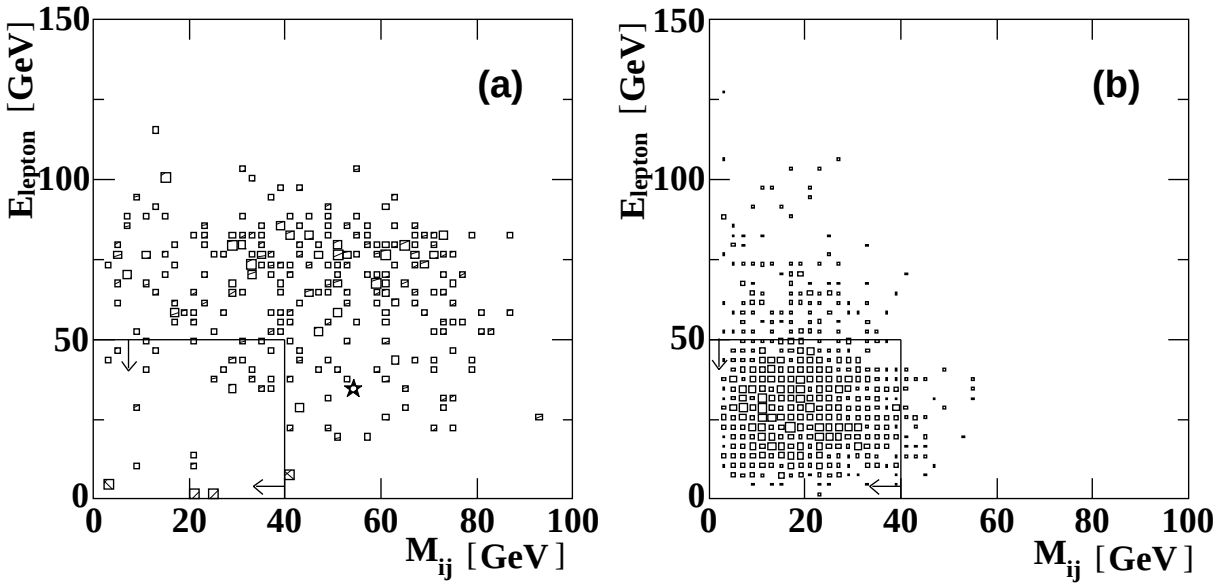

Figure 5.15: *The distribution of $E_{\rm lepton}$ vs. M_{ij}; (a) for data (star) and $\rm q\bar{q}\ell\bar{\nu}_\ell$ background Monte Carlo, and (b) for chargino signal Monte Carlo with ΔM=20 GeV. The plots of background and signal Monte Calro events are shown with arbitrary normalization.*

5.6 Candidate Events

In this section candidate events of this search are reported in the OPAL data sample collected in 1999 and 2000. The table 5.2 summarizes all candidates and the corresponding analyses. The numbers of observed candidates and the expected Standard Model background are shown in Table 5.3 for each analysis. An interpretation is given below for each candidate within both the Standard Model and Supersymmetry.

Candidates in Category A

Analysis A is employed for the topology *"photons plus leptons with missing energy"*. Two events survive *Analysis A*, while 2.2 events are expected from the Standard Model source. Table 5.4 summarizes characteristic variables of the candidate events. They are shown in Figure 5.16 and Figure 5.17,

respectively.

The event (# run=12998 , # evt=41774) has the two charged tracks, which are identified as a muon and an electron, respectively. Therefore, it can be a signal of $\tilde{\tau}_1^+\tilde{\tau}_1^-$, $\tilde{\chi}_1^+\tilde{\chi}_1^-$ or $\tilde{\chi}_1^0\tilde{\chi}_2^0$ production considering the lepton flavors. The other candidate (# run=13452 , # evt=13908) has two muons, and can be considered as a signal of any process except $\tilde{e}_1^+\tilde{e}_1^-$ events. If they are signals with the GMSB scenario, SUSY particles with medium ΔM are suitable considering of the lepton and photon energies.

Within the Standard Model, they can be interpreted $Z^0 \to \tau^+\tau^-$ with double ISR's or ISR/FSR. The recoil mass of two photons ${M_{\rm recoil}^{\gamma\gamma}}^2$ is a little larger than m_{Z^0} (see Table 5.4) in both candidate events. Considering these two photons as ISR's, the third ISR photon may have escaped to the beam pipe.

Candidates in Category B

Five different analyses, *Analyses B1, B2N, B3N, B2C* and *B3C* are employed for the signal topology of "*photons plus jets with missing energy*". In any analysis, the number of observed events is consistent with the expected number from the Standard Model processes within statistical fluctuation.

The event (# run 15894 , # evt 40261) survives *Analysis B2N, B3N* and *B2C*, and it is shown in Figure 5.18. The first photon is identified as a conversion photon. Within the Standard Model, this event might be interpreted $W^+W^- \to q\bar{q}e^-\bar{\nu}_e$, where the electron interacts with materials and radiates a photon followed by a photon conversion. Figure 5.19 shows an enlarged view of CJ region. There is one track with silicon hits around conversion tracks and it is considered as electron. The second photon (E_γ=11.3 GeV) might be radiated from the electron. The reconstructed mass of the other particles is 71.6 GeV.

The event (# run 12193 , # evt16571) shown in Figure 5.20 is a candidate selected with *Analyses B2C* and *B3C*. In this event, three hard photons are observed. The ECAL3 (see Figure 5.20) may be a photon radiated from the electron (CTR1) because ECAL3 direction is tangential to an arc of CTR1 track. The ECAL1 might be a neutral hadron or FSR since the reconstructed mass of ECAL1 and jets is near to m_W. Considering the origin of ECAL3 and the reconstructed mass being close to m_W, this event can be considered as $W^+W^- \to q\bar{q}e^-\bar{\nu}_e$ with ISR (ECAL2).

The event (# run 12456 , # evt 60091) is selected with *Analysis B2C*. There is a large uncertainty on the energy measurement. One reason is that the event has a considerable energy deposit in HCAL, and the second reason is that there is a possibility of some particles going through to the beam pipe direction since there is an activity of the forward detecor (1.5 GeV). Taking account of the uncertainty of the energy measurement, the event might be a radiative-return multihadronic event and the second photon comes from a neutral hadron.

The event (# run 11623 , # evt 40904) is selected as a candidate with *Analyses B2C* and *B3C*. The recoil mass of the two photons is 88.6 GeV. Probably, this event comes from a multihadronic event with double ISR's.

The event (# run 15301 , # evt 6597) results from *Analysis B2C*. It might be from $W^+W^- \to q\bar{q}e\nu$ followed by photon radiation from electron.

The event (# run 11235 , # evt 74747) is selected with *Analysis B2C* and *B3C*. It can be considered that this event arises from $W^+W^- \to q\bar{q}\tau\nu$ process. The reconstructed mass of JET1 and JET2 is

[2]The recoil mass of two photons is defined as $M_{\rm recoil}^{\gamma\gamma} = \sqrt{(E_{\rm vis} - E_\gamma^{\rm 1st} - E_\gamma^{\rm 2nd})^2 - (\vec{\mathbf{P}}_\gamma^{\rm 1st} + \vec{\mathbf{P}}_\gamma^{\rm 2nd})^2}$.

61.4 GeV. The difference from m_{W} might come from JET1 which directs forward and is not measured correctly. The mass of JET3 is 4.5 GeV and a little larger than a mass of tau-lepton. The second photon can be considered as FSR or a neutral hadron.

Candidates in Category C

No candidate is found by any analysis in Category C. The numbers of expected events from the Standard Model processes with *Analysis C1* and *C2* are 0.2 and 0.9, respectively.

$\sqrt{s}$	#run	#event	A	B					C	
(GeV)			A	B1	B2N	B3N	B2C	B3C	C1	C2
206.4	15894	40261			√	√	√			
206.3	15301	6597						√		
205.4	13452	13908	√							
204.9	12998	41774	√							
199.7	11623	40904					√	√		
199.6	12193	16571					√	√		
199.6	12456	60091					√			
199.6	11817	47964					√			
191.6	11235	74747					√	√		

Table 5.2: *Candidates selected in Category A,B and C. A tick indicates the analysis in which the candidates are found.*

	A	B1	B2N	B3N	B2C	B3C	C1	C2
n_{obs}	2	0	1	1	6	4	0	0
n_{exp}	2.2	0.2	2.7	1.5	4.1	1.8	0.2	0.9

Table 5.3: *The numbers of observed events and expected events in the Standard Model are shown for each analysis in Category A, B and C.*

# run	# evt	$\sqrt{s}$	P_{T}	E_ℓ	$M^{\gamma\gamma}_{\mathrm{recoil}}$	E_γ (GeV)		$P^{\mathrm{track}}_{\mathrm{T}\gamma}$ (GeV)	
		(GeV)	(GeV/c)	(GeV)	(GeV/c^2)	1st	2nd	1st	2nd
12998	41774	204.9	37.7	e (20.1), μ (14.5)	119.8	55.1	22.2	37.1	21.8
13452	13908	205.4	33.8	μ (37.7), μ (9.6)	103.4	42.0	40.1	32.8	37.3

Table 5.4: *The characteristic event variables of the two candidates.*

5.7 Systematic Uncertainties

There is no significant excesss from the number of expected events with the Standard Model. Therefore, the results can be translated into upper limits on the signal cross-sections. The systematic uncertainties of the upper limits depend on those of the integrated luminosity and the signal efficiency. However, since the error on the integrated luminosity is only $\sim 0.5\,\%$ and thus totally negligible, the

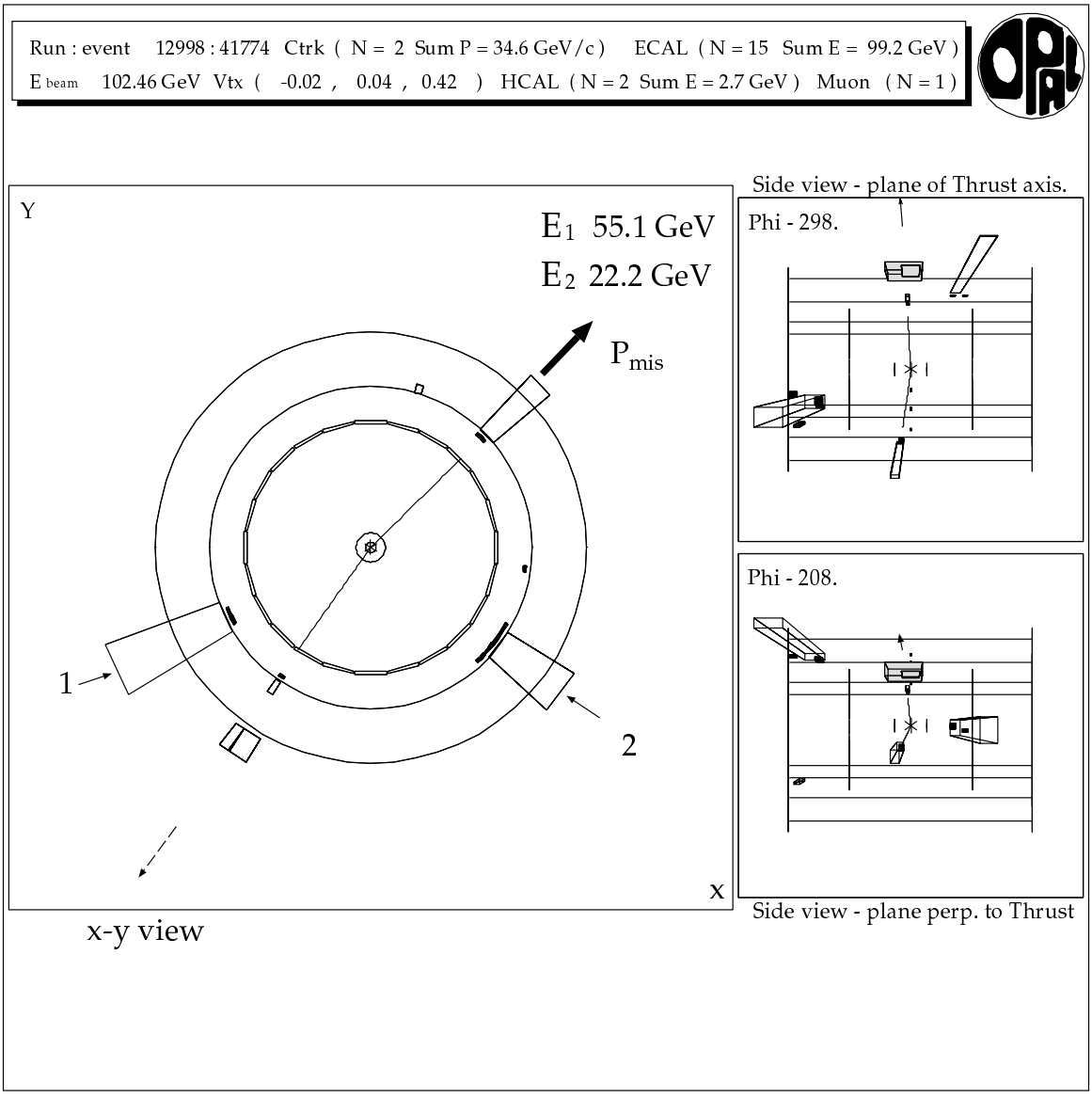

Figure 5.16: *The candidate (#run=12998 , #evt=41774) selected by Analysis A.*

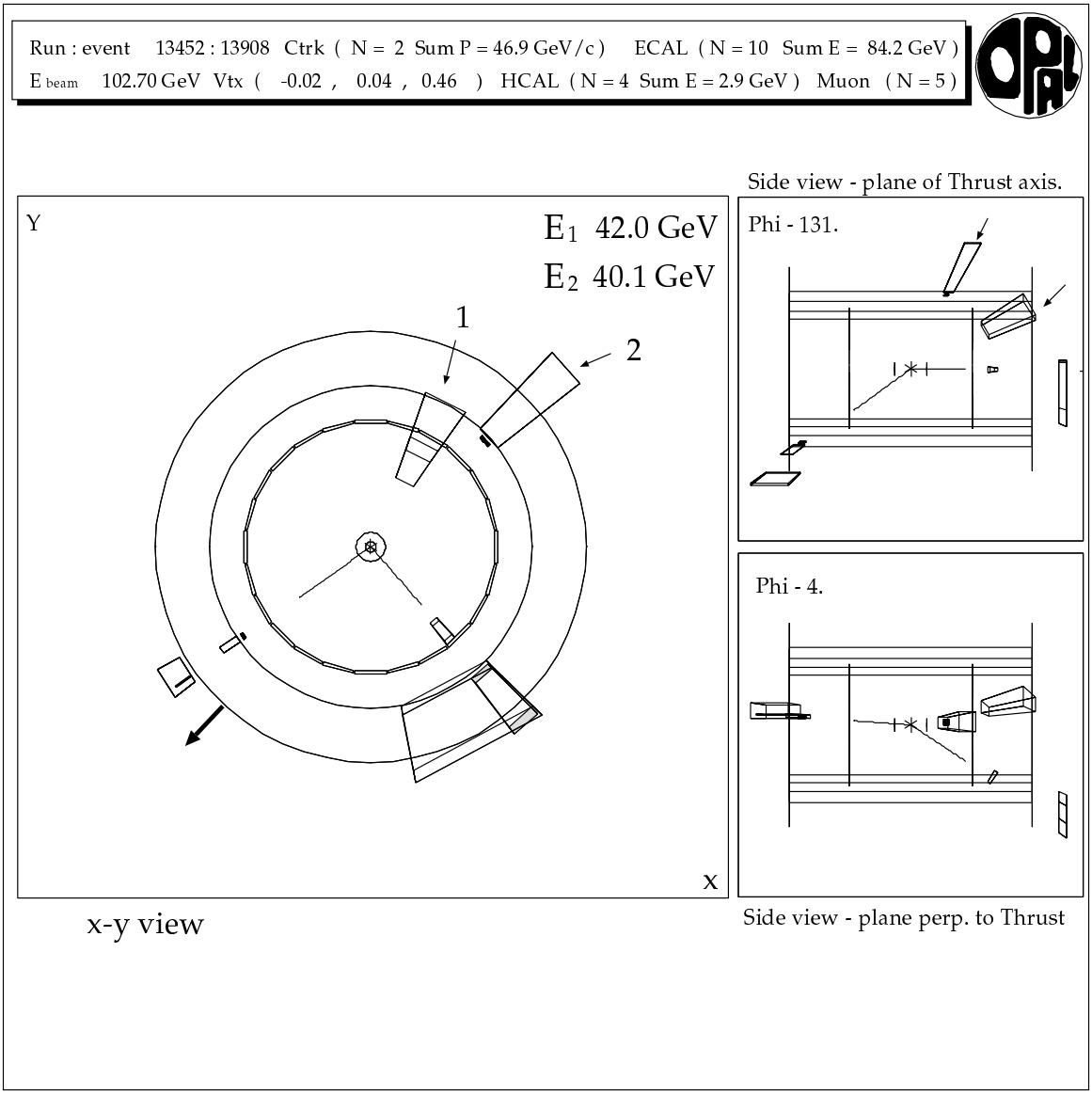

Figure 5.17: *The candidate (#run=13452 , #evt=13908) selected by Analysis A.*

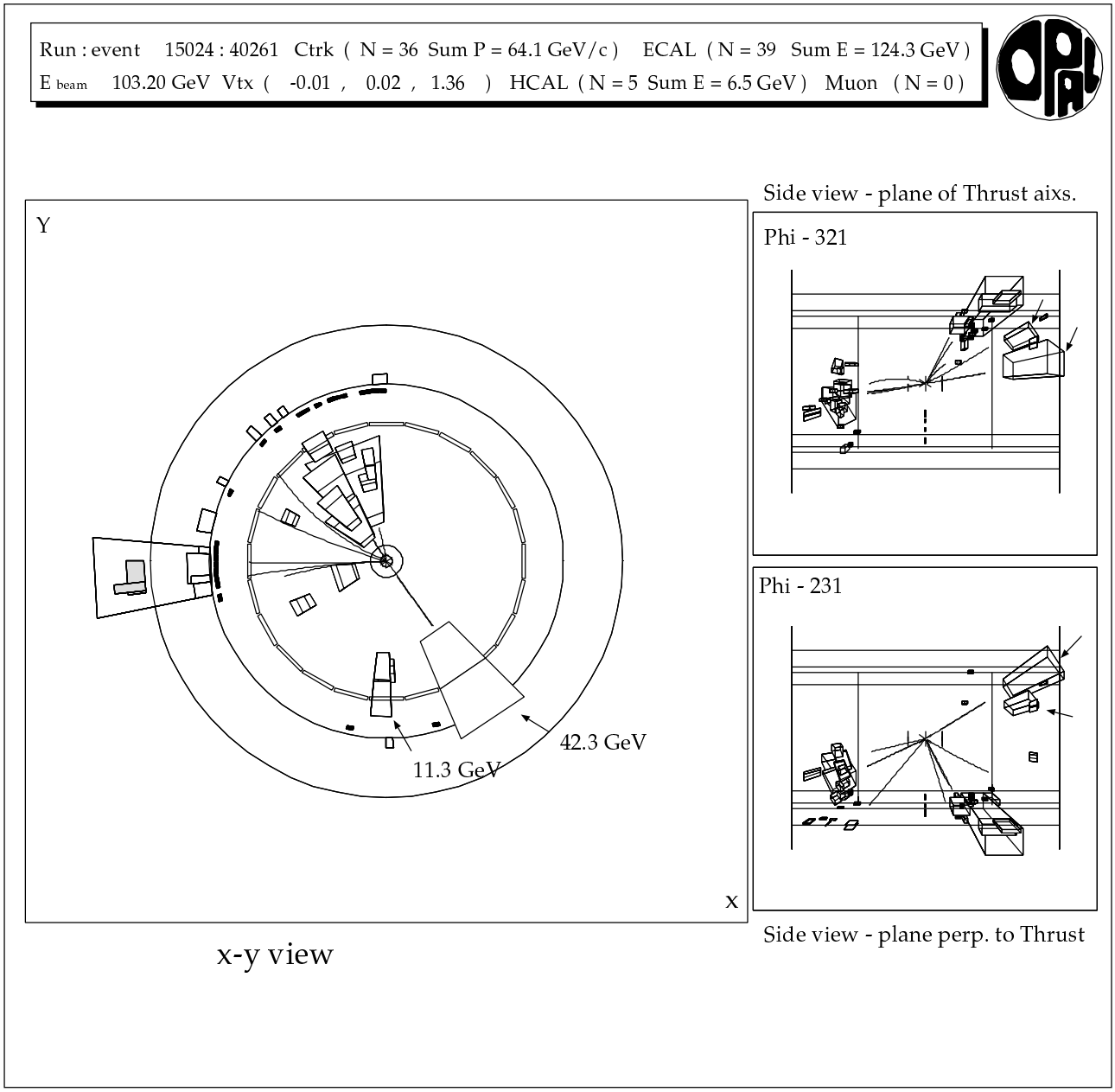

Figure 5.18: *The candidate (#run=15894 , #evt=40261) selected in Analyses B2N, B3N and B2C.*

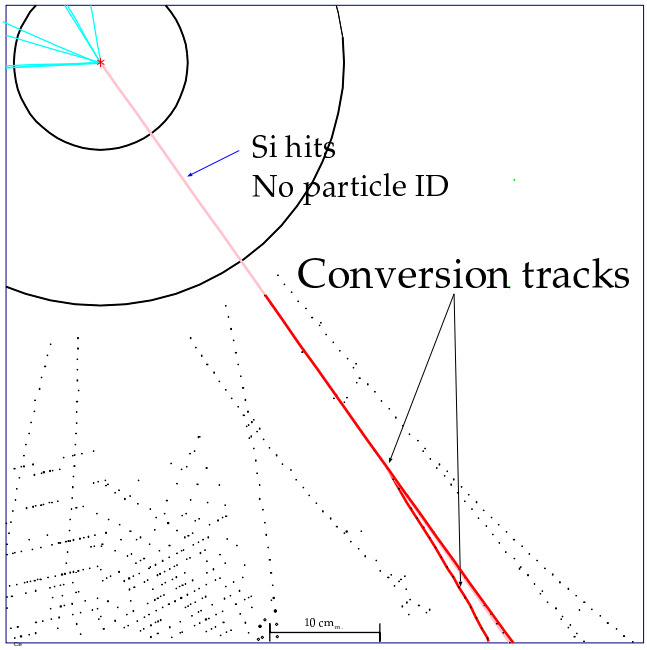

Figure 5.19: *The candidate (#run=15894 , #evt=40261) selected by Analyses B2N, B3N and B2C. The tracking detector region is enlarged.*

systematic studies concentrate on the evaluation of the uncertainties of the detection efficiency.

5.7.1 Uncertainties for an isolated photon identification

Both a modeling of photon emissions and the detector simulation can be considered as the potential sources of systematic uncertainties. For the isolated photon selection, following uncertainties can be considered;

- *Photon radiation rate and energy distribution* depend on a treatment for QED corrections,
- *Losses due to the isolation requirement* depend on the fragmentation,
- *Contributions of isolated neutral hadron* depend on fragmentation and hadronization, and
- *A conversion photon identification* depends on the detector simulation.

Although these are independent to each other, it is difficult to evaluate these uncertainties separately. Here, the differences between the data and the Monte Carlo simulation on selection efficiencies of the isolated photon.

Uncertainty on the isolation due to fragmentation

The systematic error associated with the isolation requirements depends on the accuracy of the Monte Carlo simulation of the fragmentation process in hadronic jets. This is checked by using multi-hadronic events recorded around the Z^0 peak during the 1999 and 2000 runs. At first, the following selection criteria are applied to select multihadronic events;

- $\sum E_{\rm raw}/\sqrt{s} \geq 0.1$,
- $|\sum E_{\rm raw} \cos\theta|/\sum E_{\rm raw} \leq 0.65$,

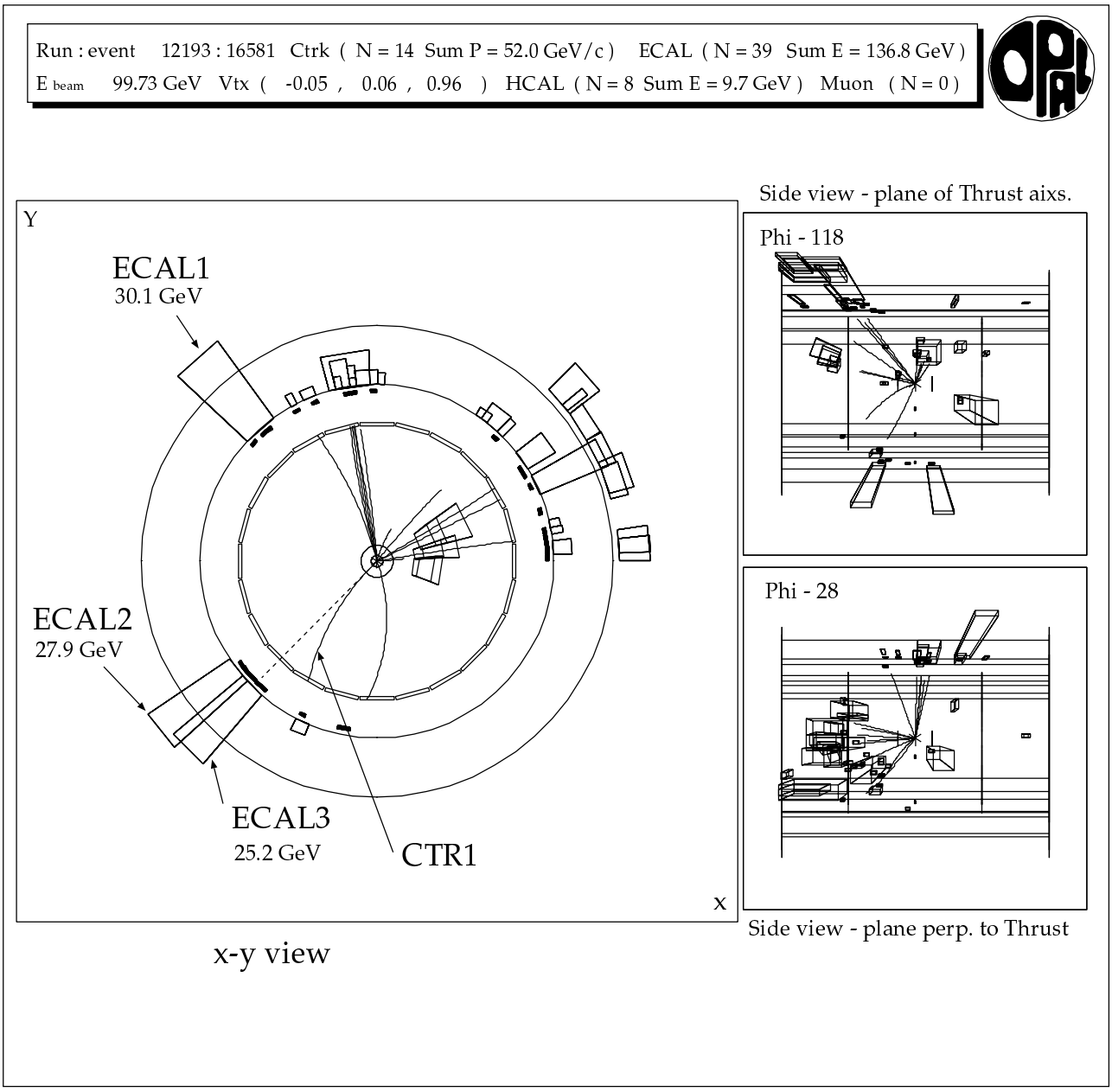

Figure 5.20: *The candidate (#run=12193 , #evt=16571) selected in Analyses B2C and B3C.*

- the number of good ECAL clusters ≥ 7 ,
- the number of good charged tracks ≥ 5 , and
- $M_{\rm vis} > 60$ GeV ,

where, $E_{\rm raw}$ is the ECAL cluster energy without correction. For each selected event, the inefficiency of the isolation requirements is determined for random orientations of the isolation cone and parametrized as a function of the angle between the cone and the nearest jet (Figure 5.22). Here an isolation requirement is $E_{15} < 2$ GeV. For all the jet-cone angles the inefficiency in the Monte Carlo and the real data agree to ~ 1 %. Consequently a 1 % systematic error is assigned.

Uncertainty on the photon candidates.

In the high multiplicity events, photons radiated by quarks and hadrons are dominant backgrounds as well as ISR. ISR is treated with $\mathcal{O}(\alpha^3 L^3)$ accuracy while the treatment of FSR is performed by JETSET showering algorithm, which cannot reproduce hard photons. Data collected around Z^0 is useful to study FSR because ISR is suppressed due to the Z^0 resonance. The error on the selection efficiency of isolated photons is studied using a large amount of data sample around $\sqrt{s}$ = 91 GeV collected in 1992-1994.

To select well-measured multihadronic events and to remove two-photon events, following selections are applied;

- $\sum E_{\rm raw}/\sqrt{s} \geq 0.1$,
- $|\sum E_{\rm raw} \cos\theta| / \sum E_{\rm raw} \leq 0.65$,
- the number of good ECAL clusters ≥ 7 ,
- the number of good charged tracks ≥ 5 ,
- $M_{\rm vis} > 60$ GeV , and
- $|\cos\theta_{\rm thrust}| < 0.8$.

The condition on photon isolation used in "*photons plus X with missing energy*" analyses are;

- $E_\gamma > 3$ GeV ,
- $|\cos\theta_\gamma| < 0.9$, and
- $E_{15} < 2$ GeV .

Figure 5.21 shows the difference of the number of isolated photon candidates between the real data and the Monte Carlo simulation for photons with $P_{{\rm T}\gamma}^{\rm jet} > 10$ GeV. The errors include the differences with some k_T values as well as the statistical errors. There is ~ 20 % excess in the real data for photon with $E_\gamma < 20$ GeV. As a result, a 20 % systematic error is assigned.

5.7.2 Statistical uncertainties

The uncertainties are estimated due to the limited statistics of the signal Monte Carlo samples and also due to the accuracy of the efficiency parameterization used to derive the limits. For chargino detection, the detection efficiency $\epsilon\,(m_{\tilde{\chi}_1^+}, \Delta M)$ has a statistical uncertainty

$$\frac{\delta\epsilon}{\epsilon} = \pm\sqrt{\frac{(1-\frac{n}{n_0})}{n}}\,, \tag{5.1}$$

where n_0 is the generated number of events and n is the number of events passing all the cuts. The $\frac{\delta\epsilon}{\epsilon}$ for arbitrary values of $m_{\tilde{\chi}_1^\pm}$ and ΔM is estimated by interpolation. The statistics and interpolation errors are typically 3–10 %.

5.7.3 Modeling of the cut variables

The modeling of the cut variables is estimated by comparing the efficiencies when each cut variable is shifted by a possible error. This error in corresponding distribution is determined by studying the differences between the Monte Carlo and data collected around the Z^0 resonance in 1999 and 2000. The systematic errors on the expected number of background events and signal events are summarized in Table 5.5 and Table 5.6, respectively.

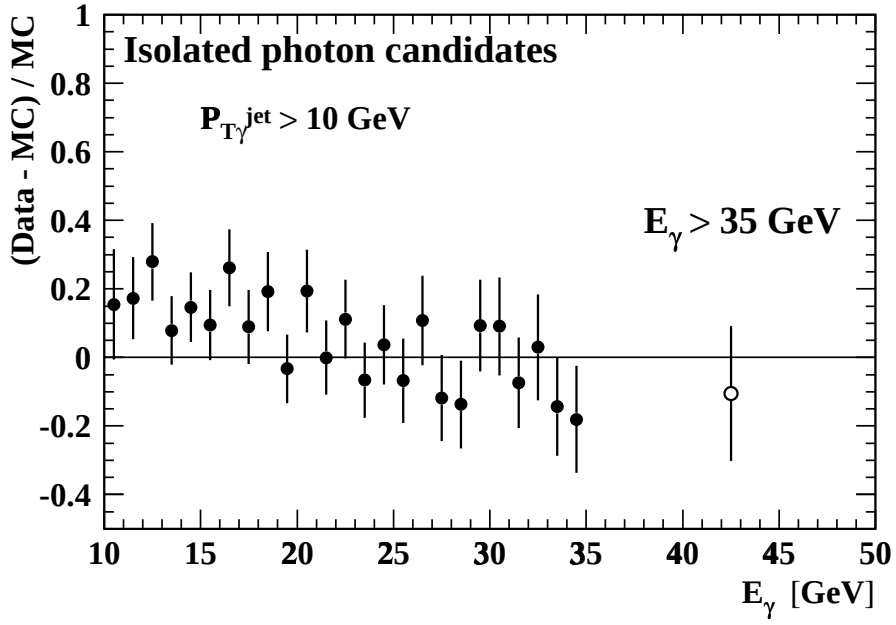

Figure 5.21: *The difference between the real data and the Monte Carlo simulation on the number of photons identified as isolated photon.*

	Analysis A	Analysis B1	Other Analyses
Acoplanarity angle	3.0 %	3.3 %	3.9 %
Visible energy	2.8 %	4.9 %	6.2 %
Photon energy	4.0 %	3.2 %	5.8 %

Table 5.5: *Systematic uncertainties on the modeling of each cut variable for simulated background Monte Carlo events.*

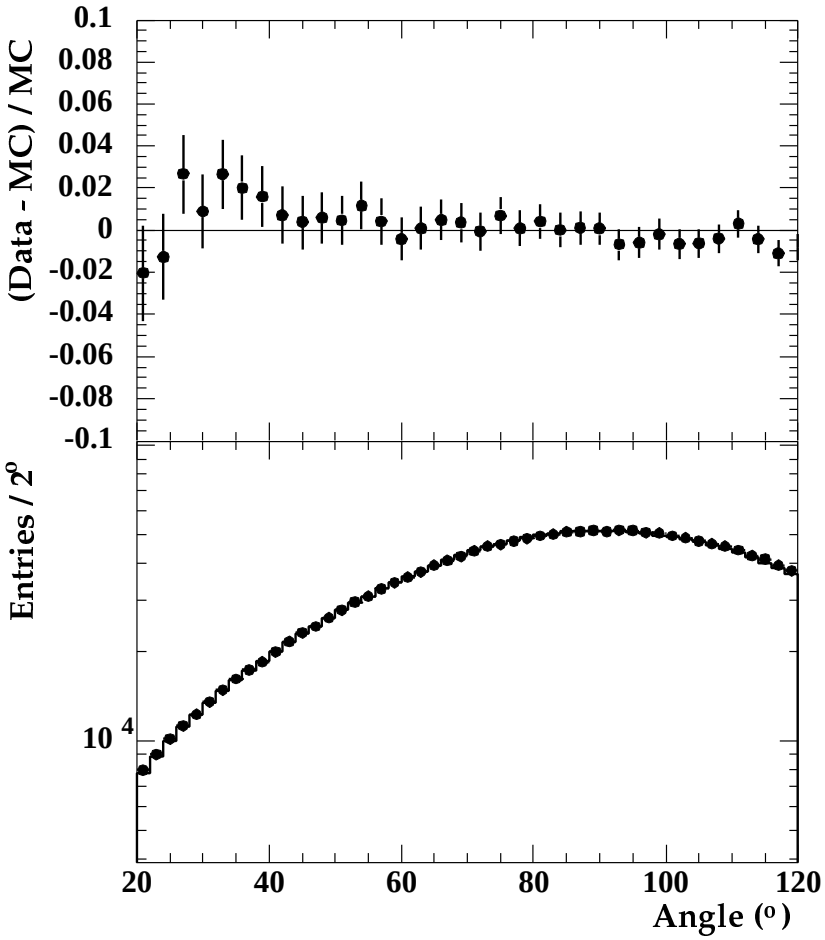

Figure 5.22: The number of photons with $E_{15} < 2$ GeV as a function of the angle between the cone center axis and the nearest jet for data (dot with error bar) and Monte Carlo simulation (open histogram). The upper plot shows the difference between the real data and the Monte Carlo simulation.

	Analysis A	Analysis B1	Other Analyses
Acoplanarity angle	1.9 %	1.9 %	3.4 %
Visible energy	negligible	negligible	2.8 %
Photon energy	negligible	0.6 %	2.3 %

Table 5.6: *Systematic uncertainties on the modeling of each cut variable for simulated signal Monte Carlo events.*

5.8 Limits on the production cross-sections

Since no significant signal has been found, these results can be translated to limits on the production cross-sections of $\widetilde{\chi}_1^+\widetilde{\chi}_1^-$, $\widetilde{\chi}_1^0\widetilde{\chi}_2^0$ and $\widetilde{\ell}_1^+\widetilde{\ell}_1^-$. Model independent upper limits are obtained at 95 % C.L. for the production cross-sections. This is done first for $\widetilde{\chi}_1^+\widetilde{\chi}_1^-$ assuming the decay mode $\widetilde{\chi}_1^\pm \to \widetilde{\chi}_1^0 \mathrm{W}^{(*)\pm}$. The upper limits are determined from the observed numbers of events, the signal detection efficiencies and their uncertainties, and the numbers of expected background events and their uncertainties. This set of parameters, necessary to set the cross-section upper limit, are calculated at each energy bin for each analysis category. To obtain this limit at a given ($m_{\widetilde{\chi}_1^+}$, $m_{\widetilde{\chi}_1^0}$) , ($m_{\widetilde{\chi}_2^0}$, $m_{\widetilde{\chi}_2^0}$) or ($m_{\widetilde{\ell}_1^+}$, $m_{\widetilde{\ell}_1^-}$) point, the independent analyses are combined using the likelihood ratio method [38]. The combinations are depending on a production process and ΔM, and they are summarized in Table 5.7. This method combines the independent analyses by assigning greater weight to the analysis which is expected to have greater sensitivity.

Contours of the 95 % C.L. upper limits for the $\widetilde{\chi}_1^+\widetilde{\chi}_1^-$ cross-sections are shown in Figure 5.23 assuming $\widetilde{\chi}_1^\pm \to \widetilde{\chi}_1^0 \mathrm{W}^{(*)\pm}$ with 100 % branching fraction followed by the prompt decays $\widetilde{\chi}_1^0 \to \gamma\widetilde{\mathrm{G}}$. The Standard Model branching fractions are used for the $\mathrm{W}^{(*)}$ decay. Although these limits do not depend on the details of Supersymmetry models considered, a "typical" field content of the gauginos is assumed, leading to particular production angular distributions that are subsequently used in estimating detection efficiencies. The variation of the efficiency is found to be less than 5 %.

Similar contours of the upper limits for the $\widetilde{\chi}_1^0\widetilde{\chi}_2^0$ cross-section and $\widetilde{\tau}_1^+\widetilde{\tau}_1^-$ cross-section are shown in Figure 5.24 and Figure 5.25, respectively. In either case, $\widetilde{\chi}_1^0$ is assumed to decay into $\gamma\widetilde{\mathrm{G}}$ immediately. For $\widetilde{\chi}_1^0\widetilde{\chi}_2^0$ production, it is also assumed that $\widetilde{\chi}_2^0$ decays into $\widetilde{\chi}_1^0 \mathrm{Z}^{0(*)}$ with 100 % branching fraction.

Production process	small ΔM	medium ΔM	large ΔM
$\widetilde{\ell}_1^+\widetilde{\ell}_1^-$	A $3 \le \Delta M \le m_{\widetilde{\ell}_1^+}$		
$\widetilde{\chi}_1^+\widetilde{\chi}_1^-$	A+B1 3 GeV $\le \Delta M \le$ 20 GeV	A+B2C+C1 20 GeV $< \Delta M \le m_{\widetilde{\chi}_1^+}$ - 30 GeV	A+B3C+C2 $m_{\widetilde{\chi}_1^+}$ - 30 GeV $< \Delta M \le m_{\widetilde{\chi}_1^+}$
$\widetilde{\chi}_1^0\widetilde{\chi}_2^0$	A+B1 3 GeV $\le \Delta M \le$ 40 GeV	A+B2N 40 GeV $< \Delta M \le$ 110 GeV	A+B3N 110 GeV $< \Delta M \le$ 180–190 GeV

Table 5.7: *Combinations at calculating upper limits on production cross-sections. For $\widetilde{\chi}_1^0\widetilde{\chi}_2^0$, the maximum value of ΔM depends on the cms energy. The definition of small, medium and large is different in $\widetilde{\chi}_1^+\widetilde{\chi}_1^-$ and $\widetilde{\chi}_1^0\widetilde{\chi}_2^0$.*

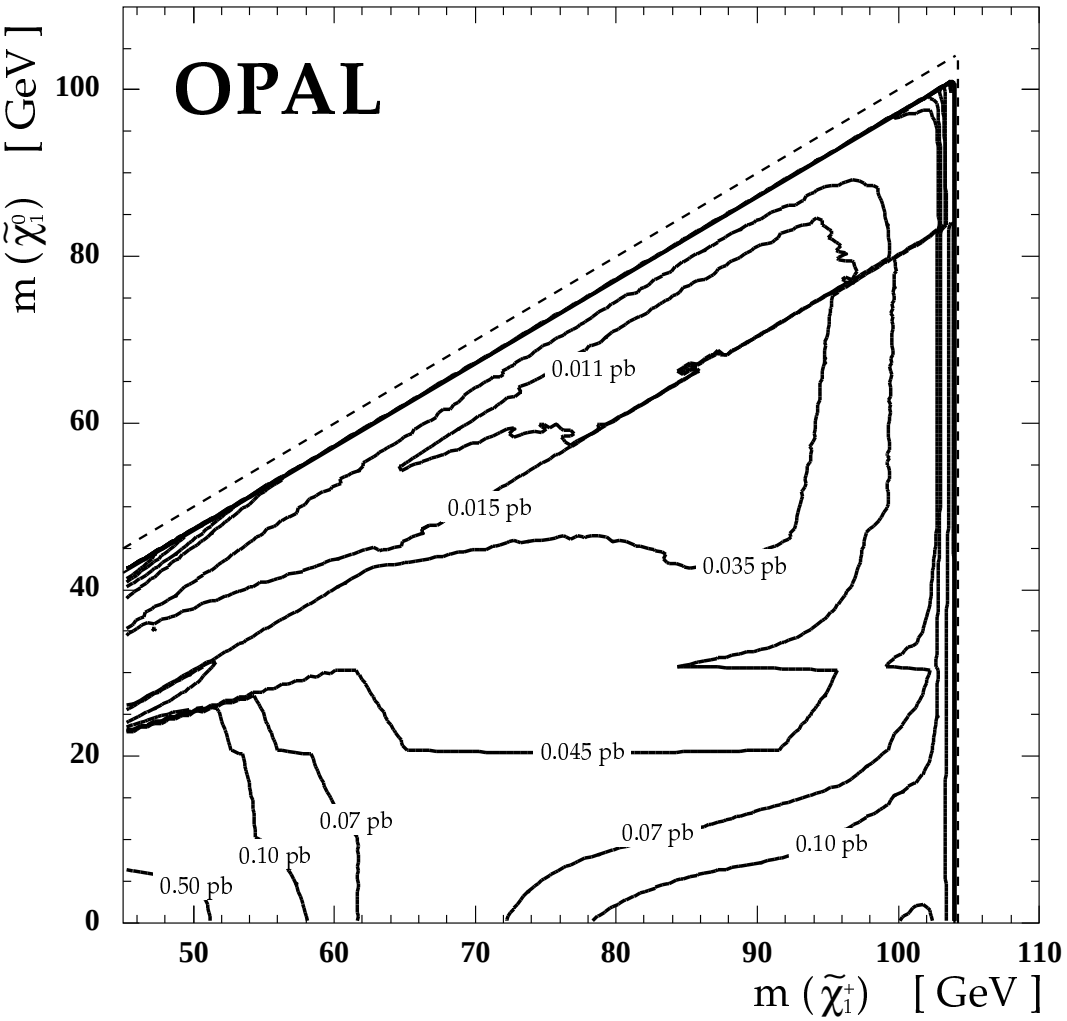

Figure 5.23: *Limits at the 95 % C.L. for the production cross-section of* $e^+e^- \to \tilde{\chi}_1^+\tilde{\chi}_1^-$ *at* $\sqrt{s}$ *= 208.0 GeV are shown, assuming the decays* $\tilde{\chi}_2^0 \to \tilde{\chi}_1^0 W^{\pm(*)}$ *followed by the prompt decays* $\tilde{\chi}_1^0 \to \gamma\tilde{G}$*. The dashed line indicates the kinematic limit.*

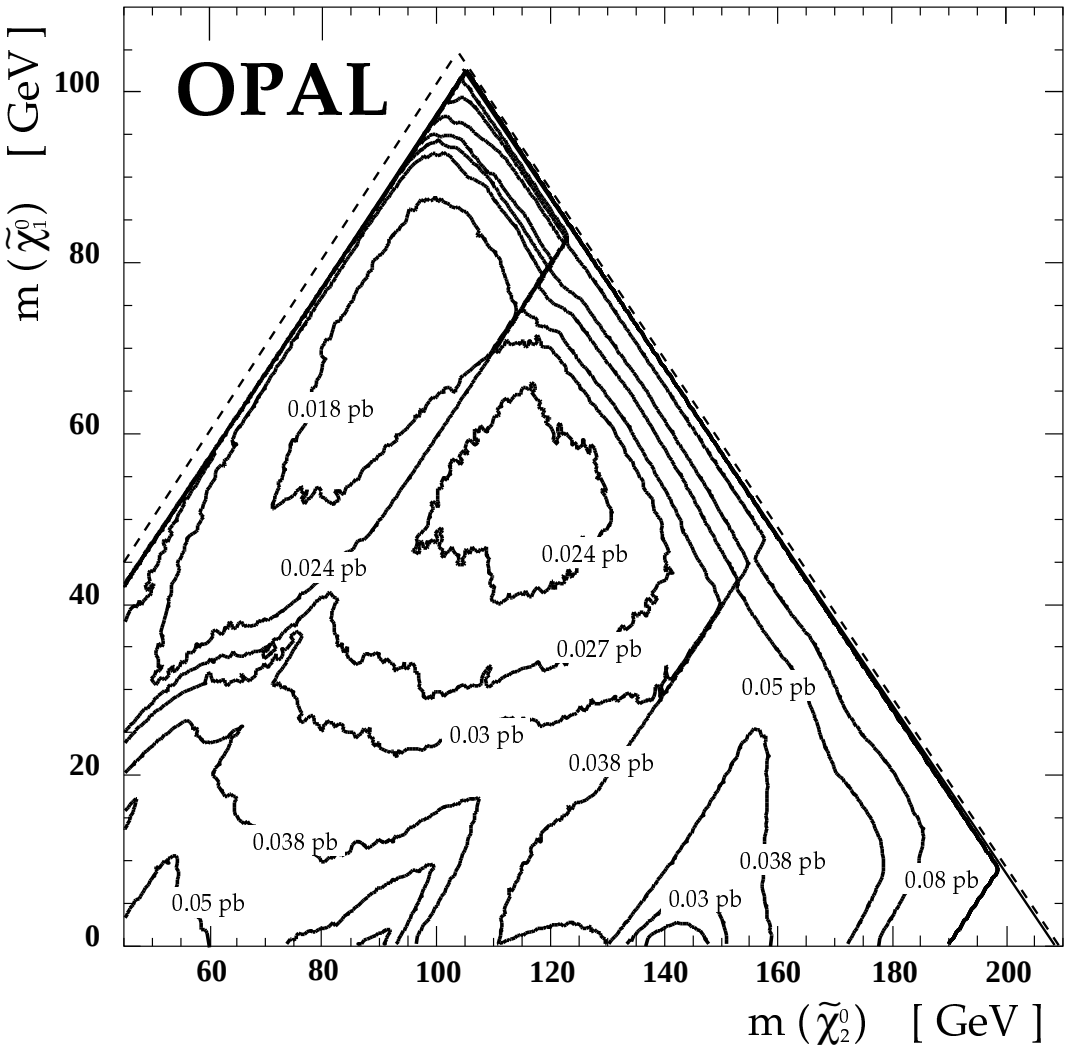

Figure 5.24: *Limits at the 95% C.L. for the production cross-section of* $e^+e^- \to \tilde{\chi}_1^0\tilde{\chi}_2^0$ *at* $\sqrt{s}$ *= 208.0 GeV are shown, assuming the decays* $\tilde{\chi}_2^0 \to \tilde{\chi}_1^0 Z^{0(*)}$ *followed by the prompt decays* $\tilde{\chi}_1^0 \to \gamma\tilde{G}$*. The dashed line indicates the kinematic limit.*

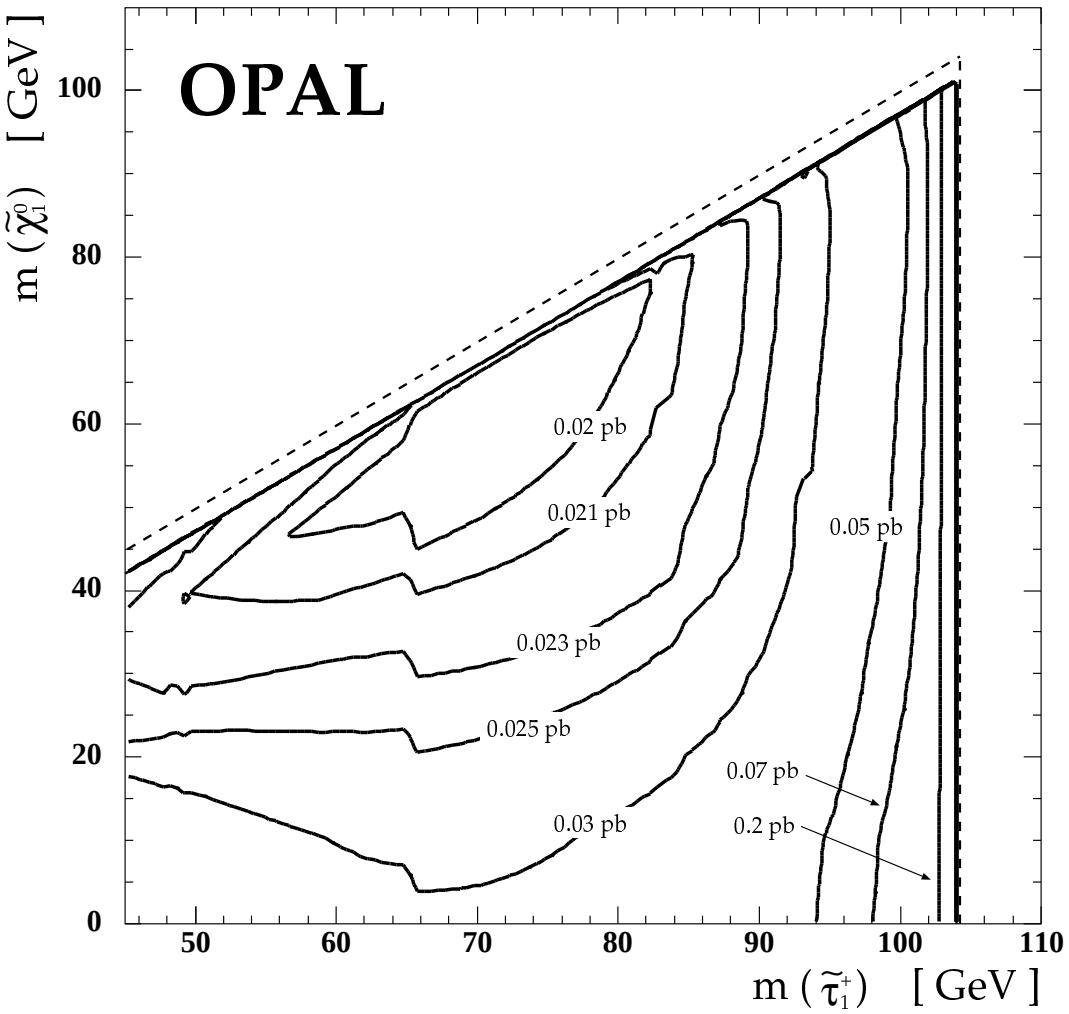

Figure 5.25: *Limits at the 95% C.L. for the production cross-section of* $e^+e^- \to \tilde{\tau}_1^+\tilde{\tau}_1^-$ *at* $\sqrt{s}$ *= 208.0 GeV are shown, assuming the decays* $\tilde{\tau}_1^\pm \to \tau^\pm\tilde{\chi}_1^0$ *followed by the prompt decays* $\tilde{\chi}_1^0 \to \gamma\tilde{G}$*. The dashed line indicates the kinematic limit.*

Chapter 6

Interpretations in the minimal GMSB models

In this chapter, interpretations with the minimal GMSB models are given based on the experimental results. The other results also should be combined to obtain the best limits on the model parameters. Unfortunately, there are many missing results at 192–209 GeV. In this section, interpretations are performed with the some old results obtained at cms energy of 189 GeV.

6.1 The minimal Gauge-Mediated Supersymmetry Breaking model

The minimal Gauge-Mediated Supersymmetry Breaking models (MGM) are the simplest phenomenological GMSB models. Any minimal model is specified in terms of six parameters

$$\Lambda\ ,\ N_m\ ,\ M\ ,\ \tan\beta\ ,\ \mathrm{sgn}(\mu)\ ,\ C_{\mathrm{grav}}\ , \tag{6.1}$$

defined in section 2.1.

The phenomenological meaning and theoretical bounds of the MGM parameters can be summarized as follows:

- Λ : The most important parameter is Λ, which sets the scale of the SUSY breaking in the observable sector. Supersymmetric particle masses are typically smaller by a one-loop factor than Λ, with coefficients completely determined by the particle gauge quantum numbers. The parameter Λ should be larger than several TeV so that Higgs boson has a correct vacuum expectation value.
- M : The messenger scale M affects on supersymmetric masses logarithmically from their renormalized group evolution. The M should be larger than Λ, and well below the M_{GUT} to guarantee flavor-invariant supersymmetry breaking mass terms.
- N_m : N_m is the messenger index (see section 2.1). The maximum number of N_m can be bounded by requiring that the gauge interactions remain perturbative up to the GUT scale, although this bound depends on M; for M = 100 TeV, $N_m \leq 5$, while for M = 10^{10} TeV, $N_m \leq 10$.
- $\tan\beta$: The ratio of the Higgs vacuum expectation values, $\tan\beta$, affects on the mixing angles between left- and right-handed sparticles, especially the third generation sparticles. The upper value is limited by a positiveness of mass squared of the lightest stau.
- sgn(μ) : The size of μ can be computed from the condition of the correct electroweak breaking;

$$\mu^2 = -\frac{m_{\mathrm{Z}^0}^2}{2} + \frac{1}{\tan^2\beta - 1}(m_{H_1}^2 - \tan^2\beta m_{H_2}^2)\,, \tag{6.2}$$

and the sign of μ is still a free parameter. The parameter μ^2 is roughly (electroweak scale)^2.

- $C_{\rm grav}$: $C_{\rm grav}$ is the ratio of the intrinsic SUSY breaking parameter (F_0) to the messenger sector SUSY breaking parameters (F). It controls the coupling to the gravitino.

The parameter $C_{\rm grav}$ is an independent parameter of the others, and it is set to be small enough so that the NLSP decays into the LSP promptly. In the MGM with prompt decay NLSP, the number of free parameters is reduced to five.

Experimental results described in the next section can be interpreted within the framework of the MGM.

6.2 GMSB signatures

Assuming the MGM with prompt decaying NLSP, the topologies expected in GMSB models are characterized by the nature of the NLSP. Generally, following three situations can be considered[1];

- neutralino NLSP ,
- slepton co-NLSP ($m_{\tilde{\tau}} \sim m_{\tilde{e}} \sim m_{\tilde{\mu}}$) , and
- stau NLSP ($m_{\tilde{\tau}} < m_{\tilde{e}}, m_{\tilde{\mu}}$) .

Production and decay processes used in the interpretation are summarized in Table 6.1. In the following paragraphs, each topology is presented briefly.

Search for $\widetilde{\chi}^0_1\widetilde{\chi}^0_1$ ($\widetilde{\chi}^0_1$ NLSP)

A pair of the lightest neutralinos is produced through s-channel exchange of virtual Z^0 and t-channel exchange of selectron, which are constructive to each other. The parameter μ, extracted from the electroweak breaking condition, typically turns out to be larger than m_{Z^0}: that is, the lightest neutralino is almost Bino-like. The contribution of t-channel exchange is larger than s-channel because the trilinear coupling of gauge boson is not allowed. In case of $\widetilde{\chi}^0_1$ NLSP, $\widetilde{\chi}^0_1$ decays into $\gamma\widetilde{\mathrm{G}}$ with 100 % branching ratio if R-parity is conserved;

$$\mathrm{e}^+\mathrm{e}^- \to \widetilde{\chi}^0_1\widetilde{\chi}^0_1 \to \gamma\widetilde{G}\gamma\widetilde{G}\,.$$

One can observe acoplanar photons with significant missing energy in the final state [35].

Search for $\widetilde{\chi}^0_1\widetilde{\chi}^0_2$ ($\widetilde{\chi}^0_1$ NLSP)

The second lightest neutralino $\widetilde{\chi}^0_2$ can be produced through an s-channel Z^0, or by t-channel selectron exchange. The cross-section for $\widetilde{\chi}^0_1\widetilde{\chi}^0_2$ production is much lower than that of $\widetilde{\chi}^+_1\widetilde{\chi}^-_1$ production although $\widetilde{\chi}^0_2$ and $\widetilde{\chi}^\pm_1$ are almost degenerate in the MGM prediction. The $\widetilde{\chi}^0_2$ will decay into $\widetilde{\chi}^0_1\nu\bar{\nu}$, $\widetilde{\chi}^0_1\ell^+\ell^-$ or $\widetilde{\chi}^0_1\mathrm{q}\bar{\mathrm{q}}$ followed by $\widetilde{\chi}^0_1 \to \gamma\widetilde{\mathrm{G}}$;

$$\mathrm{e}^+\mathrm{e}^- \to \widetilde{\chi}^0_1\widetilde{\chi}^0_2 \to \widetilde{\chi}^0_1\widetilde{\chi}^0_1\mathrm{Z}^0 \to \gamma\widetilde{G}\gamma\widetilde{G} + \mathrm{q}\bar{\mathrm{q}} \text{ or } \ell^+\ell^-\,.$$

The direct decay process $\widetilde{\chi}^0_2 \to \widetilde{\mathrm{G}}\gamma$ is also possible but this contribution is small. The detail of this analysis is described in Ref. [37].

[1] In some restricted parameter regions, "slepton and neutralino co-NLSP" case ($m_{\tilde{e}} \sim m_{\tilde{\mu}} \sim m_{\tilde{\chi}} \sim m_{\tilde{\tau}}$) and $m_{\tilde{e}}, m_{\tilde{\mu}} > m_{\tilde{\chi}} > m_{\tilde{\tau}}$ case are also possible.

Search for $\widetilde{\chi}_1^0\widetilde{\chi}_1^0$ ($\widetilde{\ell}_1^{\pm}$ NLSP)

In case of slepton NLSP, the neutralino pair production may result in the 4-lepton with missing energy signature;

$$\mathrm{e}^+\mathrm{e}^- \to \widetilde{\chi}_1^0\widetilde{\chi}_1^0 \to \ell^+\widetilde{\ell}^-\ell^-\widetilde{\ell}^+ \to \ell^+\ell^-\ell^-\ell^+\widetilde{G}\widetilde{G}\,.$$

The decay mode of $\widetilde{\chi}_1^0 \to \widetilde{\ell}^{\pm}\ell^{\mp}$ competes with $\widetilde{\chi}_1^0 \to \gamma\widetilde{\mathrm{G}}$. The relative strength depends on the gravitino mass, the mass difference between $\widetilde{\chi}_1^0$ and $\widetilde{\ell}$, $\widetilde{\chi}_1^0$ parameters, and $\tan\beta$. Generally, this process can dominate over the decay process $\widetilde{\chi}_1^0 \to \gamma\widetilde{\mathrm{G}}$ unless $m_{\widetilde{\chi}_1^0} - m_{\widetilde{\ell}} < m_{\ell}$.

If $m_{\widetilde{e}} \sim m_{\widetilde{\mu}} \sim m_{\widetilde{\tau}}$, called 'slepton co-NLSP', selectron and smuon channels are more useful to exclude a parameter space than stau channel because the analyses of former channels usually have a better sensitivity. As $\tan\beta$ becomes large, $\widetilde{\tau}_1^{\pm}$ is lighter than $\widetilde{e}_1^{\pm}$ and $\widetilde{\mu}_1^{\pm}$, and stau channel can give more severe restriction on theoretical parameters than other slepton channels [37].

Search for charginos ($\widetilde{\chi}_1^0$ NLSP)

If charginos exist and are sufficiently light, they will be pair-produced through virtual γ or Z^0 boson in the s-channel. There is an additional production process through electron-sneutrino, $\widetilde{\nu}_e$ exchange in the t-channel. The production cross-section is large unless the sneutrino is light, in which case the cross-section is reduced by destructive interference between them. The details of the chargino decay depend on the parameters of the mixing and the masses of the sfermions. The lightest chargino $\widetilde{\chi}_1^+$ can decay into $\widetilde{\chi}_1^0\ell^+\nu$, or $\widetilde{\chi}_1^0\mathrm{q}\bar{\mathrm{q}}'$, via $\mathrm{W}^{(*)}$, slepton $\widetilde{\ell}$, sneutrino $\tilde{\nu}$, squark $\tilde{q}$ or $\mathrm{W}^+\widetilde{\mathrm{G}}$. In much of the MGM parameter space $\widetilde{\chi}_1^+$ decays via a virtual W are dominant;

$$\mathrm{e}^+\mathrm{e}^- \to \widetilde{\chi}_1^0\widetilde{\chi}_1^0\mathrm{W}^+\mathrm{W}^- \to \gamma\widetilde{G}\gamma\widetilde{G} + q\bar{q}q\bar{q} \text{ or } q\bar{q}\ell\bar{\nu}_{\ell} \text{ or } \ell^+\nu_{\ell}\ell^-\bar{\nu}_{\ell}\,.$$

Here, it is assumed that $\widetilde{\chi}_1^+$ decays into $\widetilde{\chi}_1^0\mathrm{W}^{+(*)}$ by 100 % branching ratio [37].

Search for sleptons ($\widetilde{\ell}_1^{\pm}$ NLSP)

The lighter smuon $\widetilde{\mu}_1^+$ and stau $\widetilde{\tau}_1^+$ are pair-produced through s-channel exchange of virtual γ and Z^0. These cross-sections are almost determined by superparticle masses and does not depend on the mixing angles between left- and right-handed states very much. On the others hand, neutralino-exchange in the t-channel can contribute to the production for the selectrons production. The cross-section is not uniquely determined by mass of selectron and the mixing angle, but depends also on the neutralino parameters M_2, μ and $\tan\beta$. In case of slepton NLSP, the experimental signature is acoplanar leptons with significant missing energy;

$$\mathrm{e}^+\mathrm{e}^- \to \widetilde{\ell}^+\widetilde{\ell}^+ \to \ell^+\ell^-\widetilde{G}\widetilde{G}\,.$$

The topological analysis for acoplanar leptons with missing energy is reported in Ref. [36].

Search for sleptons ($\widetilde{\chi}_1^0$ NLSP)

In case of the lightest neutralino NLSP, $\widetilde{\ell}_1^+$ decays into $\widetilde{\chi}_1^0\ell^+$ followed by $\widetilde{\chi}_1^0 \to \gamma\widetilde{\mathrm{G}}$. The experimental signature is photons plus acoplanar leptons with missing energy;

$$\mathrm{e}^+\mathrm{e}^- \to \widetilde{\ell}_1^+\widetilde{\ell}_1^- \to \widetilde{\chi}_1^0\ell^+\widetilde{\chi}_1^0\ell^- \to \gamma\widetilde{G}\gamma\widetilde{G} + \ell^+\ell^-\,.$$

The analysis is reported in Ref. [37].

Search for sleptons ($\widetilde{\tau}_1^0$ NLSP)

If the lightest neutralino is too heavy to be produced and the lightest stau is significantly lighter than other sleptons, the 6-lepton final state with missing energy may contribute via

$$\mathrm{e}^+\mathrm{e}^- \to \widetilde{\ell}^+\widetilde{\ell}^- \to \ell^+\widetilde{\tau}\tau\,\ell^-\widetilde{\tau}\tau \to \ell^+\tau^+\tau^-\widetilde{G}\,\ell^-\tau^+\tau^-\widetilde{G} \quad (\widetilde{\ell}^+ = \widetilde{e}^+, \widetilde{\mu}^+)\,.$$

For small $\tan\beta$, a mass difference between stau and other sleptons is small, and it is difficult to detect electrons(muons), which arise from selectron(smuon) decays. The detail of this analysis is presented in Ref. [37].

NLSP	Production	Decay mode	Expected topology
$\widetilde{\chi}_1^0$	$\mathrm{e}^+\mathrm{e}^- \to \widetilde{\chi}_1^0\widetilde{\chi}_1^0$	$\widetilde{\chi}_1^0 \to \gamma\widetilde{\mathrm{G}}$	Acoplanar photons
	$\mathrm{e}^+\mathrm{e}^- \to \widetilde{\chi}_1^0\widetilde{\chi}_2^0$	$\widetilde{\chi}_2^0 \to \widetilde{\chi}_1^0\mathrm{Z}^0$	Acoplanar photons + jets or leptons
	$\mathrm{e}^+\mathrm{e}^- \to \widetilde{\chi}_1^+\widetilde{\chi}_1^-$	$\widetilde{\chi}_\pm^0 \to \widetilde{\chi}_1^0\mathrm{W}^\pm$	Acoplanar photons + jets and/or lepton(s)
	$\mathrm{e}^+\mathrm{e}^- \to \ell^+\ell^-$	$\widetilde{\ell}^\pm \to \widetilde{\chi}_1^0\ell^\pm$	Acoplanar photons + leptons
$\widetilde{\ell}_R$	$\mathrm{e}^+\mathrm{e}^- \to \widetilde{\ell}_R^+\widetilde{\ell}_R^-$	$\widetilde{\ell}_R^\pm \to \ell^\pm\widetilde{\mathrm{G}}$	Acoplanar leptons
co-NLSP	$\mathrm{e}^+\mathrm{e}^- \to \widetilde{\chi}_1^0\widetilde{\chi}_1^0$	$\widetilde{\chi}_1^0 \to \widetilde{\ell}_R^\pm\ell^\mp$	four leptons
$\widetilde{\tau}_1^\pm$	$\mathrm{e}^+\mathrm{e}^- \to \widetilde{e}_R^+\widetilde{e}_R^-(\widetilde{\mu}_R^+\widetilde{\mu}_R^-)$	$\widetilde{e}_R^\pm \to e^\pm\widetilde{\tau}_1^\pm\tau^\mp$	Six leptons ($\tau^+\tau^-\tau^+\tau^-e^+e^-(\mu^+\mu^-)$)

Table 6.1: *Production and decay process with GMSB are summarized. Six lepton process is special to the stau NLSP case, but processes listed in a column, the slepton co-NLSP case, are dominant in the stau NLSP case.*

6.3 Methodology

In the GMSB models, Eqs.(2.8, 2.9) serve as boundary conditions at the messenger scale (M-scale) for renormalization group evolution of SUSY quantities from the M-scale down to m_{Z^0} scale. In order to obtain gaugino and scalar particle masses at the M-scale, we need the gauge and Yukawa couplings at the M-scale. Therefore, at the beginning, we evolve the gauge and Yukawa couplings up to the M-scale. For gauge couplings at m_{Z^0} scale:

$$\begin{aligned}
\alpha_1 &= \frac{\alpha_{\mathrm{em}}(m_{\mathrm{Z}^0})}{4\pi\cos^2\theta_W}\,,\\
\alpha_2 &= \frac{\alpha_{\mathrm{em}}(m_{\mathrm{Z}^0})}{4\pi\sin^2\theta_W}\,,\\
\alpha_3 &= \frac{7\alpha_{\mathrm{em}}(m_{\mathrm{Z}^0})}{12\pi(5\sin^2\theta_W - 1)}\,,
\end{aligned}$$

where $\alpha_{\mathrm{em}}(m_{\mathrm{Z}^0}) = 1/127.89$ and the α_3 is calculated from the GUT condition. For Yukawa couplings, we make use of simple relation between quarks and leptons mass matrices and Yukawa matrices:

$$\begin{aligned}
Y_U &= \frac{\sqrt{2}}{4\pi\upsilon\sin\beta}\begin{pmatrix} m_u & 0 & 0\\ 0 & m_c & 0\\ 0 & 0 & m_t\end{pmatrix},\\
Y_D &= \frac{\sqrt{2}}{4\pi\upsilon\cos\beta}\begin{pmatrix} m_d & 0 & 0\\ 0 & m_s & 0\\ 0 & 0 & m_b\end{pmatrix},\\
Y_E &= \frac{\sqrt{2}}{4\pi\upsilon\cos\beta}\begin{pmatrix} m_e & 0 & 0\\ 0 & m_\mu & 0\\ 0 & 0 & m_\tau\end{pmatrix}.
\end{aligned}$$

In above formulae, $v = \sqrt{v_u^2 + v_d^2}$ = 246 GeV, where v_u and v_d are up- and down-type Higgs VEVs, respectively.

After setting up those initial conditions, we evolve the gauge and Yukawa couplings up to the M-scale using the Standard Model renormalization group equations (RGE's) below SUSY mass threshold. At the first step, it is set to be 1 TeV, and MSSM RGE's is used above that scale:

$$\frac{d\alpha_i}{dt} = b_i \alpha_i^2 \,,$$

where $t = \log Q$, and $(b_1, b_2, b_3) = (41/3, -19/3, -14)$ for the Standard Model RGE's, while $(b_1, b_2, b_3) = (22, 2, -6)$ for SUSY RGE's.

This procedure allows us to calculate boundary conditions for gaugino and scalar masses at the M scale. After that, we make parameters run down to the m_{Z^0} scale. During this evolution, the threshold corrections of SUSY particles are considered with step functions. The squared mass of up-type scalar Higgs is driven to negative due to a large top Yukawa coupling contribution, which causes the radiative electroweak symmetry breaking. At m_{Z^0} scale, the gaugino and scalar masses are computed based on mass eigenstates (see Appendix A).

The values of μ and $B\mu$ are obtained by minimizing the tree-level Higgs potential;

$$V_0 = m_1^2 |H_d^0|^2 + m_2^2 |H_u^0|^2 + m_3^2 (\epsilon_{ij} H_d^{0i} H_u^{0j} + h.c.) + \frac{g_1^2 + g_2^2}{8} (|H_d^0|^2 - |H_u^0|^2)^2 + \frac{1}{2} |H_d^{0i*} H_u^{0i*}|^2 \,, \quad (6.3)$$

where $m_{1,2}^2 \equiv m_{H_{d,u}}^2 + \mu^2$, $m_3^2 \equiv B\mu$, and phases of fields are chosen so that m_3^2 is negative. Having those quantities, we can calculate the low-energy mass spectrum of the model, which is necessary in order to find the proper values of μ and $B\mu$ coming from the full one-loop Higgs effective potential. Thus, in the next step, we perform the RGE evolution of all the parameters up to the M-scale, set the initial conditions for gauginos and scalars once again, and then evolve everything back to m_{Z^0} scale. Next, we perform the RGE evolution up to the scale $Q = \sqrt{m_{\tilde{t}_1} m_{\tilde{t}_2}}$, which is the best scale for minimizing the full one-loop Higgs scalar potential:

$$|\mu|^2 = -\frac{m_{Z^0}^2}{2} + \frac{m_{H_d}^2 + m_{H_u}^2 \tan^2\beta + \Delta T_1 / v}{\tan^2\beta - 1} \,, \quad (6.4)$$

$$-B\mu = (2\mu^2 + m_{H_u}^2 + m_{H_d}^2) \sin\beta \cos\beta + \Delta T_2 / v \,. \quad (6.5)$$

where one-loop contributions of T_1 and T_2 are given in Ref. [51]. In order for the Higgs bosons to acquire the vacuum expectation values and have the physical masses,

$$(B\mu)^2 > (|\mu|^2 + m_{H_d}^2)(|\mu|^2 + m_{H_u}^2) \,, \quad (6.6)$$

$$2B\mu < 2|\mu|^2 + m_{H_u}^2 + m_{H_d}^2 \,, \quad (6.7)$$

are required. After the radiatively corrected values of $B\mu$ and μ are obtained, we evolve all the quantities down to m_{Z^0} scale to find the mass eigenstates of MSSM particles once again. We repeat this procedure a few times to have a stable solution for $B\mu$ and μ.

All necessary parameters are obtained at m_{Z^0} scale for computing production cross-sections and decay widths. The computation of these quantities is performed using SUSYGEN [49]. The investigated parameter space is summarized in Table 6.2.

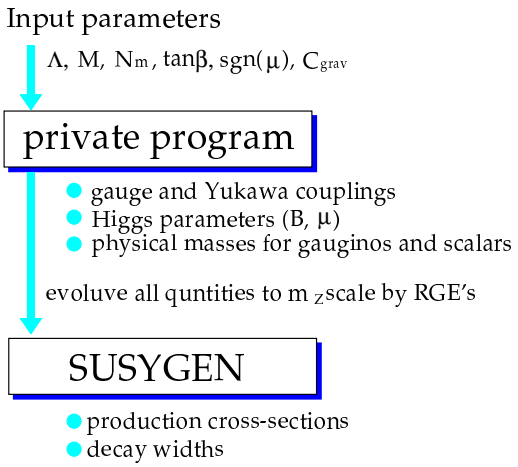

Figure 6.1: *An Outline of the method of the interpretation with the MGM.*

Parameter	Lower value	Upper value
Λ	10.0 TeV	200.0 TeV
$\tan\beta$	2.0	50.0
M	1.01 Λ, 250 TeV, 10^6 TeV	
sing of μ	-	+

Table 6.2: *The investigated parameter space of the MGM.*

6.4 Lower limit on Λ

In the context of the MGM, it is relevant to put a lower limit on the parameter Λ which determines a mass scale of SUSY particles. As the relation between the SUSY particles and Λ depends on N_m, a limit on Λ is provided for each N_m. The parameter $\tan\beta$ is also important because it determines the mass relation among sleptons and the lightest neutralino, namely the NLSP type and decay modes.

In Figure 6.2 exclusion limits on the Λ versus $\tan\beta$ plane are shown for differnet values of N_m. Theoretical inaccessible region is restricted by unphysical sparticle or Higgs masses ($\tilde{m}^2 < 0$) and the incorrect electroweak symmetry breaking (Eqs.(6.6, 6.7)). Three lines in each plot show excluded region with different M. As M becomes smaller, sfermions become lighter and gauginos become heavier due to the functions $f(x), g(x)$ (see Eqs.(2.11, 2.13)). The result from acoplanar photon search ($\tilde{\chi}_1^0\tilde{\chi}_1^0 \to \gamma\tilde{\mathrm{G}}\gamma\tilde{\mathrm{G}}$) has the largest potential to restrict the parameter space in case of small N_m and small $\tan\beta$. In other region, the constraint from acoplanar tau search ($\tilde{\tau}_1^+\tilde{\tau}_1^- \to \tau^+\tilde{\mathrm{G}}\tau^-\tilde{\mathrm{G}}$) dominates over others. The lower limits on Λ with different N_m are summarized in Table 6.3.

N_m	lower limit on Λ (TeV)
1	48
2	31
3	22
4	19

Table 6.3: *The lower limit on Λ for each N_m in the case of the MGM with prompt decaying NLSP (95 % C.L.).*

6.5 Lower limit on the NLSP masses

The parameter $\tan\beta$ determines the NLSP type and its property. Therefore, results are presented on $\widetilde{\chi}_1^0$ and $\widetilde{\tau}_1^{\pm}$ mass plane for $\tan\beta$ = 2 and $\tan\beta$ = 20. The former case corresponds to "slepton co-NLSP" case while the latter corresponds to "stau NLSP". In the case of $\tan\beta$ = 2, the excluded region is shown in Figure 6.3(a). The "theoretically inaccessible" region indicates that such a mass relation between $\widetilde{\chi}_1^0$ and $\widetilde{\tau}_1^{\pm}$ is not realize within the MGM ($1 \leq N_m \leq 4$). The dominant "exclusion" channels are $\widetilde{\chi}_1^0\widetilde{\chi}_1^0 \to \gamma\widetilde{\mathrm{G}}\gamma\widetilde{\mathrm{G}}$ and $\widetilde{\mu}_R^+\widetilde{\mu}_R^- \to \mu^+\widetilde{\mathrm{G}}\mu^-\widetilde{\mathrm{G}}$. In the case of $\tan\beta$ = 20, the result is shown in Figure 6.3(b). The $\widetilde{\chi}_1^0\widetilde{\chi}_1^0 \to \gamma\widetilde{\mathrm{G}}\gamma\widetilde{\mathrm{G}}$ channel remains powerful, and $\widetilde{\tau}_1^{\pm}$ means that only the $\widetilde{\tau}_1^+\widetilde{\tau}_1^- \to \tau^+\widetilde{\mathrm{G}}\tau^-\widetilde{\mathrm{G}}$ channel contribution is significant. Finally, 95 % C.L. limits can be derived on the NLSP masses, which is summarized in Table 6.4.

$\tan\beta$	$\widetilde{\chi}_1^0$ mass	$\widetilde{e}_R^+, \widetilde{\mu}_R^+$ mass	$\widetilde{\tau}_1^+$ mass
2	85 GeV	83 GeV	
20	76 GeV	83 GeV	69 GeV

Table 6.4: *The 95 % C.L. lower limits on the NLSP masses; (a) for* $\tan\beta$*=2 (slepton co-NLSP case) and (b) for* $\tan\beta$*=20 (stau NLSP case).*

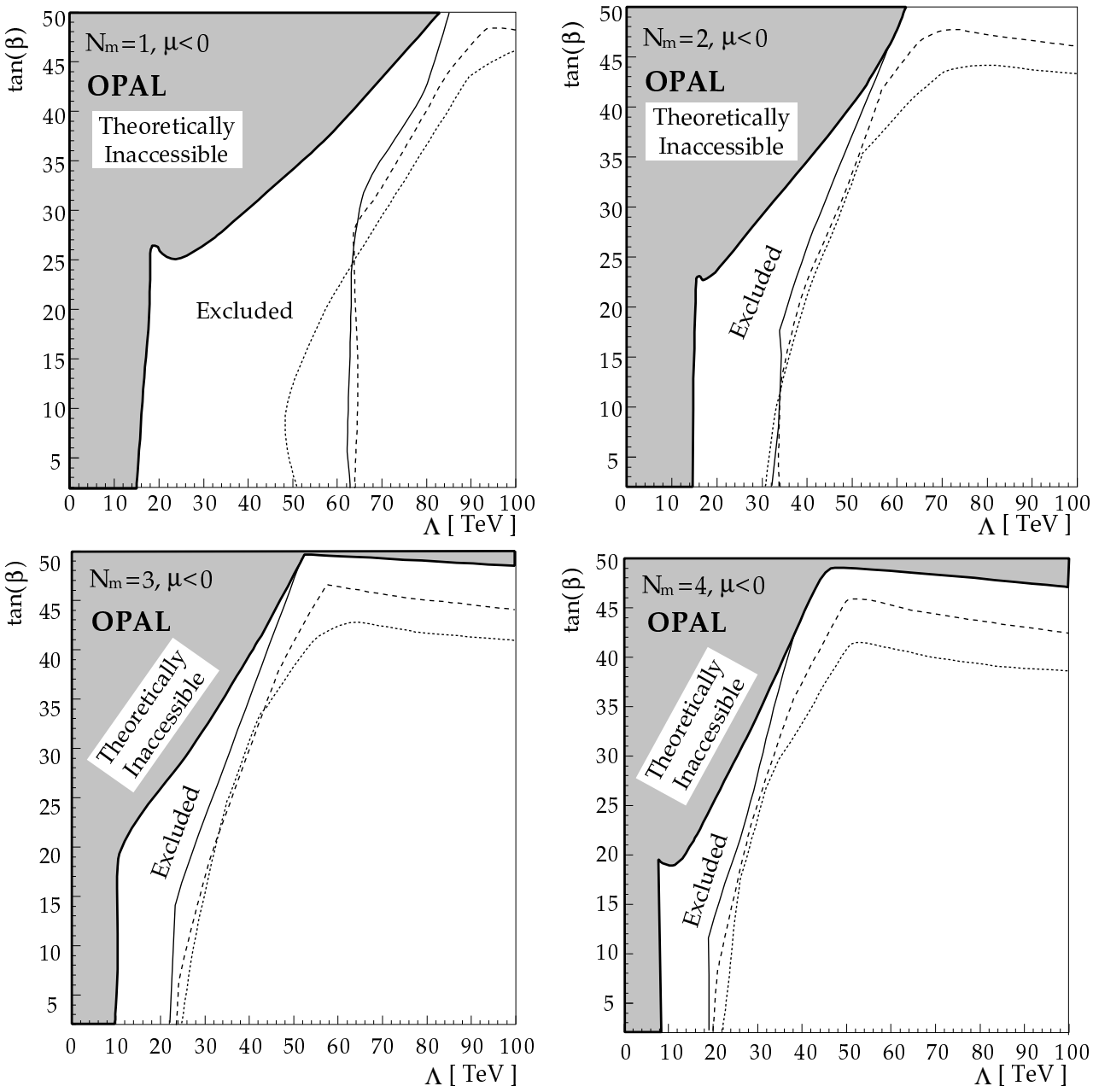

Figure 6.2: *Excluded region by experimental results using data collected at cms energy of 189 GeV for N_m = 1, 2, 3 and 4 and $\mu < 0$. The areas above and to the left of the solid line are excluded for $M = 10^6$ TeV The areas above and to the left of the lines are excluded with different M; $M = 10^6$ (solid line), 250 TeV (dashed line), and 1.01 Λ (dotted line). The shaded regions are theoretically inaccessible for $M = 10^6$ TeV (the inaccessible region is larger for smaller values of M.). The exclusions for $\mu > 0$ are somewhat stronger.*

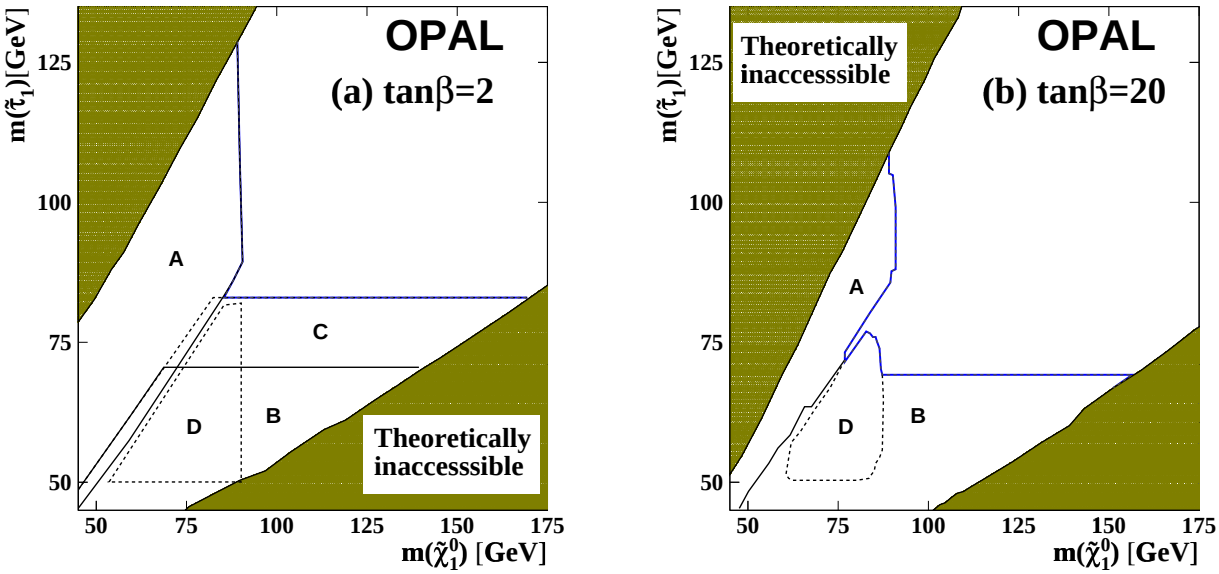

Figure 6.3: *Excluded regions at the 95% C.L. in the $m_{\tilde{\ell}}$ versus $m_{\tilde{\chi}_1^0}$ plane for (a) $\tan\beta$ = 2 (slepton co-NLSP case) and (b) $\tan\beta$ = 20 (stau NLSP case). Also shown are the regions exclusively excluded by (A) $\tilde{\chi}_1^0\tilde{\chi}_1^0 \to \gamma\tilde{\mathrm{G}}\gamma\tilde{\mathrm{G}}$, (B) $\tilde{\tau}^+\tilde{\tau}^- \to \tau^+\tilde{\mathrm{G}}\tau^-\tilde{\mathrm{G}}$, (C) $\tilde{\mu}^+\tilde{\mu}^- \to \mu^+\tilde{\mathrm{G}}\mu^-\tilde{\mathrm{G}}$ and (D) $\tilde{\chi}_1^0\tilde{\chi}_1^0 \to$ 4-lepton final states. The other search channels do not contribute significantly to the exclusion regions in the MGM model. The shaded regions are theoretically inaccessible.*

Chapter 7

Conclusion

In this thesis, the data sample corresponding to an integrated luminosity of 432 pb^{-1} at $\sqrt{s}$ = 192–209 GeV collected with the OPAL detector has been analyzed to search for charginos, neutralinos and sleptons productions predicted by the Gauge-Mediated Supersymmetry Breaking (GMSB) scenarios.

The search consists of analyses designed to look for the following topologies;

(A) photons plus leptons with missing energy,
(B) photons plus jets with missing energy, and
(C) photons plus jets plus lepton with missing energy.

These topologies are special to the GMSB scenarios. To obtain good sensitivity, the analysis is divided into some categories according to the mass difference between the NNLSP and the NLSP. The numbers of observed events are in agreement with the expected numbers from the Standard Model background in any analysis.

At last, an interpretation within the minimal GMSB (MGM) scenario with prompt decaying NLSP, is given based on some LEP2 search results. Comparing experimental upper limits on the production cross-sections with the theoretical production cross-sections, 95 % C.L. lower limits on the Λ can be set. Finally, the lower limits on the NLSP masses are set at 95 % C.L.. These results are restricted to data sample at $\sqrt{s}$=189 GeV with an integrated luminosity of 182 pb^{-1}, and more strict constraints can be set using all LEP2 search results at $\sqrt{s}$=192–209 GeV. The interpretation method, the analysis and its results would be useful for the future collider experiments. I hope that we discover an indication beyond the Standard Model in the near future.

Appendix A

Particle Contents

A.1 Neutralinos and Charginos

There are four new neutral fermions in the MGM which not only receive mass but mix as well. There are the gauge fermion partners of B and W^3 gauge bosons ($\widetilde{B}$ and $\widetilde{W}^3$), and the partners of the Higgs ($\widetilde{H}_1$ and $\widetilde{H}_2$). In the basis;

$$\phi^0 = (\widetilde{B}, \widetilde{W}^3, -\widetilde{H}_1^0 \cos\beta + \widetilde{H}_2^0 \sin\beta, \widetilde{H}_1^0 \sin\beta + \widetilde{H}_2^0 \cos\beta)\,, \tag{A.1}$$

the mass matrix of the neutral gauginos is given by,

$$\mathbf{M}^0 = \begin{pmatrix} M_1 & 0 & m_{\mathrm{Z}^0}\sin\theta_W & 0 \\ 0 & M_2 & -m_{\mathrm{Z}^0}\cos\theta_W & 0 \\ M_{\mathrm{Z}^0}\sin\theta_W & -m_{\mathrm{Z}^0}\cos\theta_W & \mu\mathrm{sin}2\beta & \mu\mathrm{cos}2\beta \\ 0 & 0 & \mu\mathrm{cos}2\beta & -\mu\mathrm{sin}2\beta \end{pmatrix}. \tag{A.2}$$

The physical mass eigenstates, the neutralino ($\widetilde{\chi}_k^0$), are defined by

$$\widetilde{\chi}_k^0 = \mathbf{N}\phi^0\,,$$

where $\mathbf{N}$ is a unitary matrix, which diagonalizes $\mathbf{M}^0$.

The neutralino mass eigenvalues ($m_{\widetilde{\chi}_k^0}$) can be computed by diagonalizing the mass matrix Eq.(A.2) according to

$$m_{\widetilde{\chi}_k^0}\delta_{kl} = N_{km}N_{ln}M^0_{mn}\,.$$

There are two new charged fermionic states which are the partners of the W$^\pm$gauge bosons and the charged Higgs scalars, $H^\pm$, which are the charged gauginos, $\widetilde{W}^\pm$ and charged Higgsino, $\widetilde{H}^\pm$, or collectively charginos. The chargino mass matrix is composed similarly to the neutralino mass matrix. The result for the mass term is

$$-\frac{1}{2}(\widetilde{W}^-, \widetilde{H}^-) \begin{pmatrix} M_2 & \sqrt{2}m_W\sin\beta \\ \sqrt{2}m_W\cos\beta & \mu \end{pmatrix} \begin{pmatrix} \widetilde{W}^+ \\ \widetilde{H}^+ \end{pmatrix} + h.c.\,. \tag{A.3}$$

The result for the mass eigenstates of the two charginos is

$$m^2_{\widetilde{\chi}_1^+}, m^2_{\widetilde{\chi}_2^+} = \frac{1}{2}\left[M_2^2 + \mu^2 + 2m_W^2 \pm \sqrt{(M_2^2+\mu^2+2m_W^2)^2 - 4(\mu M_2 - m_W^2\mathrm{sin}2\beta)^2}\right] \tag{A.4}$$

Within the MGM, gaugino masses can be give with good approximation by

$$m_{\widetilde{\chi}_1^0} \;=\; M_1 - \frac{m_{\mathrm{Z}^0}\sin^2\theta_W(M_1 + \mu\,\mathrm{sin}2\beta)}{\mu^2 - M_1^2}\,, \tag{A.5}$$

$$
\begin{aligned}
m_{\widetilde{\chi}_1^+} &= m_{\widetilde{\chi}_2^0} = M_2 - \frac{m_W^2(M_2+\mu \sin 2\beta)}{\mu^2 - M_2^2}\,, && \text{(A.6)}\\
m_{\widetilde{\chi}_2^+} &= \mu + \frac{m_W^2(\mu + M_2 \sin 2\beta)}{\mu^2 - M_2^2}\,, && \text{(A.7)}\\
m_{\widetilde{\chi}_3^0} &= \mu + \frac{m_{\mathrm{Z}^0}^2(1+\sin 2\beta)(\mu - M_1 \cos^2\theta_W - M_2 \sin^2\theta_W)}{2(\mu - M_1)(\mu - M_2)}\,, && \text{(A.8)}\\
m_{\widetilde{\chi}_4^0} &= -\mu - \frac{m_{\mathrm{Z}^0}^2(1-\sin 2\beta)(\mu + M_1 \cos^2\theta_W + M_2 \sin^2\theta_W)}{2(\mu + M_1)(\mu + M_2)}\,. && \text{(A.9)}\\
& && \text{(A.10)}
\end{aligned}
$$

The lightest neutralino is mainly B-ino, $\widetilde{\chi}_1^+$ and $\widetilde{\chi}_2^0$ from a degenerate W-ino weak triplet, and the nearly higgsinos $\widetilde{\chi}_2^+$ and $\widetilde{\chi}_{3,4}^0$ have masses roughly equal to μ.

A.2 Sleptons

The mass terms of squarks and sleptons are also modified after the electroweak symmetry breaking. There are four different contributions. One is the supersymmetric piece coming from the $|\partial W/\partial\phi_i|$ terms in Eq.(1.18), with $\phi_i = Q, U, D, L, E$. These terms add m_f^2 where m_f is the mass of the quarks and leptons from their Yukawa couplings to the Higgs boson. Next one is combining from the $|\partial W/\partial\phi_i|^2$ terms in Eq.(1.18) with $\phi_i = H_u$ or H_d in the superpotential Eq.(1.32). Because of the μ term,

$$
\begin{aligned}
\frac{\partial W}{\partial H_u^0} &= -\mu H_u^0 + \lambda_u^{ij}\tilde{Q}_i\tilde{U}_j\,, && \text{(A.11)}\\
\frac{\partial W}{\partial H_d^0} &= -\mu H_d^0 + \lambda_d^{ij}\tilde{Q}_i\tilde{D}_j + \lambda_e^{ij}\tilde{L}_i\tilde{E}_j\,. && \text{(A.12)}
\end{aligned}
$$

Taking the absolute square of these two expressions pick the cross terms together with $< H_d^0 >= v\cos\beta/\sqrt{2}$, $< H_u^0 >= v\sin\beta/\sqrt{2}$ and we obtain mixing between $\tilde{Q}$ and $\tilde{U}$, $\tilde{Q}$ and $\tilde{D}$ and $\tilde{L}$ and $\tilde{E}$. Similarly, the vacuum expectation values of the Higgs bosons in the trilinear couplings Eq.(1.36) also generate similar mixing terms. Finally, the D-term potential after eliminating the auxiliary field D Eq.(1.21) also give contributions to the scalar masses $m_{\mathrm{Z}^0}^2(I_3 - Q\sin^2\theta_W)\cos 2\beta$. Therefore, the mass matrix of stop, for instance, is given as

$$
-(\tilde{t}_L^*\,,\ \tilde{t}_R^*)\begin{pmatrix} m_{Q_3}^2 + m_t^2 + m_{\mathrm{Z}^0}^2(\frac{1}{2} - \frac{2}{3}\sin^2\theta_W)\cos 2\beta & m_t(A_t - \mu\cot\beta) \\ m_t(A_t - \mu\cot\beta) & m_{U_3}^2 + m_t^2 + m_{\mathrm{Z}^0}^2(-\frac{2}{3}\sin^2\theta_W)\cos 2\beta \end{pmatrix}\begin{pmatrix}\tilde{t}_L \\ \tilde{t}_R\end{pmatrix}, \qquad \text{(A.13)}
$$

Here $\tilde{t}_L$ is the up component of $\tilde{Q}_3$, and $\tilde{t}_R = \tilde{T}^*$. For a down-type sfermion, the $\cot\beta$ in the off-diagonal term is changed to $\tan\beta$. Also, the off-diagonal term is negligible for all but the third generation sfermions.

Appendix B

The OPAL collaboration

The OPAL Collaboration

G. Abbiendi[2], C. Ainsley[5], P.F. Åkesson[3], G. Alexander[22], J. Allison[16], G. Anagnostou[1], K.J. Anderson[9], S. Arcelli[17], S. Asai[23], D. Axen[27], G. Azuelos[18,a], I. Bailey[26], A.H. Ball[8], E. Barberio[8], R.J. Barlow[16], R.J. Batley[5], T. Behnke[25], K.W. Bell[20], G. Bella[22], A. Bellerive[9], G. Benelli[2], S. Bethke[32], O. Biebel[32], I.J. Bloodworth[1], O. Boeriu[10], P. Bock[11], J. Böhme[25], D. Bonacorsi[2], M. Boutemeur[31], S. Braibant[8], L. Brigliadori[2], R.M. Brown[20], H.J. Burckhart[8], J. Cammin[3], P. Capiluppi[2], R.K. Carnegie[6], B. Caron[28], A.A. Carter[13], J.R. Carter[5], C.Y. Chang[17], D.G. Charlton[1,b], P.E.L. Clarke[15], E. Clay[15], I. Cohen[22], J. Couchman[15], A. Csilling[15,i], M. Cuffiani[2], S. Dado[21], G.M. Dallavalle[2], S. Dallison[16], A. De Roeck[8], E.A. De Wolf[8], P. Dervan[15], K. Desch[25], B. Dienes[30,f], M.S. Dixit[7], M. Donkers[6], J. Dubbert[31], E. Duchovni[24], G. Duckeck[31], I.P. Duerdoth[16], P.G. Estabrooks[6], E. Etzion[22], F. Fabbri[2], M. Fanti[2], L. Feld[10], P. Ferrari[12], F. Fiedler[8], I. Fleck[10], M. Ford[5], A. Frey[8], A. Fürtjes[8], D.I. Futyan[16], P. Gagnon[12], J.W. Gary[4], G. Gaycken[25], C. Geich-Gimbel[3], G. Giacomelli[2], P. Giacomelli[8], D. Glenzinski[9], J. Goldberg[21], C. Grandi[2], K. Graham[26], E. Gross[24], J. Grunhaus[22], M. Gruwé[08], P.O. Günther[3], A. Gupta[9], C. Hajdu[29], G.G. Hanson[12], K. Harder[25], A. Harel[21], M. Harin-Dirac[4], M. Hauschild[8], C.M. Hawkes[1], R. Hawkings[8], R.J. Hemingway[6], C. Hensel[25], G. Herten[10], R.D. Heuer[25], J.C. Hill[5], K. Hoffman[8], R.J. Homer[1], A.K. Honma[8], D. Horváth[29,c], K.R. Hossain[28], R. Howard[27], P. Hüntemeyer[25], P. Igo-Kemenes[11], K. Ishii[23], A. Jawahery[17], H. Jeremie[18], C.R. Jones[5], P. Jovanovic[1], T.R. Junk[6], N. Kanaya[23], J. Kanzaki[23], G. Karapetian[18], D. Karlen[6], V. Kartvelishvili[16], K. Kawagoe[23], T. Kawamoto[23], R.K. Keeler[26], R.G. Kellogg[17], B.W. Kennedy[20], D.H. Kim[19], K. Klein[11], A. Klier[24], S. Kluth[32], T. Kobayashi[23], M. Kobel[3], T.P. Kokott[3], S. Komamiya[23], R.V. Kowalewski[26], T. Kämer[25], T. Kress[4], P. Krieger[6], J. von Krogh[11], D. Krop[12], T. Kuhl[3], M. Kupper[24], P. Kyberd[13], G.D. Lafferty[16], H. Landsman[21], D. Lanske[14], I. Lawson[26], J.G. Layter[4], A. Leins[31], D. Lellouch[24], J. Letts[12], L. Levinson[24], R. Liebisch[11], J. Lillich[10], C. Littlewood[5], A.W. Lloyd[1], S.L. Lloyd[13], F.K. Loebinger[16], G.D. Long[26], M.J. Losty[7], J. Lu[27], J. Ludwig[10], A. Macchiolo[18], A. Macpherson[28,l], W. Mader[3], S. Marcellini[2], T.E. Marchant[16], A.J. Martin[13], J.P. Martin[18], G. Martinez[17], T. Mashimo[23], P. Mättig[24], W.J. McDonald[28], J. McKenna[27], T.J. McMahon[1], R.A. McPherson[26], F. Meijers[8], P. Mendez-Lorenzo[31], W. Menges[25], F.S. Merritt[9], H. Mes[7], A. Michelini[2], S. Mihara[23], G. Mikenberg[24], D.J. Miller[15], W. Mohr[10], A. Montanari[2], T. Mori[23], K. Nagai[13], I. Nakamura[23], H.A. Neal[33], R. Nisius[8], S.W. O'Neale[1], F.G. Oakham[7], F. Odorici[2], A. Oh[8], A. Okpara[11], M.J. Oreglia[9], S. Orito[23], C. Pahl[32], G. Pásztor[8,i], J.R. Pater[16], G.N. Patrick[20], J.E. Pilcher[9], J. Pinfold[28], D.E. Plane[8], B. Poli[2], J. Polok[8], O. Pooth[8], A. Quadt[8], K. Rabbertz[8], C. Rembser[8], P. Renkel[24], H. Rick[4], N. Rodning[28], J.M. Roney[26], S. Rosati[3], K. Roscoe[16], A.M. Rossi[2], Y. Rozen[21], K. Runge[10], O. Runolfsson[8], D.R. Rust[12], K. Sachs[6], T. Saeki[23], O. Sahr[31], E.K.G. Sarkisyan[8,m], C. Sbarra[26], A.D. Schaile[31], O. Schaile[31], P. Scharff-Hansen[8], M. Schröder[8], M. Schumacher[25], C. Schwick[8], W.G. Scott[20], R. Seuster[14,g], T.G. Shears[8,j], B.C. Shen[4],

C.H. Shepherd-Themistocleous[5], P. Sherwood[15], G.P. Siroli[2], A. Skuja[17], A.M. Smith[8], G.A. Snow[17], R. Sobie[26], S. Söldner-Rembold[10,e], S. Spagnolo[20], F. Spano[9], M. Sproston[20], A. Stahl[3], K. Stephens[16], D. Strom[19], R. Ströhmer[31], L. Stumpf[26], B. Surrow[8], S.D. Talbot[1], S. Tarem[21], M. Tasevsky[8], R.J. Taylor[15], R. Teuscher[9], J. Thomas[15], M.A. Thomson[5], E. Torrence[9], S. Towers[6], D. Toya[23], T. Trefzger[31], I. Trigger[8], Z. Trócsányi[30,f], E. Tsur[22], M.F. Turner-Watson[1], I. Ueda[23], B. Vachon[26], C.F. Vollmer[31], P. Vannerem[10], M. Verzocchi[8], H. Voss[8], J. Vossebeld[8], D. Waller[6], C.P. Ward[5], D.R. Ward[5], P.M. Watkins[1], A.T. Watson[1], N.K. Watson[1], P.S. Wells[8], T. Wengler[8], N. Wermes[3], D. Wetterling[11] J.S. White[6], G.W. Wilson[16], J.A. Wilson[1], T.R. Wyatt[16], S. Yamashita[23], V. Zacek[18], D. Zer-Zion[8,k]

[1]School of Physics and Astronomy, University of Birmingham, Birmingham B15 2TT, UK
[2]Dipartimento di Fisica dell' Università di Bologna and INFN, I-40126 Bologna, Italy
[3]Physikalisches Institut, Universität Bonn, D-53115 Bonn, Germany
[4]Department of Physics, University of California, Riverside CA 92521, USA
[5]Cavendish Laboratory, Cambridge CB3 0HE, UK
[6]Ottawa-Carleton Institute for Physics, Department of Physics, Carleton University, Ottawa, Ontario K1S 5B6, Canada
[7]Centre for Research in Particle Physics, Carleton University, Ottawa, Ontario K1S 5B6, Canada
[8]CERN, European Organisation for Nuclear Research, CH-1211 Geneva 23, Switzerland
[9]Enrico Fermi Institute and Department of Physics, University of Chicago, Chicago IL 60637, USA
[10]Fakultät für Physik, Albert Ludwigs Universität, D-79104 Freiburg, Germany
[11]Physikalisches Institut, Universität Heidelberg, D-69120 Heidelberg, Germany
[12]Indiana University, Department of Physics, Swain Hall West 117, Bloomington IN 47405, USA
[13]Queen Mary and Westfield College, University of London, London E1 4NS, UK
[14]Technische Hochschule Aachen, III Physikalisches Institut, Sommerfeldstrasse 26-28, D-52056 Aachen, Germany
[15]University College London, London WC1E 6BT, UK
[16]Department of Physics, Schuster Laboratory, The University, Manchester M13 9PL, UK
[17]Department of Physics, University of Maryland, College Park, MD 20742, USA
[18]Laboratoire de Physique Nucléaire, Université de Montréal, Montréal, Quebec H3C 3J7, Canada
[19]University of Oregon, Department of Physics, Eugene OR 97403, USA
[20]CLRC Rutherford Appleton Laboratory, Chilton, Didcot, Oxfordshire OX11 0QX, UK
[21]Department of Physics, Technion-Israel Institute of Technology, Haifa 32000, Israel
[22]Department of Physics and Astronomy, Tel Aviv University, Tel Aviv 69978, Israel
[23]International Centre for Elementary Particle Physics and Department of Physics, University of Tokyo, Tokyo 113-0033, and Kobe University, Kobe 657-8501, Japan
[24]Particle Physics Department, Weizmann Institute of Science, Rehovot 76100, Israel
[25]Universität Hamburg/DESY, II Institut für Experimental Physik, Notkestrasse 85, D-22607 Hamburg, Germany
[26]University of Victoria, Department of Physics, P O Box 3055, Victoria BC V8W 3P6, Canada
[27]University of British Columbia, Department of Physics, Vancouver BC V6T 1Z1, Canada
[28]University of Alberta, Department of Physics, Edmonton AB T6G 2J1, Canada
[29]Research Institute for Particle and Nuclear Physics, H-1525 Budapest, P O Box 49, Hungary
[30]Institute of Nuclear Research, H-4001 Debrecen, P O Box 51, Hungary
[31]Ludwigs-Maximilians-Universität München, Sektion Physik, Am Coulombwall 1, D-85748 Garching, Germany
[32]Max-Planck-Institute für Physik, Föhring Ring 6, 80805 München, Germany
[33]Yale University,Department of Physics,New Haven, CT 06520, USA

[a] and at TRIUMF, Vancouver, Canada V6T 2A3
[b] and Royal Society University Research Fellow
[c] and Institute of Nuclear Research, Debrecen, Hungary
[e] and Heisenberg Fellow
[f] and Department of Experimental Physics, Lajos Kossuth University, Debrecen, Hungary
[g] and MPI München
[i] and Research Institute for Particle and Nuclear Physics, Budapest, Hungary
[j] now at University of Liverpool, Dept of Physics, Liverpool L69 3BX, UK
[k] and University of California, Riverside, High Energy Physics Group, CA 92521, USA
[l] and CERN, EP Div, 1211 Geneva 23
[m] and Tel Aviv University, School of Physics and Astronomy, Tel Aviv 69978, Israel.

Bibliography

[1] OPAL Collaboration, G. Abbiendi et al., hep-ex/0101014, accepted by *Phys. Lett. B*.

[2] OPAL Collaboration, G. Abbiendi et al., hep-ex/0012018, submitted to *Eur. Phys. J.*

[3] R. Barbieri and G.F. Giudice, *Nucl. Phys.* **B347** (1995) 300, hep-ph/9409419, *Phys. Rev.* **D52** (1995) 1693, hep-ph/9412322.

[4] MUON G-2 Collaboration, H.N. Brown, et al., hep-ex/0102017, submitted to *Phys. Rev. Lett.*

[5] T. Hambye and K. Riesselmann, *Phys. Rev.* **D55** (1997) 7255.

[6] P. Fayet, *Phys. Lett.* **B70** (1997) 461.

[7] Y. Fol'fand and E. Likhatam, *JETP Lett.* **13** (1971) 323; D. Volkov and V. Akulov, *Phys. Lett.* **B46** (1973) 109; J. Wess and B. Zumino, *Nucl. Phys.* **B70** (1974) 38.

[8] K. Intrigator and N. Seiberg, *Nucl. Phys. Suppl.* **45BC** (1996) 1, hep-th/9509066.

[9] H. Murayama, "SUPERSYMMETRY PHENOMENOLOGY", hep-ph/0002232.

[10] J. Ellis, S. Kelley, D.V. Nanopoulos *Nucl. Phys.* **B373** (1992) 55; ALEPH Collaboration, DELPHI, Collaboration, ELECTROWEAK Group, L3 Collaboration, OPAL Collaboration, SLD HEAVY FLAVOUR Group, CERN-EP-2000-016.

[11] R.S. Chivukula, hep-ph/0011264.

[12] P. Janot, "Priorities for LEP in 2000" proceedings; J. Sladen, "The RF system to 102 GeV" proceedings; M. jonker, private communication.

[13] ALEPH Collaboration, D. Buskulic et al., *Nucl. Inst. Meth.* **A360** (1995) 481.

[14] DELPHI Collaboration, P. Abreu et al., *Nucl. Inst. Meth.* **A360** (1995) 57.

[15] L3 Collaboration, O. Adriani et al., *Phys. Rep.* (1993) 236.

[16] OPAL Collaboration, K. Ahmet et al., *Nucl. Instr. and Meth.* **A305** (1991) 275; P. P. Allport et al., *Nucl. Instr. and Meth.* **A346** (1994) 476; B.E. Anderson et al., *IEEE Trans. on Nucl. Science* **41** (1994) 845.

[17] J. Allison et al., *Nucl. Instr. and Meth.* **A317** (1992) 47.

[18] GEANT-Detector Description and Simulation Tools, CERN Program Library.

[19] S. Jadaha, B.F.L. Ward and Z. Was, *Phys. Lett.* **B449** (1999) 97.

[20] S. Jadach, B.F.L. Ward, Z. Was, *Phys. Lett.* **B449** (1999) 97.

[21] T. Sjöstrand, *Comp. Phys. Comm.* **39** (1986) 347;
T. Sjöstrand, PYTHIA 5.7 and JETSET 7.4 Manual, hep-ph/9508391.

[22] S. Jadach, Z. Was, R. Decker, J.H. Kuhn, *Comput. Phys. Commun.* **76** (1993) 361.

[23] E. Barberio, Z. Was, *Comput. Phys. Commun.* **79** (1994) 291.

[24] S. Jadach, W. Placzek and B.F.L. Ward, *Phys. Lett* **B390** (1997) 298;
S. Jadach, W. Placzek and B.F.L. Ward, in 'Physics at LEP2', eds. G. Altarelli, T. Sjöstrand and F. Zwirner, CERN 96-01, vol. 2 (1996).

[25] D. Karlen, *Nucl. Phys.* **B289** (1987) 23.

[26] J. Fujimoto et al., *Comp. Phys. Comm.* **100** (1997) 128.

[27] S. Jadach, W. Placzek, M. Skrzypek, B.F.L. Ward, Z. Was, *Comput. Phys. Commun.* **119** (1999) 272.

[28] C. Dionisi et al., in 'Physics at LEP2', eds. G. Altareli, T. Sjöstrand and F. Zwirner, CERN 96-01, vol.2 (1996) 337.

[29] C. Dionisi et al., in 'Physics at LEP2', eds. G.Altareli, T. Sjöstrand and F. Zwirner, CERN 96-01, vol.2 (1996) 337.

[30] H. Murayama, I. Watanabe and K. Hagiwara, KEK Preprint 91-11 (1992).

[31] S. Kawabata, *Comput. Phys. Commun.* **41** (1986) 127, ibid, **88** (1985) 309.

[32] JADE Collaboration, S. Bethke et al., *Phys. Lett.*, **B213** (1988) 235.

[33] The OPAL Collaboration, G. Abbiendi et al., *Eur. Phys. J.* **C14** (2000) 373.

[34] T. Junk, OPAL Technical Note TN-570 (1998) 1.

[35] OPAL Collaboration, G. Alexander et al., *Eur. Phys. J.* **C18** (2000) 253.

[36] OPAL Collaboration, G. Alexander et al., *Eur. Phys. J.* **C14** (2000) 51.

[37] "Searches for Prompt Light Gravitino Signatures in e+e- Collisions at sqrt(s) = 189 GeV", CERN-EP-2000-078, submitted to *Phys. Lett. B*.

[38] A.F. Frodesen, O. Skeggestad, and H. Tofte, Probability and Statistics in Particle Physics, Universitetsforlaget, 1979, ISBN 82-00-01-01906-3; S.L. Meyer, Data Analysis for Scientists and Engineers, John Wiley and Sons, 1975, ISBN 0-471-59995-6.

[39] R.D. Cousins and V.L. Highland, *Nucl, Instr. Meth.* **A320** (1992) 331.

[40] Particle Data Group, *Phys. Rev.* **D54** (1996) 1.

[41] O. Helene, *Nucl.Instr. and Meth.* **A212** (1983) 319,
Nucl. Instr. and Meth. **A228** (1984) 120.

[42] J.F. Gunion, H.E. Haber, G. Kane, and S. Dawson, "Higgs Hunter's Guide"
Addison-Wesley, 1990 (Frontiers in Physics, 80).

[43] Y. Okada, M. Yamaguchi, and T. Yanagida, *Prog. Theor. Phys.*, **85**, (1991) 1, *Phys. Lett.* **B262** (1991) 54;
J. Ellis, G. Ridolfi, and F. Zwirner, *Phys, Lett.* **B257** (1991) 83, *ibid.* **B262** (1991) 477, *ibid.* **B271** (1991) 123.

[44] J.R. Espinosa and R.J. Zhang, hep-ph/9912236; M. Carena, H.E. Haber, S. Heinemeyer, W. Hollik, C.E.M. Wagner, a and G. Weiglein, hep-ph/0001002.

[45] The Super-Kamiokande Collaboration (M. Shiozawa et al.), *Phys. Rev. Lett.* **81** (1998) 3319, hep-ex/9806014.

[46] G.F. Giudice, R. Rattazzi, *Phys.Rept.* **322** (1999) 419, *Phys.Rept.* **322** (1999) 501.

[47] S. Ambrosamio, G.D. Kribs and S.P. Martin, *Nucl. Phys. B* **516** 55 (1998).

[48] E. Duchovini, J. Ihmels, A. Wodecki, J. Kraskiewicz, "Decay State Signatures at LEP2 for the Supersymmetric Theories with Gauge Mediated Supersymmetry Breaking", Weizmann Institue preprint WIS/09/00-June-DPP.

[49] S. Katsanevas and P. Morawitz *Comput. Phys. Commun.* **112** (1998) 227.

[50] OPAL Collaboration, G. Abbiendi et al., *Eur. Phys. J.* **C18** (2000) 253.

[51] V. Barger, M.S. Berger, and P. Ohmann, *Phys. Rev. D* **49** (1994) 4908;
S.P. Martin and M.T. Vaughn, *Phys. Rev. D* **50** (1994) 2282.